DEVELOPMENT OF SURFACE-ENHANCED RAMAN SCATTERING-BASED NANOSPECTROSCOPIC METHODS FOR TOXICITY DETERMINATION OF NANOMATERIALS

by

Gamze Kuku

Submitted to Graduate School of Natural and Applied Sciences

in Partial Fulfillment of the Requirements

for the Degree of Doctor of Philosophy in

Biotechnology

Yeditepe University

2017

DEVELOPMENT OF SURFACE-ENHANCED RAMAN SCATTERING-BASED NANOSPECTROSCOPIC METHODS FOR TOXICITY DETERMINATION OF NANOMATERIALS

APPROVED BY:

Prof. Dr. Mustafa Çulha
(Thesis Supervisor) .....

Assoc. Prof. Dr. Hande Sipahi .....

Assist. Prof. Dr. Andrew John Harvey .....

Assist. Prof. Dr. Kaan Keçeci .....

Assist. Prof. Dr. Sultan Sibel Erdem .....

DATE OF APPROVAL: ..../..../2017

Dedicated to the hearts
beating for the Beauty…

ACKNOWLEDGEMENTS

Every beautiful story, dear reader, has to conclude someday and you will be reading the summary of a five-year journey with continuous challenges, learning, and development. I believe I was blessed with meeting and getting to know wonderful people throughout this journey, which is one of the greatest bestowments in life. So, let me acknowledge them before everything else.

I would like to gratefully thank my supervisor Prof. Mustafa Çulha to provide me the opportunity to take part in the exciting COST Action (MP1302) project funded by TUBITAK (Project no: 113Z554). He has been a great role model for me to be both "tenacious" and humble in scientific research. It was also a kind of addiction to listen to his morning talks starting from Middle Asia and ending in space or somewhere that we do not even know.

I am also grateful to my thesis monitoring committee members Assist Prof. Andrew J. Harvey and Assoc. Prof. Hande Sipahi for their constructive comments and directive ideas throughout thesis work.

An individual paragraph absolutely comes for my project mate Melike Sarıçam. We have grown up together with this project and had endless fun, endless possible solutions to our struggles, and endless "combinations". She deserves additional thanks to endure my nerd jokes which I am sure made her stronger -if they still did not kill her- and to "provide her shoulder" whenever I needed.

I prepared the samples for TEM and EDF microscopy in Kazan, Tatarstan, and the microscopy images were obtained by Assoc. Prof. Rawil Fakhrullin's group. Besides his kind scientific help, I am also thankful to him and his research group full of wonderful people for helping me throughout my stay there. Gölnur Fakhrullina, Ramil Fakhrullin, Elvira Rozhina, Farida Akhatova, Elvira Gaiazova, Ekaterina Naumenko and Maria Kibardina thank you for making those two weeks in Kazan an unforgettable memory.

I also thank the co-authors I wrote articles with; Mine Altunbek, Sevda Mert, Ertuğ Avcı, Farida Akhatova, and Anna Danilushkina, it was a beneficiary experience. Mine, I also thank you for being a collaborator of our crazy lab emplacement ideas.

The smart and hardworking undergraduate project students Merve Coşkun, Ayşegül Ekmekçioğlu, Buşra Kasap, and Betül Yurttaş also contributed a lot to this thesis. I thank

you for sharing nice memories and misfortunate moments in research. With you, I tasted a bit of how it feels like to be a supervisor and the responsibilities that it brought.

I am thankful to have a research group that is helpful to the most and fun at the same time. Nano group is the best! Besides that, as the famous saying goes, “all work and no play makes Jack a dull boy”. My dearest friends and sisters in my heart, I owe you a big “thank you!”; Seda Keleştemur the super mom and the coffee mate, Zehra Çobandede the inventor, Sevda Mert the figure drawer, Hande Duru the surpriser (Surprise!), Zeynep Işık the “euro” tracker, Merve Ercan the delicate vintage girl, Hamide Özaydın the best!, Dr. Suheir Zaghal the role model of women-in-science and of course Dr. Fatma Özen, my friend since the very first days of our university career - I think a good “eleven” years do not need any further thanks. Many more people of Yeditepe University who were always willing to help with a big smile and chat in between experiments. They made long hours in the lab a fun time. Selin Kılınç Lekesiz and Melek Bakiler, my honorary thesis controllers and connection to the world outside science, even knowing that I have you as friends is good even though I had times that I could not find much chance to be together.

My relatives who supported me with their prayers and always motivated; Mukadder & Ünal Badat, the members of Yorgancoğlu family and very special “Bahçemirler”, Fatma (Şahver) Baruş, Meral Bacak, Munise & Tuğrul Kırca with their fragile princess Beril Ece, Kerime & Baran Çelik with the smartest Rengin İnci and the newbie Ayşin Evin, and finally my honorary elder sister Zohreh Varasteh (Abla!), I am grateful for your presence.

However, no other person deserves greater thankfulness than my beloved mother Melahat Kuku and sister Gökçe Çolak with her husband Hüseyin Çolak who joined to the family on the half way of my thesis. Dearest mom, your impatient patience, angry cuteness, hard looking soft heart and even the unique ways to motivate me to finish writing this thesis are my source of energy to always carry on, and never give up. And my dearest sister, although you left the “Kuku sistas” alliance, there is no escape from being a member. Having you as a sincere art director, food critique, fashion designer, and all the rest are what brings joy to life; “it is the way of enjoy!”

And a place that can never be filled, the love and unseen support of my father with his unique laughter that echoes in my ears. I hope and strive to meet you in the place of no sorrow. Till then, know that I do continue!

ABSTRACT

DEVELOPMENT OF SURFACE-ENHANCED RAMAN SCATTERING-BASED NANOSPECTROSCOPIC METHODS FOR TOXICITY DETERMINATION OF NANOMATERIALS

The intensive research on nanomaterials (NMs) in the last decades resulted in broad applications in many industries ranging from energy deposition to medicine, cosmetics, food, textile, military or communication. The tremendous utilization of these newly discovered materials, however, also raised concerns about their possible side effects. On the other hand, the efforts to determine NM toxicity faced problems in terms of obtaining accurate results; originating from the physicochemical properties of NMs. Most of the conventional cytotoxicity assays have been reported to give false results due to interaction with assay components or absorbance artefacts. Therefore, *in vitro* nanotoxicity evaluation field is in need of alternative approaches.

In an attempt to propose a new perspective, in the present work, surface-enhanced Raman scattering (SERS) was utilized on four cell lines; lung adenocarcinoma (A549), human and mouse fibroblasts (HSF, L929), and human umbilical vein endothelial cell line (HUVEC), to test *in vitro* nanotoxicity of a panel of NMs; zinc oxide and titanium dioxide nanoparticles, single- and multi-walled carbon nanotubes, and quantum dots. Before that, SERS substrate localization within the cells as well as the spectral contributors were evaluated. Then, SERS spectra obtained from NM-exposed cells were carefully investigated for possible toxicity markers and seven of them were proposed to be in good correlation with the conventional cytotoxicity assays; apoptosis/necrosis and WST-1 cell proliferation assays, as well as the transmission electron microscopy and enhanced-dark field microscopy images. Altogether the results were in agreement with the nanotoxicity studies in the literature. The seven intensity ratios gave information about the rates of collagen, fibronectin, cholesterol depletion, lipid stability, tyrosine phosphorylation, phenylalanine to tyrosine conversion and protein C-S to S-S bond conversion, all of which can also be utilized for various further cellular SERS studies.

ÖZET

NANOMALZEMELERİN TOKSİSİTELERİNİ BELİRLEMEK İÇİN YÜZEYDE-ZENGİNLEŞTİRİLMİŞ RAMAN SAÇILMASINA DAYALI NANOSPEKTROSKOPİK YÖNTEMLERİN GELİŞTİRİLMESİ

Son yıllarda nanomalzemeler (NM) üzerinde yapılan yoğun araştırmalar sonucu enerji depolama endüstrisinden tıp, kozmetik, gıda, tekstil, askeriye ve iletişim gibi geniş bir alanda bu malzemeler kullanılmaya başlanmıştır. Bu kullanım aynı zamanda olası yan etkileri düşündürmeye başlamıştır. Öte yandan, NM'lerin fizikokimyasal özellikleri sebebiyle elde edilen tutarsız sonuçlar NM toksisitesini belirlemek için atılan adımlarda sorun oluşturmuştur. Yaygın olarak kullanılan sitotoksisite deneylerinin çoğunda, NM'lerin deney bileşenleriyle etkileşime girmesi ya da absorbans kalıntıları oluşturması sebebiyle yanıltıcı sonuçlar elde edildiği bildirilmiştir. Dolayısıyla *in vitro* nanotoksisite araştırmalarında alternatif yaklaşımlara ihtiyaç duyulmaktadır.

Bu noktada yeni bir bakış açısı sunmak amacıyla bu çalışmada Yüzeyde-Zenginleştirilmiş Raman Saçılmasına dayalı olarak (YZRS) *in vitro* nanotoksisite belirlenmesinde dört hücre hattı (akciğer adenokarsinomu (A549), insan ve fare fibroblastı (HSF ve L929) ve insan göbek bağı damar endotel hücresi (HUVEC)), çinko oksit ve titanyum dioksit nanoparçacıklar, tek ve çok katmanlı karbon nanotüpler ve kuantum noktaları gibi çeşitli NM'lere maruz bırakılmıştır. Daha sonra, NM'lere maruz bırakılan hücrelerden elde edilen spektrumlar, olası toksisite belirteçlerini bulmak amacıyla dikkatlice incelendi. Belirteçlerden yedi tanesi yaygın olarak kullanılan toksisite deneylerinden olan apoptoz/nekroz ve WST-1 hücre çoğalma testlerinden elde edilen sonuçlarla ve geçirimli elektron mikroskobu ile zenginleştirilmiş karanlık alan mikroskobu görüntüleriyle uyum içinde bulundu. Tüm sonuçların literatürde bulunan nanotoksisite çalışmalarıyla bağdaştığı gözlemlendi. Bulunan yedi bant yoğunluk oranı kollajen, fibronektin, kolesterol tükenmesi, lipid stabilitesi, tirozin fosforlanması, fenilalanin-tirozin dönüşümü ve proteinlerin C-S bağlarının S-S'ye dönüşümü hakkında bilgi vermekle birlikte bu oranların farklı pek çok hücresel YZRS çalışmasında kullanılabileceği öngörülmektedir.

TABLE OF CONTENTS

LIST OF FIGURES

LIST OF TABLES

LIST OF SYMBOLS/ABBREVIATIONS

°C	Degrees Celsius
cm^{-1}	Wavenumber
ml	Milliliter
nm	Nanometer
α	Alpha
β	Beta
µl	Microliter
µM	Micromolar
µm	Micrometer
A	Adenine
a.u.	Arbitrary units
ADP	Adenosine diphosphate
AFM	Atomic force microscopy
ANOVA	Analysis of variance
ApoE	Apolipoprotein E
AuNP	Gold nanoparticle
ARF6	ADP-ribosylation factor 6
CaF_2	Calcium fluoride
CARS	Coherent anti-Stokes Raman scattering
CCD	Charge-coupled device
CE	Chemical enhancement mechanism
CO_2	Carbondioxide
DAPI	4',6-diamidino-2-phenylindole
DCFH-DA	Dichloro-dihydro-fluorescein diacetate
DLS	Dynamic light scattering
DMEM	Dulbecco's Modified Eagle Medium
DMEM-F12	Dulbecco's Modified Eagle Medium: Nutrient Mixture F-12
DNA	Deoxyribonucleic acid

DOF	Degrees of freedom
ECM	Extracellular matrix
EDF	Enhanced-dark field
EDTA	Ethylenediaminetetraacetic acid
ELISA	Enzyme-linked immunosorbent assay
EM	Electromagnetic enhancement mechanism
ER	Endoplasmic reticulum
FBS	Fetal bovine serum
FITC	Fluorescein isothiocyanate
G	Guanine
GEEC	Glycosylphosphatidylinositol-enriched endosomal compartments
H_2O_2	Hydrogen peroxide
$HAuCl_4$	Hydrogen tetrachloroaurate
IR	Infrared
LDH	Lactate dehydrogenase
LOD	Limit of detection
LSPR	Localized surface plasmon resonance
mPMS	1-Methoxy-5-methylphenazinium methyl sulfate
MRI	Magnetic resonance imaging
mW	Milliwatt
MWCNT	Multi-walled carbon nanotube
N.A.	Numerical aperture
NADH	Nicotinamide adenine dinucleotide
NM	Nanomaterial
OH	Hydroxyl
PBS	Phosphate-buffered saline
PDMS	Polydimethylsiloxane
Phe	Phenylalanine
PI	Propidium iodide
PLGA	Poly(lactic-co-glycolic acid)
PO_2	Phosphate
Pro	Proline
QD	Quantum dot

ROS	Reactive oxygen species
S.D.	Standard deviation
SERS	Surface-enhanced Raman scattering
SERRS	Surface-enhanced resonance Raman scattering
SOD	Superoxide dismutase
SORS	Spatially offset Raman scattering
SRS	Stimulated Raman scattering
SWCNT	Single-walled carbon nanotube
TEM	Transmission electron microscopy
TERS	Tip-enhanced Raman scattering
TiO_2 NP	Titanium dioxide nanoparticle
Trp	Tryptophan
TRS	Transmission Raman scattering
Tyr	Tyrosine
UV-Vis	Ultraviolet-Visible
WST-1	Water-soluble tetrazolium-1
ZnO NP	Zinc oxide nanoparticle

1. INTRODUCTION

1.1. THE BIRTH OF NANOTECHNOLOGY

Nanomaterials (NMs) are defined as materials or substances with at least one diameter of 1-100 nm size and the word comes from the Greek word for dwarf; *nanos*. Throughout the history of civilization, several kinds of NMs were found to be used for several purposes although without knowing the materials were nanoscale [1]–[3]. Among them, colloidal gold has a special place. The use of colloidal gold to boost up health and fertility in Ancient China dates back to 2500 BC. The Chinese words *Kim* (gold) and *Yeh* (juice) were adapted as "*Kimiye*" by Arabic scholars with the article "*al*"; "*Alkimiya*" which was transferred to Europe as "*Alchemy*" [4]. The magical impact of the material continued for centuries worldwide and with the advancement of science and technology it became possible to investigate and develop further benefits of such materials. Although the lecture from 1857 by Michael Faraday on the light interactions of thin films of gold and other metals is often attributed to be the earliest report on the characterization of gold nanoparticles, the German chemist Johann Kunckels had concluded in his book from 1676 that "*gold must be present in such a degree of comminution that it is not visible to the human eye*" [5], [6]. Faraday have shown evidences of unique physicochemical properties of various thin metal films, the thickness of gold films were calculated to be 1/278000 of an inch which is about 90 nm. The varying properties with varying thicknesses compared to bulk gold included color change and lower melting points. His studies were expanded by several others to understand the characteristics of these thin films further [7]–[9]. Meanwhile similar studies were going on, the field of quantum physics was also growing and new theories enabled scientists to reach more detailed explanations on the various behavior of NMs. Inspired by "the marvelous biological system" that cannot only successfully write but also can function at nanoscale, Richard P. Feynmann gave his famous, challenging and brainstorming lecture "There's plenty of room at the bottom!" on December 29, 1959 [10]. Being one of the leading theoretical physicists of his time, he was challenging scientists and high school students to contribute to this promising and exciting field by creating tiny machines. For instance, he offered a prize of 1000 dollars to the first person who would make an operating, rotating

electric motor of only 1/64 inch cube that can be controlled from the outside and not counting the lead-in wires. The lecture is widely accepted as the seeds of nanotechnology field today even though it did not get many citations – only seven – in the first two decades after the lecture was given [11].

1.2. NANOMATERIAL CHARACTERISTICS

The uniqueness of NMs compared to their bulk forms mainly comes from two types of effects occurring at nanoscale; one is **size effect** and the other is **quantum confinement effect** of delocalized electron states.

Once a material is at nanoscale, it gains an incredible surface area compared to its bulk counterpart. In Figure 1.1, specific surface areas of particles with decreasing diameters were calculated by the help of below formula (1.1) where S is the specific surface area, in other words the surface area per unit weight; in m^2/g, d is the particle diameter in nanometers and ρ is the density of the material in g/cm^3:

$$S = \frac{6000}{d \times \rho} \tag{1.1}$$

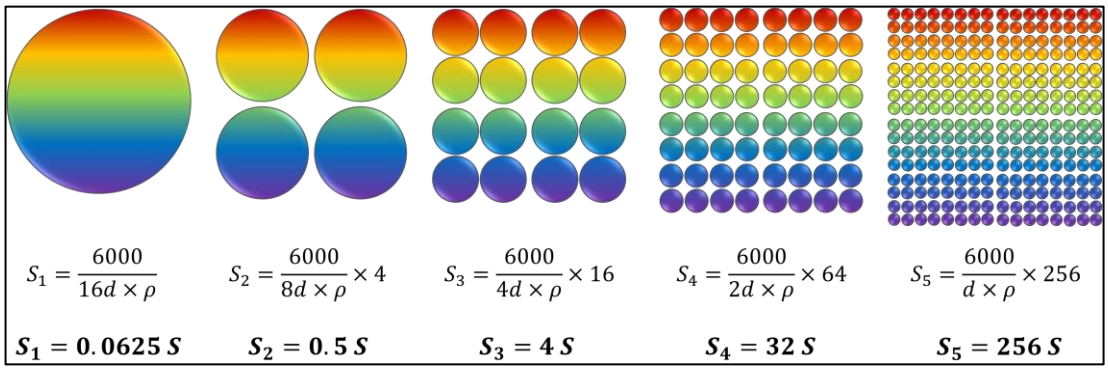

Figure 1.1. Specific surface areas of hypothetical particles with decreasing diameters.

In this hypothetical particle example, dividing a single large particle into particles with a diameter of only $^{1}/_{16}$ times yielded an increase of $^{256}/_{0.0625} = 4096$ times the surface area of the bulk material. Higher specific surface area enables higher reactivity, higher solubility as well as lower melting temperature due to increased number of exposed atoms on the surface which are more easily accessible by reactants, solvents or any other medium.

The decrease in size restricts the movement of delocalized electrons and phonons, thus leading to an increase in the number of standing waves at a certain wavelength. This phenomenon can be exemplified with a police whistle. In order to produce a tone through the whistle, the air blown from the mouth should be at a certain wavelength. By changing the length of the whistle, it is possible to change its tone as well. The longer whistles require longer wavelengths to produce the necessary vibrations whereas the shorter ones need shorter wavelengths. The shorter the wavelength gets, the sharper the sound becomes. In the case of nanoparticles, the phonons are confined in a shorter space, thus their energy increases. This property is beneficial for optical and electronic applications such as the quantum dots (QDs) with longer-lasting fluorescence properties that are seen as future alternatives to the conventional fluorescent tags used in biomedical applications [12], [13].

The above mentioned unique physicochemical properties of NMs opened up the way for a broad field of applications in many technological as well as research areas [14]–[17]. Among them, biomedical applications of NMs produced the field of nanomedicine. Extensive research is still going on to improve diagnosis, treatment and prevention of diseases by applying “smart” NMs. Site-specific targeted drug delivery systems with nanodrug carriers, controlled drug release systems, multi-modal drugs that are functionalized to both visualize and treat the diseased region, improved magnetic resonance imaging (MRI) contrast agents, stronger implant materials, more biocompatible tissue scaffolds, improved surgical procedures, and extremely sensitive nanosensors to detect disease markers, viruses, bacteria, or glucose levels of patients are some examples of the potential improvements provided by the NMs [18]–[20].

1.3. NANOTOXICITY

The higher reactivity and higher ion release rates as well as similar sizes to cellular components make NMs candidates of toxic materials, too. The awareness on the toxic side effects of NMs has emerged upon the incredible advancement in NM-related research and applications. The term "**nanotoxicology**" was introduced by Donaldson and colleagues in 2004 and was defined by Oberdörster and colleagues as "*the science of engineered nanodevices and nanostructures that deals with their effects in living organisms*" in a review paper from 2005 [21], [22].

Nanotoxicology studies have been carried out not only by individual research groups but also by international consortia with the financial support of many organizations. These include European Union Framework Program 7 (EU FP7) projects such as FP7-MARINA and FP7-NANOVALID, and web-based repositories for nanotoxicology data mining studies such as nanoinfo.org and eNanoMapper [23]–[25]. These initiatives attempt to collect, process and classify the information related to nanotoxicology in such a way that will provide researchers all around the world a more precise evaluation of NM toxicity. Although the nanotoxicology field spans the toxicological response of organisms from microorganisms to *in vivo* human studies as well as to the environmental safety, only *in vitro* studies on human cell lines will be addressed in the scope of this thesis.

1.3.1. Factors that Determine Nanotoxicity of NMs

NMs might exert various toxic effects at various levels depending both on their intrinsic properties as well as some extrinsic conditions [26]:

- **Chemical composition** of a NM is one of the determining factors of nanotoxicity. A report by Lanone and colleagues showed that spherical metal oxide NPs of similar sizes varied in their cytotoxicity [27]. NMs containing copper or zinc were highly toxic whereas titanium-containing NMs showed milder cytotoxicity.
- Smaller **size**d NMs of same elements are considered to be more toxic compared to NMs with larger diameters [28] whereas **shape** is also important. In a study by Zheng and colleagues, spherical gold and silver NPs were more toxic than silver triangular

nanoplates and gold nanorods [29]. On the contrary, multi-walled carbon nanotubes (MWCNTs) of larger aspect ratio were shown to induce inflammation in mice compared with smaller ones [30]. Also, Yin and colleagues have shown that larger oleic acid-coated nickel ferrite NPs were more cytotoxic than smaller ones and they concluded that the increased toxic effects was either an indication of higher surface energy or higher surface interaction areas [31].

- Two **crystalline structures** of titanium dioxide (TiO_2) NPs exert high or milder toxicity for anatase and rutile structures of TiO_2 NPs, respectively and as such, crystallinity can be a determining factor of nanotoxicity [32].
- **Agglomeration status** of NMs change the toxic effect. The higher rate of agglomeration often results in the loss of some nanoscale properties of NMs and reduces cytotoxicity [33], [34].
- A very important factor determining nanotoxicity of a NM is its **surface properties** such as charge, chemistry or coating and area or porosity [35]–[38]. These three properties might influence the colloidal stability, cellular uptake route and rate as well as ion releasing capacity, all of which affect the toxic outcome [39], [40].
- In addition to NM characteristics, its environment also affect the toxic response. There are studies showing **cell-type** dependent response to NMs *in vitro*. In a study by Manshian and colleagues, QDs were tested on three cell lines; epithelial (BEAS-2B), fibroblast (HFF-1) and lymphoblastoid (TK6), representing three routes of exposure; bronchial, skin and circulatory, respectively [41]. Although the cellular uptake rate of BEAS-2B cells were the highest, the toxic outcome was more severe in HFF-1 and TK6 cells. The **culture medium content**, such as the amount of serum used, might also alter the cellular response as shown by Nafee and colleagues [42]. The cells that were cultured in serum-free medium were 15 per cent more susceptible to damage due to the lack of a protective shell around chitosan-modified Poly(lactic-co-glycolic acid) (PLGA) NPs.

1.3.2. Mechanisms of Nanotoxicity

NMs interact with the cells in several ways. They might be adsorbed to the cell surface or can enter the cells via endo-lysosomal pathways. Single-walled carbon nanotubes

(SWCNTs) that were not internalized into cells but are still on the cell surface were shown to create physical stress on the cells and might also adsorb culture medium ingredients [43]. Depletion of medium then results in starvation stress and the cells are affected indirectly from these NMs. Although there are also reports claiming that some NMs might be internalized through membrane diffusion, there is an ongoing debate whether this can be the case or not [44]–[46].

The moment NMs are administered into the cell culture medium; proteins, metals, small molecules or polymers tend to interact with the NM and form a so-called "**corona**" on NM surface [47], [48]. The studies concerning the NM-protein corona content and its changes have recently been termed as "**coronome**" and the coronome field promises to be a hot topic in the near future [49].

In Figure 1.2, evolution of a corona around a bare NP is given. The modifications on the protein corona have been shown to affect nanotoxicity. Glycosylated proteins on the corona were shown to decrease the colloidal stability of gold nanoparticles (AuNPs) as well as the cellular uptake, which resulted in less toxicity [50]. One of the most widely used cell culture medium supplements Penicillin-Streptomycin was also shown to modify the protein corona and induce inflammation in cell cultures [51].

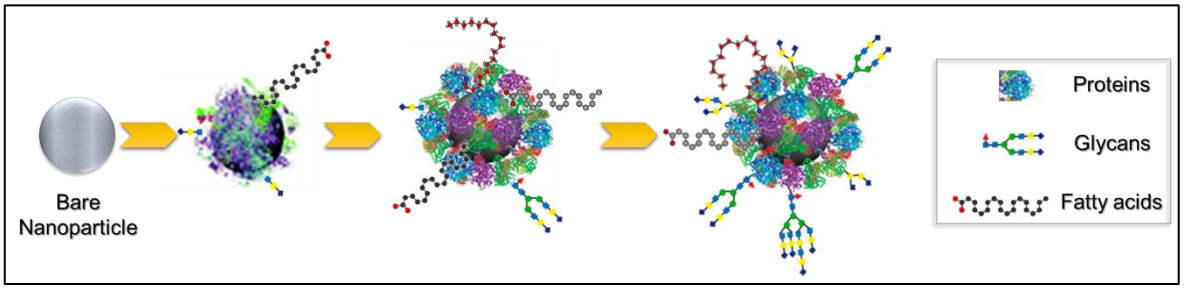

Figure 1.2. Schematic illustration of protein corona evolution on a bare nanoparticle.

Moreover, the corona-coated NMs become almost all what the "cell sees" and are mostly treated or endocytosed depending on their corona composition even though the core of the NM might still exert its characteristics [52]–[55]. The amount of serum proteins on magnetic NPs was shown to alter their uptake efficiency [56]. In the same study, binding of

Apolipoprotein E (apoE) to magnetic NPs increased the crossing across the blood-brain barrier. Therefore, the NM's final destination and effect on the cells might change depending on their corona.

The general routes of cellular uptake processes are shown in Figure 1.3. Mainly, there are two accepted routes; **phagocytosis** (large, solid particles) and **pinocytosis** (uptake of fluids or solutes of various smaller sizes) [57]. Under the pinocytosis category, four major categories also exist.

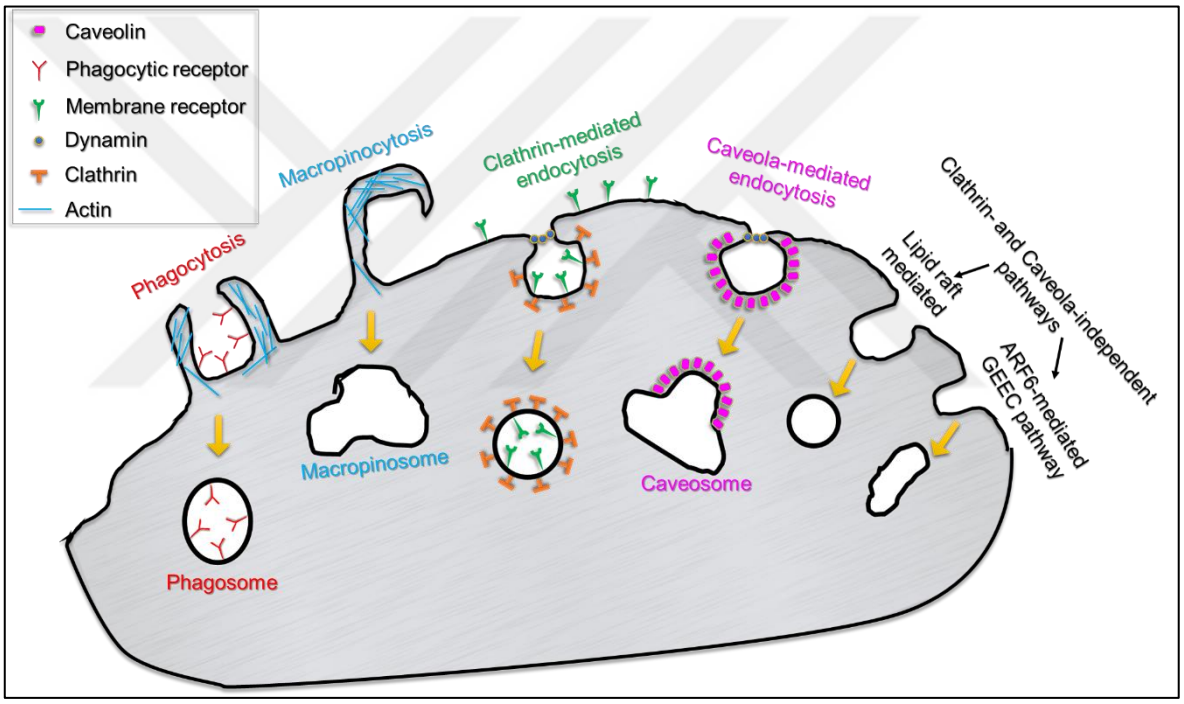

Figure 1.3. Cellular entry routes. (GEEC: Glycosylphosphatidylinositol-enriched endosomal compartments).

Large (> 1 μm) endocytic vesicles are formed upon actin-driven membrane protrusions in **macro-pinocytosis** and it is considered advantageous for pharmaceutical delivery applications due to its large uptake capacity [58]. **Clathrin**- and **caveolin-mediated** endocytosis are two types of receptor mediated pinocytosis routes. Particles of around 120-150 nm size, with an upper limit of 200 nm, are endocytosed via clathrin-coated vesicles. The endocytosis might be initiated either non-specifically by the cationic particles, thus

called **adsorptive pinocytosis**, or through specific receptors [59], [60]. Caveola can be formed by the coating of caveolin-1 and have a diameter of about 50-80 nm [61]–[63]. This route of endocytosis is often associated with non-lysosomal trafficking even though the lysosomal route cannot be excluded completely [64], [65]. Therefore, NMs that are taken up through this route is considered to escape lysosomal degradation and localize in endoplasmic reticulum (ER), Golgi apparatus or cytoplasm. Although the size limits for clathrin- and caveolin-dependent endocytosis are estimated to be 200 nm and 50-80 nm, respectively, there are also studies contradicting with these values. Microspheres ranging from sizes smaller than 200 nm to approximately 500 nm were found to be endocytosed through clathrin-dependent pathway, whereas particles above 200 nm size were also seen to be uptaken through caveolin-dependent pathways [66]. **Clathrin- and caveolin-independent endocytosis** pathways were also reported in the literature. These pathways were shown to rely on the regulation of various proteins such as ADP-ribosylation factor 6 (ARF6) and Ras homolog family member A, and particles with a size larger than 100 nm are thought to be taken up through these routes [67]–[69].

The mostly pronounced and accepted mechanism of NM cytotoxicity is the generation of reactive oxygen species (ROS) [70]–[72]. NM-related ROS production can originate from various reasons in a cell:

- Metal oxide NPs such as TiO_2 NPs can **generate free radicals** [73]. Metallic impurities on other types of NMs such as SWCNTs might also result in ROS generation [74].
- Release of toxic ions can cause reactive hydroxyl radical production through **Fenton-type reactions** as shown in Equation 1.2 [75]:

$$\begin{gathered} M^{n+} + H_2O_2 \rightarrow M^{(n+1)} + HO^{\cdot} + HO^{-} \\ M^{(n+1)+} + O_2^{\cdot -} \rightarrow M^{n+} + O_2 \end{gathered} \tag{1.2.}$$

- **Interaction with the cellular components** such as the respiratory chain in mitochondria might interrupt the normal function and lead to ROS generation [76].
- **Interaction with antioxidants** indirectly leads to an increase in ROS amount [77].

Production of ROS then leads to membrane damage through lipid peroxidation, oxidative disorder, mitochondrial damage, protein adducts, enzyme dysfunction, gene adducts and gene mutations [78], [79]. In a specific cell type, one or more of these outcomes might be observed and the cells might end up with apoptosis, necrosis or autophagy-related cell death. Moreover, as a genotoxic response, cells might carry mutations to daughter cells.

NM interaction with endolysosomal components and dysfunction of the endolysosomal as well as autophagy pathways is an emerging cause of nanotoxicity [80]. Upon NM interaction, lysosomal membranes might become permeable and the leaking ions lead to ROS generation. Dysfunctional lysosomes also lead to the blockade of autophagy. Autophagosomes that contain the proteins and organelles such as mitochondria to be recycled cannot fuse with lysosomes and the non-recycled or waiting-to-be recycled, damaged components lead to massive ROS production [80].

1.3.3. Conventional Nanotoxicity Determination Assays and Their Drawbacks

To evaluate the possible cytotoxicity caused by NMs, conventional *in vitro* cytotoxicity assays have been used. These include; Annexin V-FITC/Propidium iodide (PI) apoptosis/necrosis assay, DCFH-DA ROS detection assay, tetrazolium based cell proliferation assays such as MTT, MTS, WST-1, lactate dehydrogenase (LDH) lipid peroxidation assay, neutral red uptake assay as well as staining the cells with several fluorescent dyes or antibodies to either obtain image-based cytotoxicity information through confocal microscopy or quantitative information through flow cytometry [70]. However, it was shown in many cases that not all assays give accurate results with all types of NMs [81]. As mentioned in the previous sections, NMs might possess several different physicochemical properties compared to their bulk counterparts. These unique properties lead to end up with absorbance artifacts in the assays in most cases because NMs can alter the light emission, absorbance or fluorescence characteristics through enhancing or quenching the fluorescence of the medium they are in [71], [82]–[85]. For instance, NMs with an absorbance peak between 400-600 nm range cause false negative values of cytotoxicity in assays based on colorimetric detection of dyes, such as MTS, at these wavelengths. CdSe QDs are one good example to this issue. In a study by Ong and coworkers, 547±224 cells were counted as alive in MTS assay where there were actually no

cells in the tested QD-containing medium [86]. The value even got higher, 1297±50, when Alamar blue assay was used.

Because of their similar size range, NMs can also directly interact with enzymes in enzyme based cytotoxicity assays [87], [88]. Lactate dehydrogenase, amount of which is detected in LDH assay, was shown to interact with many types of NMs [87]. Adsorption of the enzyme to NM surface causes a reduced value in the detected amount of LDH leaked from the cells, thus an overlooked cytotoxicity.

1.3.4. Alternative Nanotoxicity Evaluation Methods

The uncertainties introduced by NMs in assay results have driven researchers worldwide to form a consensus on how to evaluate nanotoxicity. Many initiatives published their findings and several meetings helped to take a step further for the development of protocols and nanotoxicity evaluation approaches. Examples to work groups include; NANoREG, Managing Risks of Nanomaterials (MARINA), Organization for Economic Co-operation and Development Working Party on Manufactured Nanomaterials (OECD-WPMN), NANOVALID, ONE Nano, and Nanosafety Cluster Working Group 10 [23], [24], [89]–[92]. In addition to their informative reports, there are collective statements from scientists stressing the importance of improved approaches and how to achieve them [93]–[97]. The trend observed from the reports is that creating decision trees, grouping NMs, reconsidering the dosimetry of the particles in the tested system, and read-across approaches are needed and are currently being developed. Furthermore, *in silico* predictive methods are believed to be of benefit, especially in the reduction of number of animals used or the better usage of funding sources [98], [99].

On the *in vitro* nanotoxicity evaluation side, some practical solutions to the existing problems were proposed [84]. These include; separating NMs from the solution containing assay contents via centrifugation or filtration, washing the cells, lowering the NM concentration to be tested, confirming the results with other non-optical spectrometry-based cytotoxicity tests, performing cell-free assays to test NM interference prior to nanotoxicity evaluation. It is also acknowledged by the scientists in the field that more accurate assays are sought with minimal or no interference by NMs, whereas being fast and easy to implement. In an attempt to solve the interference issue, several alternative methods were

proposed such as atomic force microscopy (AFM)-based cell mechanics investigation, mass spectrometry-based redox proteomics, cell impedance-based analysis as well as high throughput screening and high content analysis of cells [100]–[104].

1.4. VIBRATIONAL SPECTROSCOPY

The interaction of electromagnetic radiation with matter and the observable effects of these interactions have been the topic of various spectroscopy techniques. Such an interaction might result in ionizing, electronic, vibrational and rotational transitions in molecules (Figure 1.4), which can be detected via; X-ray spectroscopy, UV-Visible (UV-Vis) or fluorescence spectroscopy, infrared (IR) or Raman spectroscopy and microwave rotational spectroscopy, respectively.

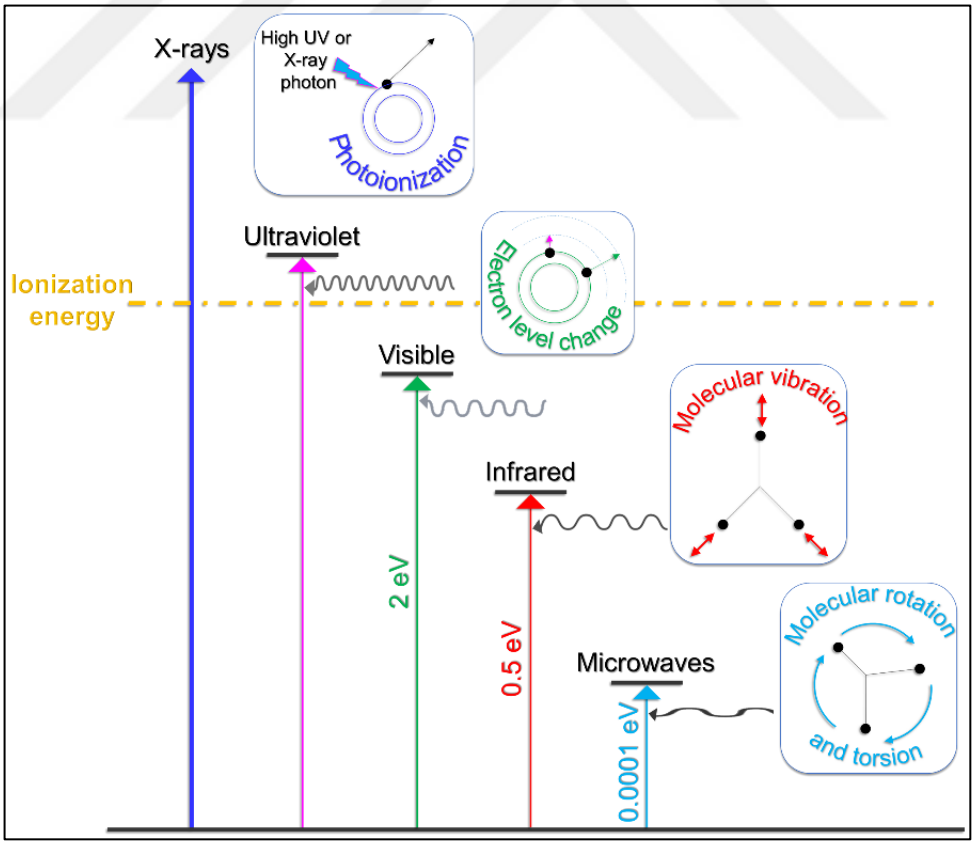

Figure 1.4. The interaction of electromagnetic radiation with matter.

Among these molecular transitions, information on the secondary structures or modifications in the local environment of molecules can be extracted by applying vibrational spectroscopy techniques. As mentioned above, IR and Raman spectroscopy are two techniques to detect molecular vibrations. Due to their differences in working principles, they are widely used as complementary techniques [105]. The principles of these vibrations and the mechanisms of infrared absorption and Raman scattering were summarized from the general chemistry books and the related references can be found in [106]–[111] for "Section 1.4" and its subsections.

1.4.1. Molecular Vibrations

Molecules in space possess three types of degrees of freedom (DOF), namely;

- Translational – movements on x, y and z axes as a whole,
- Rotational – movements on orthogonal axes,
- Vibrational – movements in the bonds within the molecules, as can also be seen in Figure 1.5.

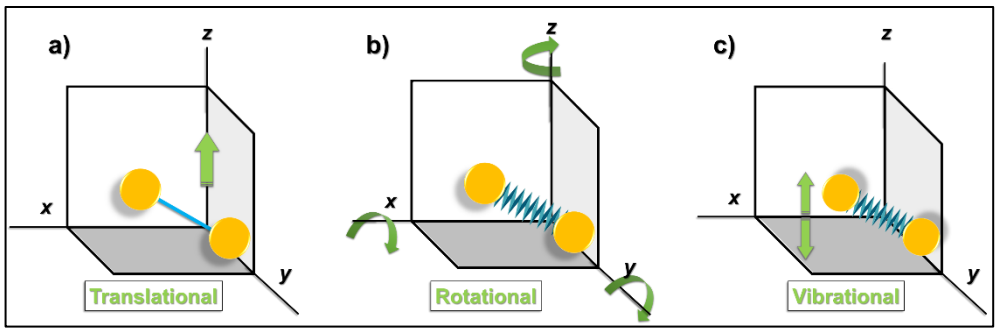

Figure 1.5. Molecular degrees of freedom. **(a)** Translational, **(b)** rotational, and **(c)** vibrational movements in x, y, and z axes.

Thus, in a given molecule, there are "*3N*" DOFs, "*N*" being the number of atoms in the molecule. In the case of a linear molecule, three of these DOFs are translational and two are rotational, whereas in a non-linear molecule the rotational DOFs are three instead of two.

Therefore, for any given linear molcule, there are "*3N-5*"vibrational modes and "*3N-6*" for non-linear ones.

Depending on the type of the molecule, the vibrational modes can be stretching, bending (deformation) or in some cases a coupling between various vibrations. These modes are also summarized in Figure 1.6. Stretching vibrations can be either symmetric or asymmetric. Bending or deformation vibrations can be either in-plane, as in the case of rocking and scissoring, or out-of-plane, as in the case of wagging and twisting.

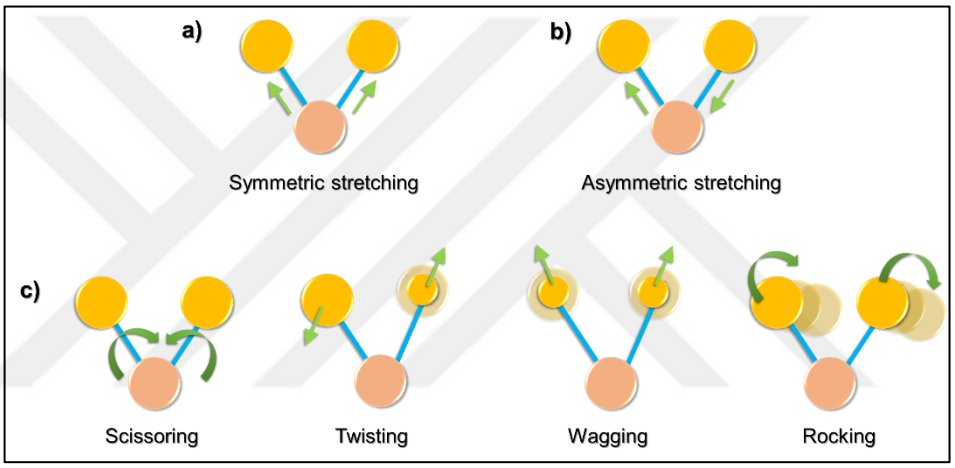

Figure 1.6. Vibrational modes **(a)** Symmetric stretching, **(b)** asymmetric stretching, **(c)** bending and deformation vibrations.

1.4.2. IR Spectroscopy

In IR spectroscopy, the incident light at IR region of the electromagnetic spectrum causes a change in the dipole moment of a molecule at specific frequencies matching the frequency of its bond vibrations which then causes absorption of a certain amount of the incident light. Therefore, in an IR spectrum, the percentage of the transmitted light at certain wavenumbers, one over wavelength in centimeters (cm^{-1}), is shown. For instance, as shown in the IR spectrum of acetone in Figure 1.7, at wavenumber 1715 cm^{-1}, about 100 per cent of the incident light was absorbed by the molecule, which means the bonds vibrate at the same

frequency with this wavenumber. However, at 3000 cm^{-1}, 30 percent of the light was absorbed, meaning the rest was transmitted [112].

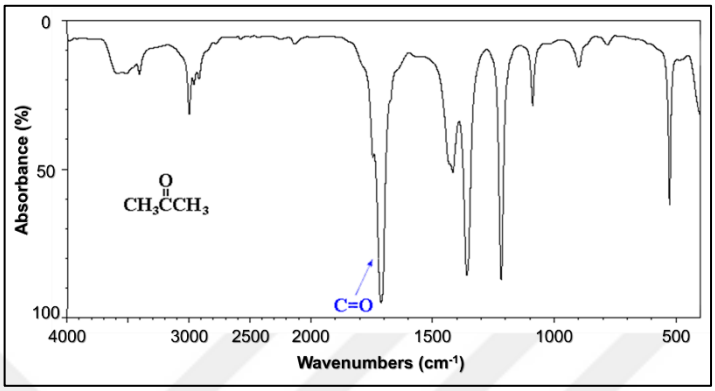

Figure 1.7. IR spectrum of acetone [112].

The main difference between IR absorption and Raman scattering comes from the response of bond vibrations due to their characteristics. For a molecular vibration to be IR active, the incident light should cause a change in dipole moment on that specific bond. Therefore, asymmetric bond vibrations are IR active since symmetric vibrations are not easily polarized to cause a change in their dipole moments. On the other hand, for a vibration to be Raman active, the bond should be polarizable upon the interaction with the incident light. The polarizability level is determined by the interaction of the nucleus with its surrounding electron cloud. For instance, molecules with large nuclei and many electrons cannot strongly attract their electron clouds around them, especially the ones furthest to the nuclues and this causes higher polarizability. Unlike IR absorption, Raman active bond vibrations are symmetric, since these vibrations are more easily polarizable compared to asymmetric ones.

1.4.3. Raman Scattering

As a difference from IR spectroscopy, where there is an absorption of photons, Raman spectroscopy is interested in the detection of scattered photons. Molecules, which are mostly found in ground vibrational states in nature, have the ability of absorption or scattering of incident photons. Characteristic to the organization of their electron orbits, they have

allowed energy levels to jump to an excited state, to a virtual state between the ground and excited states or to remain as they are. Upon such interactions, they also have the possibilities of either absorption, emission or scattering photons at various energies. These possible phenomena are summarized in Figure 1.8.

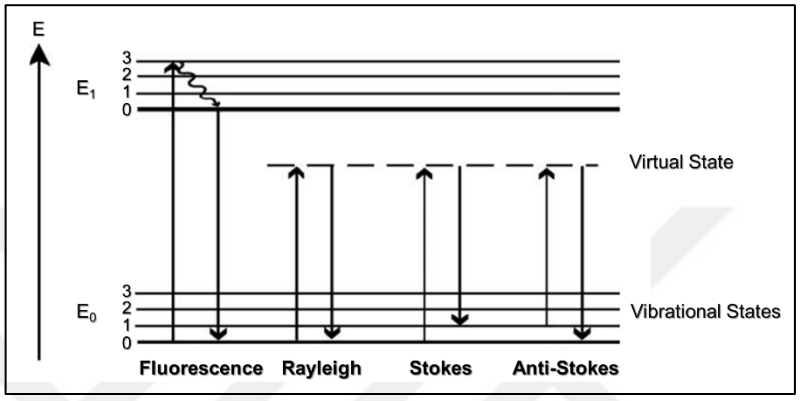

Figure 1.8. Jablonski diagram depicting fluorescence, Rayleigh, Stokes and anti-Stokes scattering [113].

If the incident light causes excitation to a higher electronic state and photon emission occurs at a longer wavelength, which means a loss of energy, then this is called **fluorescence**. If the incident light causes increase to a virtual energy state and the scattered photons are at the same wavelength, it is called **Rayleigh scattering**. On the other hand, if the scattered light has lost some of its energy, the phenomenon is called **Stokes scattering**. If the scattered light gains more energy, then it is called **anti-Stokes** and these two types of inelastic scattering are called in general as **Raman scattering**.

Since molecules are mostly found in ground state, the rate of anti-Stokes scattering is much smaller than Stokes scattering and these two comprise a very small portion of scattered photons ($\sim 10^{-7}$) compared to Rayleigh scatteres photons. In a Raman spectrum, the change in vibrational levels of Raman active bond vibrations are plotted in wavenumbers (cm^{-1}) (Figure 1.9). Although their occurrence rates are different, both Stokes and anti-Stokes shifts occur at same wavenumbers in a Raman spectrum, anti-Stokes shifts having negative values on x-axis.

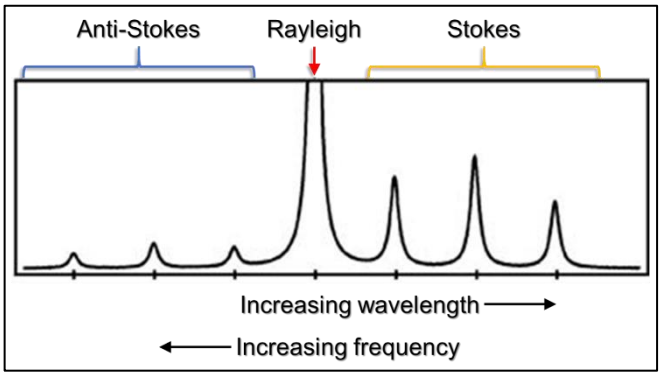

Figure 1.9. Representative Raman spectrum showing the Stokes, anti-Stokes, and Rayleigh scattering.

1.5. INSTRUMENTATION AND MODALITIES OF RAMAN SCATTERING

A typical modern Raman spectrometer consists of four units; **excitation source**, **light collection and distribution optics**, **wavelength selector**, and **detector** (Figure 1.10) [114]. In this section, the instrument that was used in the present work, Renishaw inVia Reflex, will be based on and its compartments will be explained.

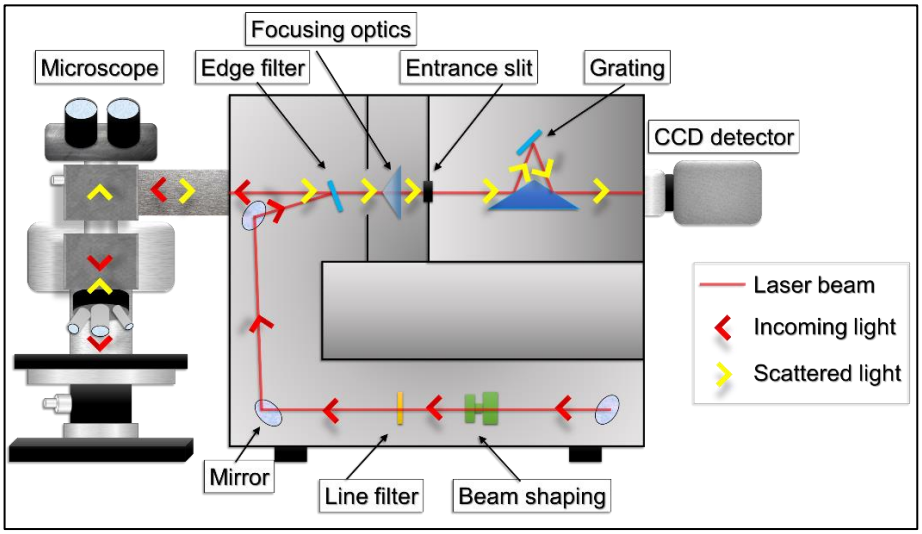

Figure 1.10. Instrumental components of a Raman spectrometer.

The excitation source, a photodiode laser of 830 nm wavelength, provides the laser beam and the beam first passes through the beam shaping optics. The line filter blocks all other light except the laser line. The light is directed through mirrors to hit the edge filter, which blocks the Rayleigh scattering to transmit the path to the detector but allows the Stokes Raman signals at a high transmission capacity. As a side note here, instead of an edge filter, a notch filter can also be used to obtain both Stokes and anti-Stokes scattering. The laser that hits the sample causes Raman scattering that will be condensed through the microscope optics and directed back to the edge filter. Then, the scattered signals are condensed through focusing optics to pass through the entrance slit where the light is directed to the grating optics to be diffracted and finally hit the charge-coupled device (CCD) detector.

Alternative instrumental setup allows to work with various modalities of Raman spectroscopy and enhance the extent of information that can be gathered from the sample of interest. For instance, single molecule or single cell characterization as well as manipulation can be made by the help of optical tweezers, where the sample of interest is optically trapped by the laser beam and can also be directed to a microchannel for sorting [115], [116].

To suppress the background fluorescence that can be problematic in biological samples, due to their autofluorescence, coherent anti-Stokes Raman scattering (CARS) and stimulated Raman scattering (SRS) can be utilized. In CARS, anti-Stokes scattering is acquired where the fluorescence does not interfere with the signals. SRS, where multiphotons hit the sample and the signals are thus enhanced, provides even better resolution over CARS [117], [118].

For thick samples, spatially-offset Raman spectroscopy (SORS) can be utilized where the location of incident laser beam and the collected Raman signals are spatially offset [119]. Similar to SORS, transmission Raman spectroscopy (TRS) enables the analysis of thick samples, as thick as 10 mm [120], [121]. In TRS, the Raman signals are collected from the opposite side of the sample where the laser beam hit. Therefore, it is not possible to obtain information from the different layers of the sample compared with SORS but the system enables acquiring spectra from the inner side of materials where the surface layer is not a matter of interest, as in the case of pharmaceutical investigations where the spectrum originating from the drug capsules are not desired [121].

To enhance the low Raman signals, confocal Raman, surface-enhanced Raman (SERS), tip-enhanced Raman (TERS), and surface-enhanced resonance Raman (SERRS) spectroscopies

are commonly used modalities [122]–[127]. Confocality provides an increase in spectral resolution by focusing on a narrower region on the sample. For SERS, TERS, and SERRS, basically a rough metal surface is made use of to enhance the weak Raman signals. The SERS enhancement mechanism will be explained in the next section in detail. The difference between the three modalities is that in SERS, often a noble metal nanoparticle colloid or a rough surface is used and in TERS, a tip is coated with such material, whereas in SERRS, a molecule that can resonate at the specific frequency also adds to the surface enhancement provided by the SERS substrate.

1.6. SURFACE-ENHANCED RAMAN SCATTERING

The discovery of SERS dates back to early 1970s and the history of early work is exciting to mention. One of the pioneers of the field, Richard P. Van Duyne, explained the discovery and theoretical understanding process of SERS phenomenon in a paper published in 2005 [128]. Summarizing his words in this section would be beneficial to understand the process but interested readers are highly encouraged to read the full story from his own words.

During early 1970s, the vibrational spectroscopy community was highly interested in obtaining spectra from a solid surface with a monolayer of molecules adsorbed on to study, for instance, solid-liquid interfaces in electrochemistry to probe the electrochemical environment. Although IR spectroscopy was being studied, Raman spectroscopy studies were yet to be investigated. Van Duyne was one of those researchers that was trying to improve the weak Raman signals. He first made theoretical calculations on a non-resonant molecule, pyridine, to adsorb on the electrode surface but found out that the signal intensity would be about 25 counts, which would not be useful. Therefore, he moved on to improving Raman cross section by utilizing resonance Raman effect. With the preliminary results as well as the theoretical calculations he made, he was just about to submit a research proposal on improved resonance Raman scattering from molecules adsorbed on electrode surface in May 1974, when he saw the article published in the journal Chemical Physics Letters by Fleischmann's group [123]. They reported up to 1000 counts from pyridine adsorbed on a roughened silver electrode at similar settings. In that study, they have also showed that the peaks shifted with the increased and decreased anodic potentials; demonstrating that it was possible to observe whether pyridine was adsorbed on the surface or was very near to it.

Being confused with their findings, Van Duyne had a chance to meet Fleischmann in September 1974 and was invited to visit his laboratory to discuss with McQuillan, the coauthor of Fleischmann's article, to figure out what he was missing when he calculated very low signal intensity from pyridine. Increased surface roughness was proposed to him as the key point; a rough electrode surface would enable more pyridine to be adsorbed on the electrode. Back in his laboratory to replicate Fleischmann's work, it was actually discovered that surface roughness was not the only contributor and indeed lower roughness than the one applied in the paper resulted in even higher Raman intensities. His graduate student, Jeanmarie, worked on the optimization of surface roughness and successfully obtained about 10^5-10^6 times enhanced Raman signals which was not possible to be attributed only to increased surface area. Their outcomes directed them to investigate further this new type of Raman scattering phenomenon. After a long "submit-be rejected" cycle, in October 1976, he submitted an extended report on his findings to Journal of Electroanalytical Chemistry where the article was accepted to be published on May 1977 and eventually get published in November that year [124]. An electric field enhancement was proposed as being responsible of the intense signals. Meanwhile in May 1977, Van Duyne attended Optics at the Solid-Liquid Interface Conference, where he met physicists that opened the way up to him to learn more about surface plasmons and together developed the **electromagnetic field enhancement (EM) theory** of SERS [129].

During his report submission process, in May 1977, he also received a review request from Journal of American Chemical Society of a report by Albrecht and Creighton with the title "Anomalously Intense Raman Spectra of Pyridine at a Silver Electrode" [125]. However, he thought at that time that their results were almost identical to the article he submitted. Thus, he rejected the article even though it was published in that journal in July 1977. In that report the observed phenomenon was explained to originate from the charge transfer absorption from the surface to the adsorbate which caused resonance Raman scattering. The mechanism is now accepted as the **chemical enhancement (CE) theory** of SERS.

These two theories, EM and CE, are accepted as the main mechanisms of SERS effect today. Localized surface plasmons on the surface of nanostructured metals oscillate with the incoming laser beam at an appropriate frequency and create an electromagnetic field gradient. The optimal wavelength of a laser light to create higher oscillation is where the metal-specific localized surface plasmon resonance (LSPR) peak is. If the molecule that was

polarized upon interaction with the incoming laser beam have vibrational modes that moves in line with the electromagnetic field gradient of the SERS substrate, Raman peaks belonging to these modes are seen as enhanced in the observed spectrum. This is because the polarizability of the molecule is increased by the help of the oscillations occurring in the electromagnetic field gradient. The enhancement factor of EM mechanism is about 10^5-10^6 times whereas the value is between 10^0 to 10^3 for CE mechanism [130]. For CE, three sub-mechanisms were proposed; resonances originating either from molecular excitation or charge transfer between the substrate and the molecule, and non-resonant changes in the polarizability of the molecules [131]–[133]. In CE-related mechanisms, the level of enhancement might be affected from the orientation and distance of the molecule to the substrate surface or the level of interaction between the electron systems of the molecule and substrate surface.

1.6.1. Biological Applications of SERS

The ability of SERS to detect molecules even at very low concentrations as well as its ease of analysis with simple sample preparation, opened the way up for a broad application field ranging from biosensors to spectroelectrochemistry, forensics, art preservation or archeology [134]. Application of SERS in biological research has also become a growing area of interest. It is now possible to monitor drug release, detect yeasts, viruses and other microorganisms, or map cell surface markers on cells by utilizing SERS [135]–[139]. Even the detection of potential cancer markers that could not be detected with conventional immunoassays, such as ELISA, has been accomplished from the serum of patients [140, p. 4]. Low limit of detection (LOD) provided by the technique is promising in clinical decision procedures for faster and more accurate treatment strategies [141]. Although modalities such as CARS and SORS are more widely investigated for *in vivo* studies for their higher penetration depth, the first *in vivo* SERS study was reported already in 2008, followed by a multiplexed SERS nanotag imaging *in vivo* on mice in 2009 [142], [143].

Besides tissue or body fluid detection, another highly informative application field of SERS is single cell analysis considering the fact that it enables label-free, non-invasive and living cell monitoring. The very first living cell SERS analysis report dates back to 1991 by Nabiev and colleagues where they observed the differences between the interaction of doxorubicin,

a DNA intercalating anticancer drug, with the cytoplasm and nucleus [144]. Later, with the advancement of instrumentation, especially the laser and detector technologies, the studies expanded from intracellular pH changes to endosomal maturation, small molecule detection, circulating tumor cell detection, or cell cycle and apoptosis dynamics, all of which are challenging and hot topics of biological research [145]–[150]. With the use of targeting moieties, SERS substrates can also be directed to various cellular compartments, such as nucleus and mitochondria, to acquire organelle-specific information [151].

The use of SERS tags is also an option with unique profits especially when SERS is modified for multiplexed cell imaging. In the SERS-tagged approach, surface of the SERS substrates are conjugated with reporter molecules. Depending on the presence or absence of the reporter, desired information, such as pH or the presence of a specific molecule, can successfully be extracted. Details of the approach are not in the scope of this work but more detailed information can be read from a well-written review by Wang and colleagues [152].

Here, it should be noted that only molecular vibrations can be detected with any Raman scattering modality. Thus, in a complex structure like a eukaryotic cell, it can be extremely chaotic to understand or interpret the obtained spectra. What creates this complexity originates from the nature of vibrational spectroscopy techniques. In a SERS spectrum, the obtained peaks are a combination of various bond vibrations such as C-C, C-S, C-H or C-N. The cellular components are made up of molecules such as carbohydrates, lipids, and proteins which also have C-C, C-S, C-H or C-N vibrations. Therefore, it is not possible to pinpoint, for instance the expression of a random protein as in the case of immunoassays. However, the technique conveniently provides information on the cellular dynamics and chemical milieu at stimulated or other conditions as mentioned previously in this section. The information includes the changes in the protein α-helix to β-sheet conformation, lipid type and abundancy or nucleic acid abundancy.

Another SERS concept-related point that should be kept in mind before making any spectral interpretation is the accumulation dynamics of the SERS substrate because the observed bands in a SERS spectrum are the overall information of the close vicinity of the substrate. Therefore, substrate localization plays a vital role and should be evaluated carefully in cellular SERS studies.

2. OBJECTIVES OF THE STUDY

Utilization of label-free SERS in single-cell analyses as a promising powerful approach, and its potential to bypass NM-related assay interferences were the two driving forces of this thesis work. It was mainly aimed to develop and optimize a living-cell SERS analysis method to detect cellular changes upon NM exposure and evaluate nanotoxicity based on the obtained SERS spectral patterns.

There were several points to be cleared to accomplish this aim and a stepwise approach was required. First of all, the extent of nanotoxicity should have been evaluated carefully to avoid assay-related drawbacks mentioned in the previous sections because the results obtained from these studies would be correlated to the observed SERS spectra upon NM exposure.

Then, SERS experimental setup needed to be optimized. This brought up additional concerns, mostly originating from the nature of SERS, that were:

- In which compartments of the cells were the SERS substrates located?
- To what extent the corona around the substrate contributed to the SERS spectra?
- What were the origins of the observed spectral pattern?

Upon finding answers to these questions, observed spectral peaks were investigated to find spectral markers that would point out nanotoxicity.

Through testing a panel of NMs with various size, shape, and chemical composition on several cell lines of distinct tissue origins, it was aimed to demonstrate the discrimination power of the developed method.

3. MATERIALS AND METHODS

3.1. MATERIALS

3.1.1. Cell Lines

A549 (human Caucasian lung carcinoma), HSF (human skin fibroblast), HUVEC (human umbilical vein endothelial cell), and L929 (mouse fibroblast from connective tissue) cell lines were purchased from American Type Culture Collection (ATCC).

3.1.2. Cell Culture Reagents

Dulbecco's Modified Eagle Medium (DMEM) with high glucose content (catalog #D6429), Dulbecco's Modified Eagle Medium: Nutrient Mixture F-12 (DMEM/F-12) (catalog #6421), fetal bovine serum (FBS) (catalog #F7524), and phosphate-buffered saline (PBS) (catalog # D8537) were purchased from Sigma-Aldrich®. Trypsin-EDTA (catalog #25200056), Penicillin-Streptomycin (catalog # 15140122), and L-Glutamine (catalog # 25030081) were purchased from Gibco®.

3.1.3. Nanomaterials

Zinc oxide nanoparticles (ZnO NPs) were purchased from TecStar, anatase form TiO_2 NPs were from Alfa Aesar® (catalog #044690), SWCNTs (catalog #704148-1G) and MWCNTs (catalog #406074-1G) were from Sigma-Aldrich®. The QDs that were used in this thesis were CdSe/ZnS/MS/hydr QDs and they were purchased from PlasmaChem GmbH.

3.1.4. Kits and Chemicals

The nuclear stain DAPI (catalog #D1306) was purchased from Molecular Probes®. Gluteraldehyde (catalog #G5882), and gold (III) chloride trihydrate (catalog #G4022) were

from Sigma-Aldrich, sodium citrate was from Merck Millipore (catalog #1064321000). Dow Corning Sylgard 184 Silicone Elastomer Clear was used for polydimethylsiloxane (PDMS) coating over Petri dish.

Cell proliferation reagent WST-1 (catalog #11644807001) was purchased from Roche. Apoptosis/necrosis detection kit was purchased from CalbioChem (catalog #PF032).

3.2. CELL CULTURE

A549 and L929 cell lines were cultured in DMEM/F-12 supplemented with 10 per cent fetal bovine serum (FBS), 1 per cent Penicillin-Streptomycin and 2 mM L-Glutamine. HSF and HUVEC cell lines were cultured in DMEM with high glucose content supplemented with 10 per cent FBS and 1 per cent Penicillin-Streptomycin. Cells were incubated in an incubator at 37°C with 5 per cent CO_2 humidified atmosphere.

For SERS studies, 7.5×10^3 cells for HSF cell line, 10^4 cells for HUVEC cell line, and 1.5×10^4 cells for A549 and L929 cell lines were seeded on calcium fluoride (CaF_2) slides. CaF_2 slides were cut into 1 cm^2 pieces beforehand to prevent fracture of the slides as well as to be able to use 24-well culture plates to place the slides for NM exposure.

For WST-1 assay and enhanced- dark field (EDF) microscopy, the same amount of cells as for SERS studies were seeded on 96-well plates and round glass coverslips, respectively.

For Annexin V-FITC/PI apoptosis-necrosis assay, 3×10^4 cells for HSF cell line, 3.5×10^4 cells for HUVEC and L929 cell lines, and 4×10^4 cells for A549 cell line were seeded on each well of a 24 well-plate in triplicates. For Transmission electron microscopy (TEM) imaging, 2.5×10^5 A549 cells were seeded on each well of a 6-well plate.

3.3. GOLD NANOPARTICLE SYNTHESIS

Spherical AuNPs of 60 nm diameter size were synthesized by citrate reduction method [153], [154]. Briefly, 0.01 per cent gold (III) chloride trihydrate ($HAuCl_4$) in 100 ml deionized water was boiled. Then, 0.8 mL of 1 per cent sodium citrate was added into the boiling solution. The solution was kept boiling for 15 minutes. The final AuNP colloid was left to

cool down at room temperature before characterization and was stored at room temperature in the dark. The colloid was stable for several months at these conditions.

3.4. NANOMATERIAL DISPERSION

To disperse purchased powder-form NMs, serum-free cell culture medium of each respective cell line was used; DMEM with high glucose content for HSF and HUVEC cell lines and DMEM-F12 for A549 and L929 cell lines. Dispersion was carried out as six cycles of 90 seconds sonication in a cooled ultrasonication bath and one minute "vortex-wait". The vortex step consisted of three cycles of five seconds vortex and five seconds wait. The remaining time in "vortex-wait" cycles was considered as "waiting".

3.5. NANOMATERIAL CHARACTERIZATION

The dispersed NPs and synthesized AuNPs were characterized via UV-Vis spectroscopy (Lambda 25, Perkin-Elmer, Foster City, CA, USA), TEM (JEM-2100, Peabody, MA, USA), and dynamic light scattering (DLS) (ZetaSizer Nano ZS, Malvern Instruments, Malvern, UK) measurements.

3.6. NANOMATERIAL EXPOSURE TO CELL CULTURE

Cells were incubated with NPs for 24 h at increasing concentrations that were chosen from the literature to provide a concentration range corresponding with the low, middle and high levels of cytotoxicity. Therefore, 5, 10, 15, 20 µg/ml for ZnO NPs; 20, 40, 60, 80, 160 µg/ml for anatase TiO_2 NPs, 0.1, 0.25, 0.5, 1 mg/ml SWCNTs and MWCNTs, and 5, 10, 25, 50 µg/ml for QDs were used as final concentrations in the culture vessels. Additionally, 1.6×10^{15} of AuNPs (corresponded to 25 µg/ml $HAuCl_4$ of the synthesized AuNPs) were added simultaneously to the incubation medium to make up 25 per cent (v/v) of the 1 ml in each well of a 24-well plate for SERS analyses, apoptosis-necrosis assays and EDF microscopy. For WST-1 assay, the total incubation medium was 100 µl for 96-well plates. For TEM samples total medium was 3 ml in 6-well plates.

3.7. APOPTOSIS/NECROSIS ASSAY

To determine the rate of apoptotic and necrotic cells upon NM exposure, apoptosis and necrosis detection kit from Calbiochem (Merck Millipore) was used according to manufacturer's instructions. Upon NM exposure, the supernatant containing the detached cells were collected in a test tube. Then, attached cells were trypsinized and collected in the same test tube. After centrifugation, the cell concentration was adjusted to 10^6 cells per ml and stained with Annexin V-FITC as well as with PI. The samples were kept on ice until analysis. For each sample, triplicates of 2×10^4 events were collected on *guava easy-Cyte*™ *5* (Merck Millipore) benchtop flow cytometer. Cells that were stained with only Annexin V-FITC were labeled as "early-apoptotic", stained with both Annexin V-FITC and PI as "late-apoptotic", and stained only with PI as "necrotic", whereas the non-stained cells were "alive".

3.8. WST-1 CELL PROLIFERATION ASSAY

Following NM exposure for 24 h, cells were washed once with phosphate buffered saline (PBS) and incubated with WST-1 containing complete medium for one hour at 37°C, at 5 per cent CO_2 in a humidified incubator. Upon incubation, supernatant was transferred to a new 96-well plate to prevent NM interference during absorbance measurement [84]. Absorbance values were read by a microplate reader at 450 nm (ELx808, BioTek, Winooski, VT, USA). Results were plotted as per cent cell viability. On the statistical software, SPSS, one-way ANOVA with a Tukey's post-hoc test was applied to test the effect of NP incubation compared to control samples that were incubated with only AuNPs. Samples with a $p\leq0.05$ significance value were marked with a star sign.

3.9. TRANSMISSION ELECTRON MICROSCOPY

Cells were first fixated with 2.5 per cent glutaraldehyde. Then they were dehydrated in ethanol series of 30, 60, 70, 80 and 100 per cent ethanol concentration. Thin sections of about 70-100 nm thickness were obtained from the Epoxi resin-embedded samples using a LKB ultramicrotome equipped with a diamond knife. Samples mounted on copper grids

were stained with 2 per cent aqueous uranyl acetate and lead citrate. Images were obtained by using a JEOL 1200 EX microscope operating at 80 kV.

3.10. ENHANCED-DARK FIELD MICROSCOPY

For EDF microcopy cells on coverslips were first fixated with 2.5 per cent gluteraldehyde and stained the nuclei cells with DAPI for five minutes. After mounting the samples, a Cytoviva® enhanced-dark field condenser attached to an Olympus BX51 upright microscope, which is equipped with a fluorite 100× objective and a DAGE CCD camera. By using the UV excitation of Cytoviva® Dual Mode Fluorescence system, DAPI nuclear staining was visualized. After obtaining the images the dark field images were merged with transmission fluorescence images using the image processing software GIMP by using the "Addition" function.

3.11. SERS EXPERIMENTAL SETUP

Cells on CaF_2 slides were washed once with PBS and were directly moved onto a PDMS coated polystyrene Petri dish. Because the cells were seeded on CaF_2 slides that were cut into small pieces, it was practical to carry out the measurements by placing the slides on a Petri dish. The PDMS coating suppressed the polystyrene peaks that could originate from the dish. Cells were not fixated for the measurements to prevent additional fixation-related issues such as fixative-originated peaks in the spectrum and spectral changes due to chemical fixation or cell drying [155]. A drop of serum-free cell culture medium was added on CaF_2 slides to prevent the cells from drying throughout SERS measurements. Unless otherwise was stated, for all SERS measurements, a Renishaw inVia Reflex Raman spectrometer equipped with a high speed encoded stage (Streamline™), a Leica DM2500 upright microscope and an 830 nm photodiode laser source with 1200 line/mm grating was used. The laser spot size was approximately 2.5 μm on the sample where Leica 20× long distance objective (N.A.=0.40) was used. Because the sample was in liquid and a long distance objective was used, the laser power was kept at 150 mW with two seconds exposure time to obtain efficient signals.

The measurements were carried out at a chosen area of approximately 30×30 μm with 2 μm step size. By the help of the high speed encoded stage, mapping an area of this size took about 4-5 minutes. The spectral acquisition range was set to 1473-473 cm^{-1} with a 0.9 cm^{-1} spectral resolution. A minimum of four cells were scanned on a CaF_2 slide and a minimum of 50 cells were scanned for each test group.

3.12. SERS DATA PROCESSING

The spectra obtained from a single-cell were pre-processed and averaged to yield a spectrum representing that single cell. Acquired spectra were background corrected, smoothed by Savitzky-Golay filtering, vector normalized to unit one and cosmic spikes were removed. All the averaged spectra from each single cell of a test group were averaged once again to obtain a representative spectrum of that specific test group.

3.13. GOLD NANOPARTICLE CORONA EXPERIMENTS

AuNPs were incubated in DMEM cell culture medium with 10 per cent FBS for 24 h to allow corona formation. The suspension was centrifuged at 23000 g for 20 minutes. Then, a set of samples containing AuNP pellets were resuspended in 20 μl deionized water and heated to 37°C, 42°C, 55°C or 72°C for 10 minutes. Other two sets of samples were incubated with 20 μl of increasing concentrations of hydrogen peroxide (H_2O_2) (0.18 μM, 1.8 μM, 18 μM, 180 μM) or trypsin-EDTA (2.5 μg/ml, 25 μg/ml, 250 μg/ml, 2500 μg/ml) for 30 minutes. Upon each type of incubation, test tubes were again centrifuged and 3 μl from the pellet was placed on a CaF_2 slide. The drop was air dried upside down at ambient conditions before the SERS measurement. The rest of the pellet was diluted in deionized water for UV-Vis and DLS characterization. To rupture the cells, cells were first incubated in deionized water for 30 minutes in the incubator, then sonicated in the ultrasonicator bath for 30 minutes.

4. RESULTS AND DISCUSSIONS

4.1. NANOMATERIAL CHARACTERIZATION

NMs were characterized prior to each experiment and the summary of characterization results were given in Figure 4.1 with their respective standard deviation values in the inset table.

Although ZnO NPs and AuNPs (Figure 4.1a and j) were more homogenous in cell culture medium, TiO_2 NPs, SWCNTs, and MWCNTs (Figure 4.1b-d) had a tendency to agglomerate, thus their standard deviation values were higher. QDs also had a tendency to agglomerate (Figure 4.1i). However, because the large agglomerates tended to quickly sediment down to the measurement tube, only the dispersed particles were able to be measured, leading to a small standard deviation.

TEM images were confirmative to the DLS results. ZnO NPs were more dispersed compared to TiO_2 NPs (Figure 4.1e and f). SWCNT and MWCNTs were in the size range that was stated by the producer company (Figure 4.1g and h). QDs were seen as agglomerates but were also in the size range that was stated by the producer company (Figure 4.1l).

AuNPs were also characterized by using UV-Vis spectrophotometer, that is an established standard in AuNP characterization [156]. The absorbance peak was located at 527 nm.

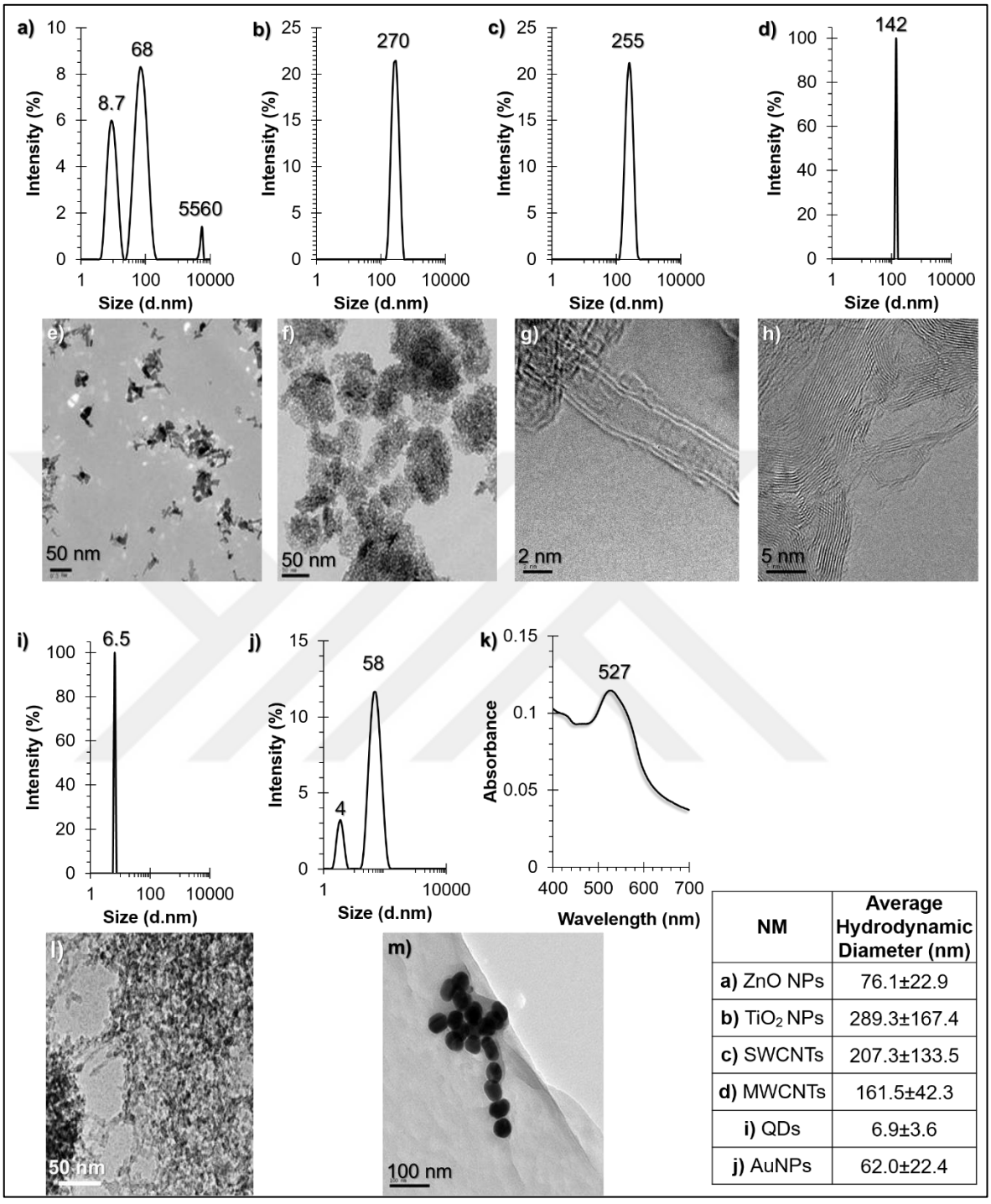

NM	Average Hydrodynamic Diameter (nm)
a) ZnO NPs	76.1±22.9
b) TiO_2 NPs	289.3±167.4
c) SWCNTs	207.3±133.5
d) MWCNTs	161.5±42.3
i) QDs	6.9±3.6
j) AuNPs	62.0±22.4

Figure 4.1. NM characterization results. **(a, b, c, d, i, j)** DLS plots and **(e, f, g, h, l, m)** TEM images of ZnO NPs, TiO_2 NPs, SWCNTs, MWCNTs, QDs and AuNPs, respectively. **(k)** UV-Visible absorbance spectrum of as-synthesized AuNPs. The average hydrodynamic diameters of the used NMs and their standard deviation were summarized in the table.

4.2. TESTING THE EFFECT OF NANOMATERIALS ON CELLS WITH THE CONVENTIONAL CYTOTOXICITY ASSAYS

The cytotoxicity of NMs were evaluated by two widely used assays in parallel with the SERS measurements. To each SERS measurement set, an apoptosis/necrosis assay and a WST-1 cell proliferation assay was coupled, so that any outlier that could originate from possible experimental variations would be easily pointed out.

TEM and EDF images helped to observe structural aberrations upon exposure to NMs. Moreover, the location and extent of internalization of AuNPs were observed from these images.

4.2.1. Apoptosis/Necrosis Assay

Apoptosis/necrosis rates were obtained from NM-exposed cells that were stained with Annexin V-FITC and PI and analyzed on flow cytometer. The overall results of the four cell lines that were exposed to five NMs were given in Figure 4.2.

ZnO NPs induced apoptosis in all cell lines, especially from above 15 μg/ml ZnO NP concentration. HSF cell line was more prone to apoptosis, whereas L929 cell line showed a resistance to ZnO NP damage until 15 μg/ml ZnO NP concentration.

TiO_2 NPs induced milder cytotoxicity. A549 and HSF cell lines were more resistant to apoptosis compared to HUVEC and L929 cell lines, even though the rate of live cells did not go below 70 per cent in any of the test groups.

The results obtained from SWCNTs, MWCNTs, and QDs were not highly reliable. The instrument counted SWCNTs and MWCNTs themselves as cells in most of the measurements due to agglomerate formation. In some cases, the instrument was clogged because of the clumps. For QDs, the emission wavelength of Annexin V-FITC stain was overlapping with the emission wavelength of QDs (~525 nm), thus the rate of live cells were false positive.

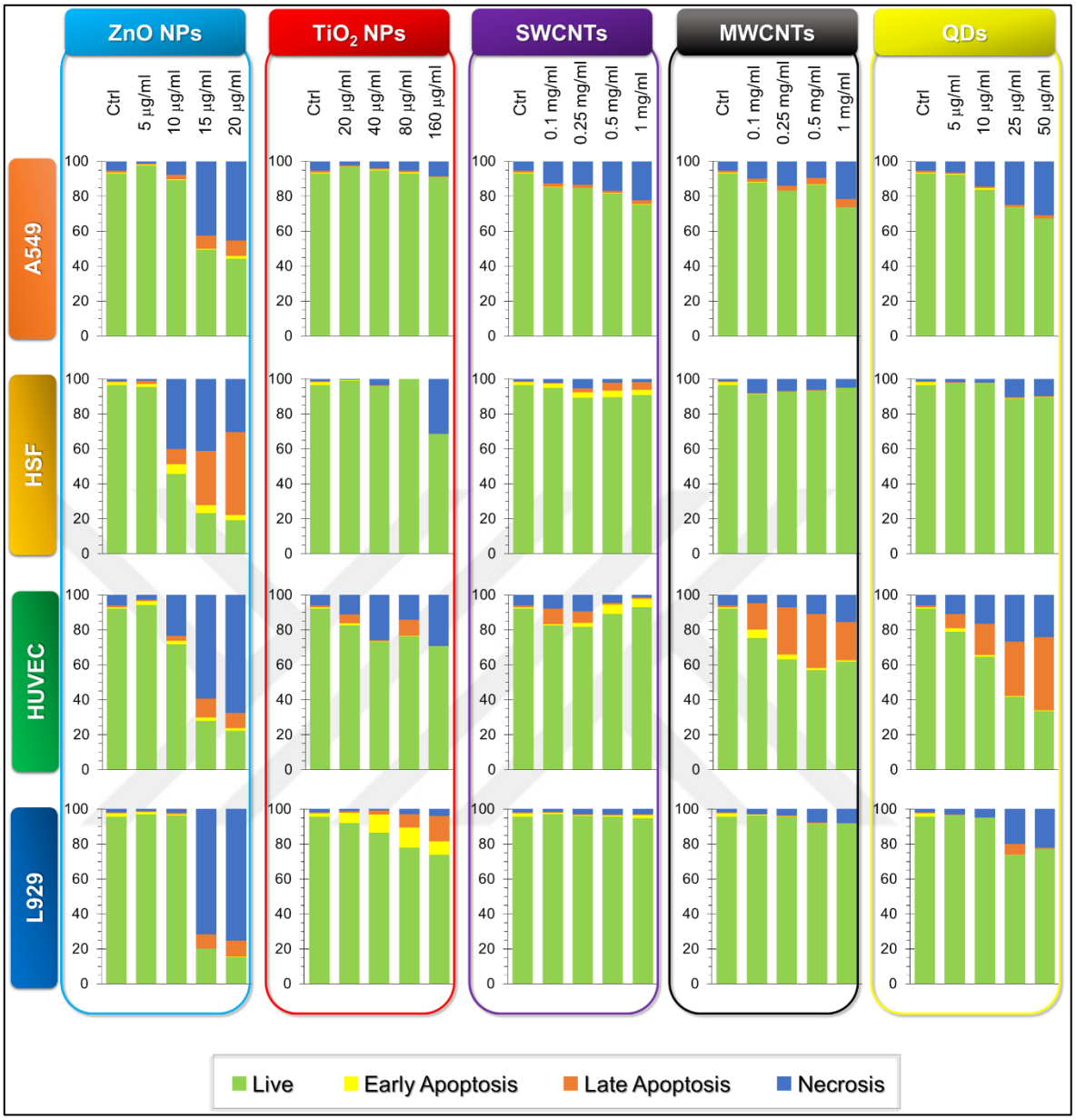

Figure 4.2. Apoptosis/Necrosis assay results. A549, HSF, HUVEC and L929 cell lines were exposed to ZnO NPs, TiO_2 NPs, SWCNTs, MWCNTs and QDs at increasing concentrations.

4.2.2. WST-1 Cell Proliferation Assay

WST-1 cell proliferation assay relies on the colorimetric detection of formazans that were reduced from the water soluble tetrazolium salt, WST-1 (Figure 4.3) [157]. The overall

reaction occurs in the extracellular environment through a couple of redox reactions in the presence of redox mediator mPMS (one of the components of the assay kit) and is mediated by extracellular superoxides [158]. Therefore, superoxide dismutase (SOD) activity significantly affects WST-1 reduction.

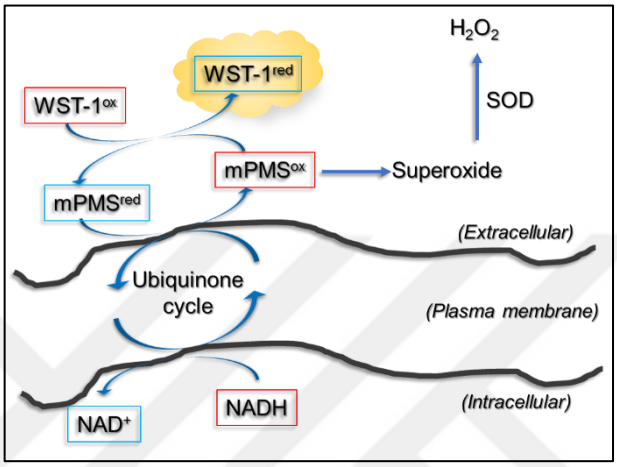

Figure 4.3. Mechanism of WST-1 reduction in te extracellular environment.

In agreement with the apoptosis/necrosis assay results, ZnO NPs caused significant reduction in cell viability but L929 cells were more resistant to damage (Figure 4.4a).

TiO_2 NPs were not observed as cytotoxic (Figure 4.4b). However, the results were not reliable because the viability values were even higher than control samples. A recent study by Masoud *et al*. showed that superoxide anion production is induced by TiO_2 NPs and as mentioned previously, WST-1 is sensitive to superoxide levels in the extracellular environment [159]. Therefore, false positive results were obtained.

SWCNTs were found to be more cytotoxic than MWCNTs and HUVEC cell line stood out as more resistant to cytotoxicity compared to the other three cell lines (Figure 4.4c and d).

QDs were again found to interfere with the assay results (Figure 4.4e). For instance, HSF cell line showed about 150 per cent cell viability regardless of QD concentration which was not confirmed by visual inspection.

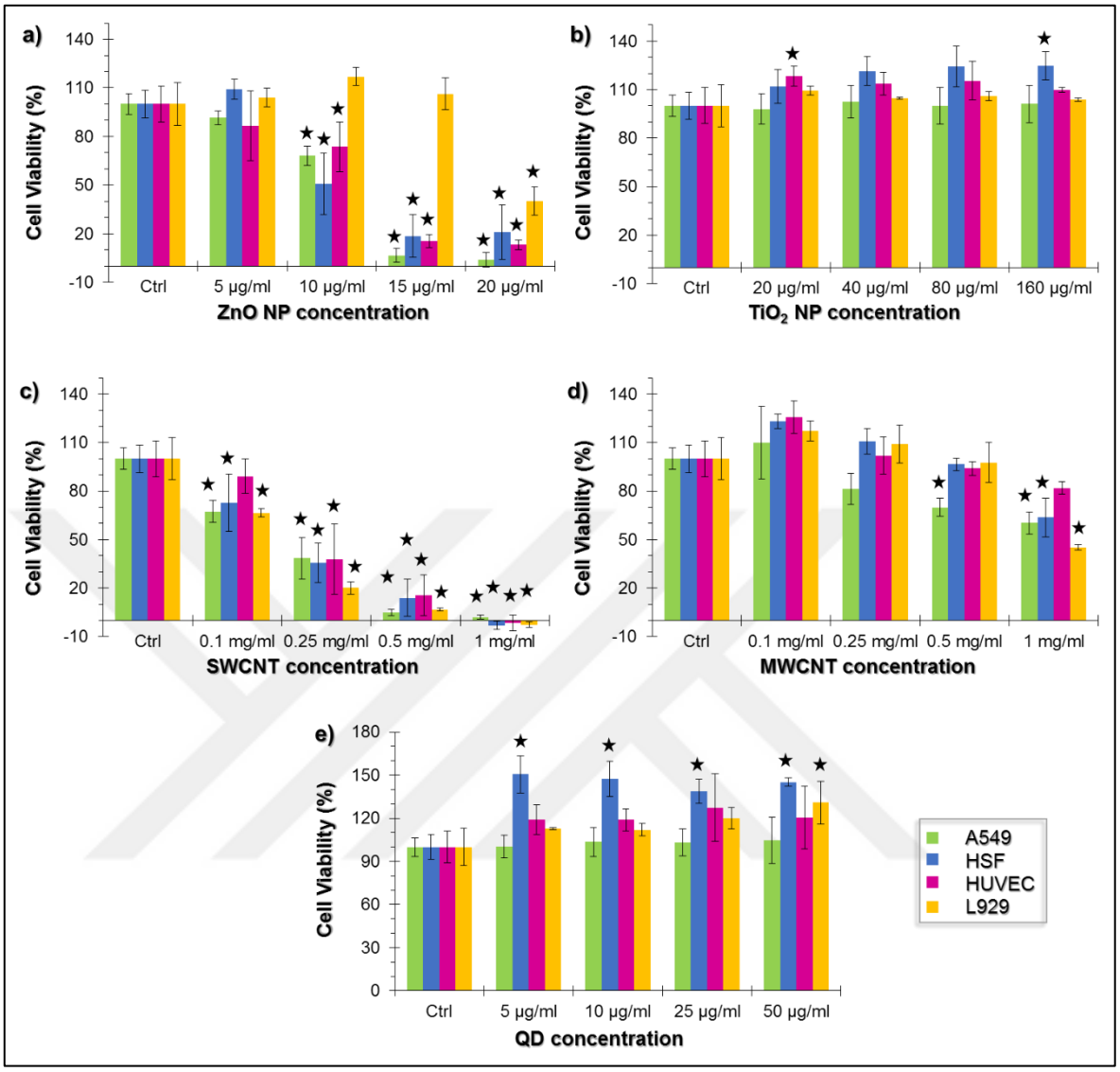

Figure 4.4. WST-1 assay results. **(a)** ZnO NPs, **(b)** TiO_2 NPs, **(c)** SWCNTs, **(d)** MWCNTs and **(e)** QDs were exposed to A549, HSF, HUVEC and L929 cell lines at increasing concentrations. Results were normalized to their only-AuNP-exposed controls, error bars represent ±S.D. and statistically significant changes compared to control samples were marked with a star sign (One-way ANOVA with Tukey's post-hoc test, ($p \leq 0.05$)).

4.2.3. Transmission Electron Microscopy Images

TEM images provide direct visual outcomes of cellular conditions. Despite being a laborious technique, precious information can be gathered from the obtained images. Upon exposure

to NMs structural aberrations and the localization of NMs were observed. Images of the cells that were only incubated with AuNPs showed that the particles were mostly accumulated in the endosomes and lysosomes at large amounts. In the inset of Figure 4.5a, AuNPs in the endocytic vesicles were zoomed in. The more electron-dense lysosomes were seen as darker vesicles.

Exposure to AuNPs and 10 µg/ml ZnO NPs resulted in structural deformations, especially the mitochondria were granulated as a marker of oxidative stress (Figure 4.5b). Large autophagosomes containing AuNPs were also seen. ZnO NPs were not visible in the acquired images. It was previously shown that upon 24 h incubation, most of the ZnO NPs dissolve into Zn^{2+} ions which might be the reason why they were not visible [160].

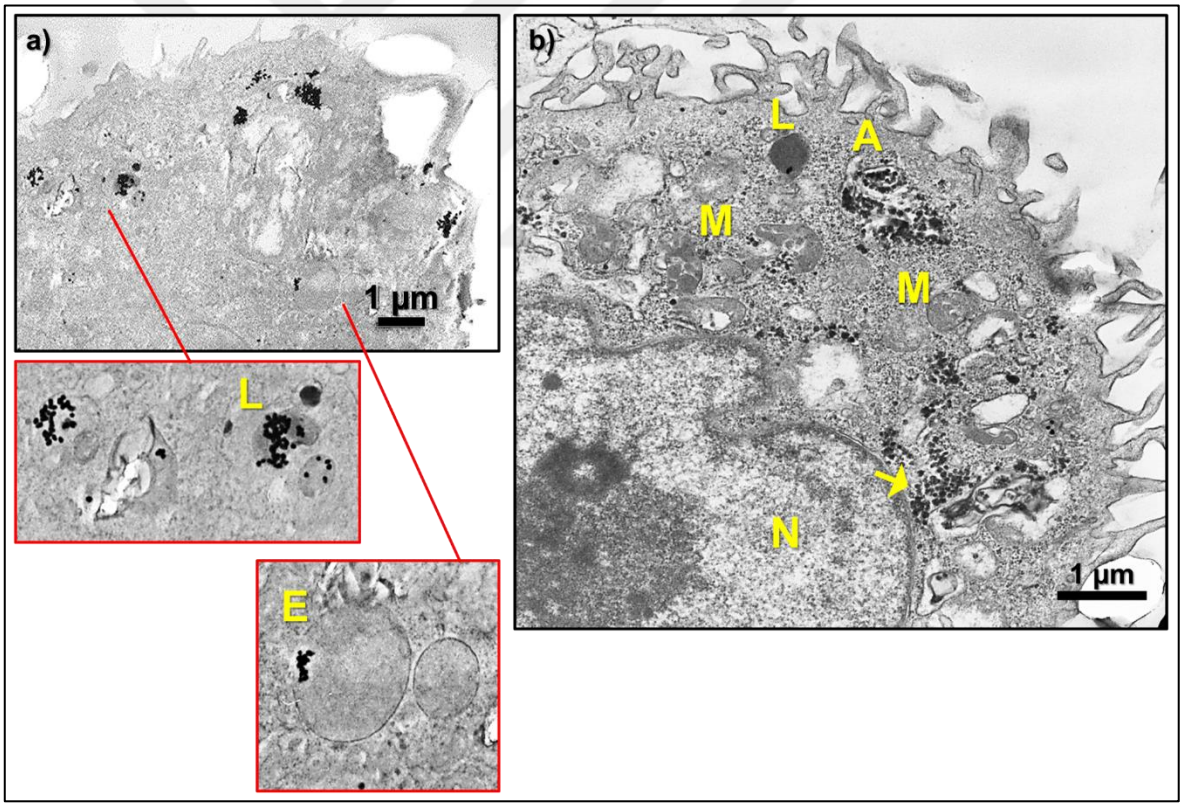

Figure 4.5. TEM image of A549 cells incubated with **(a)** only AuNPs and with **(b)** AuNPs as well as 10 µg/ml ZnO NPs. Yellow arrow points to the AuNPs. Inset figures show AuNPs accumulated in endosomes and lysosomes. (A: autophagosome, E: endosome, L: lysosome, M: mitochondrion, N: nuclues)

TiO_2 NPs were internalized extensively to the cells and accumulated in large quantities. On the other hand, SWCNTs were not visible inside the cells either because of their small diameter (0.7-0.9 nm) or because they were not internalized to a large extent that could be seen. Actually, there are studies that report pristine SWCNTs interact with the plasma membrane and do not prefer to be internalized [161]–[164]. However, cytotoxic effect of SWCNTs on the cells were observed. Apart from the formation of large autophagosomes (Figure 4.6b inset), ER-mitochondria co-localization close to plasma membrane was observed as a marker of oxidative stress [165]. Granulated and elongated mitochondria were other indicators of oxidative stress.

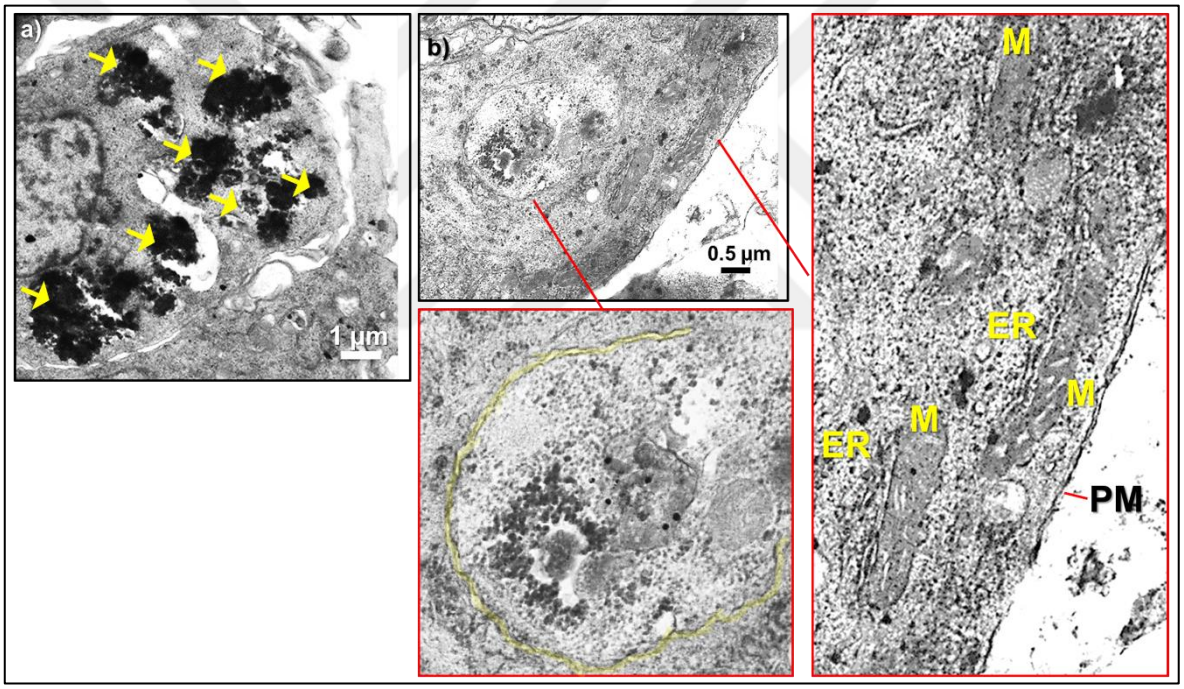

Figure 4.6. TEM image of A549 cells incubated with **(a)** AuNPs and 160 µg/ml TiO_2 NPs Yellow arrows points to accumulated TiO_2 NPs. **(b)** Cells incubated with AuNPs and 0.25 mg/ml SWCNTs. The yellow highlighted line in inset figure is the double membrane formation of an autophagosome. (ER: endoplasmic reticulum, M: mitochondrion, PM: plasma membrane)

Unlike SWCNTs, it was possible to capture MWCNTs in endosomes (Figure 4.7a inset). The structural deformation was not as significant as observed in SWCNTs, indicating a milder cytotoxicity.

Cytotoxicity induced by QDs were successfully observed in TEM images (Figure 4.7b). Exposure to 50 µg/ml QDs caused nuclear condensation and deformation of cell organelles which lead to apoptosis and cell death.

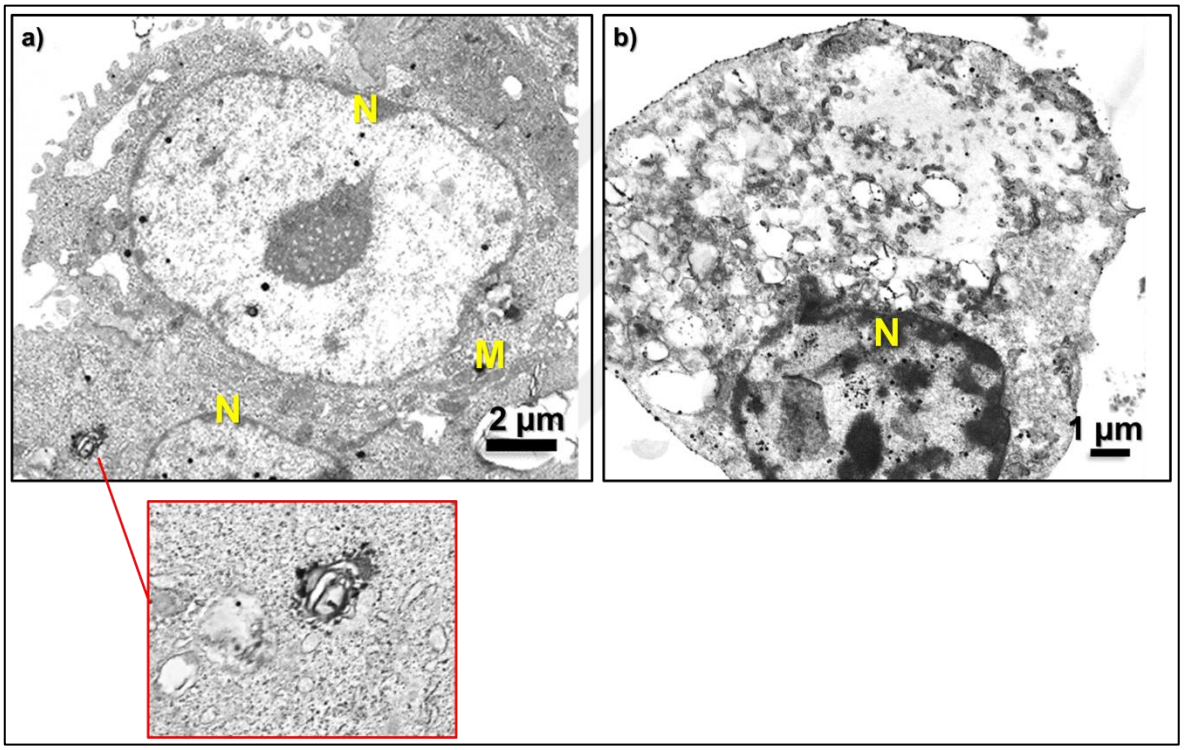

Figure 4.7. TEM image of A549 cells incubated with **(a)** AuNPs and 0.25 mg/ml MWCNTs. Inset figure shows MWCNTs accumulated in an endosome. **(b)** Cells incubated with AuNPs and 50 µg/ml QDs. (M: mitochondrion, N: nucleus)

4.2.4. Enhanced-Dark Field Microscopy Images

EDF microscopy provided an overview of cell-NM interaction. It was possible to visualize NM-accumulation in and around the cells. The extent of AuNP uptake was significant in all cell lines (Figure 4.8).

ZnO NPs at 5 μg/ml concentration were observed as non-cytotoxic in apoptosis/necrosis and WST-1 cell proliferation assays. EDF images were also in agreement with this observation with no visual aberrations in cells or nuclei morphology. As an exception, in HSF cells nuclear swelling was observed together with increased AuNP uptake which increased the possibility of membrane swelling as well (Figure 4.9f).

TiO_2 NPs covered the outer surface of the cells like a sheath, especially in HUVEC and L929 cell lines (Figure 4.10). The situation was similar in SWCNT and MWCNT-exposed cells, SWCNTs being more significantly accumulated (Figure 4.11 and 4.12).

QDs were seen as accumulated clumps, whereas some of them were captured as yellow fluorescent spots (Figure 4.13). The nuclei of the cells were mostly condensed as a marker of apoptosis as was also observed in the TEM image (Figure 7b).

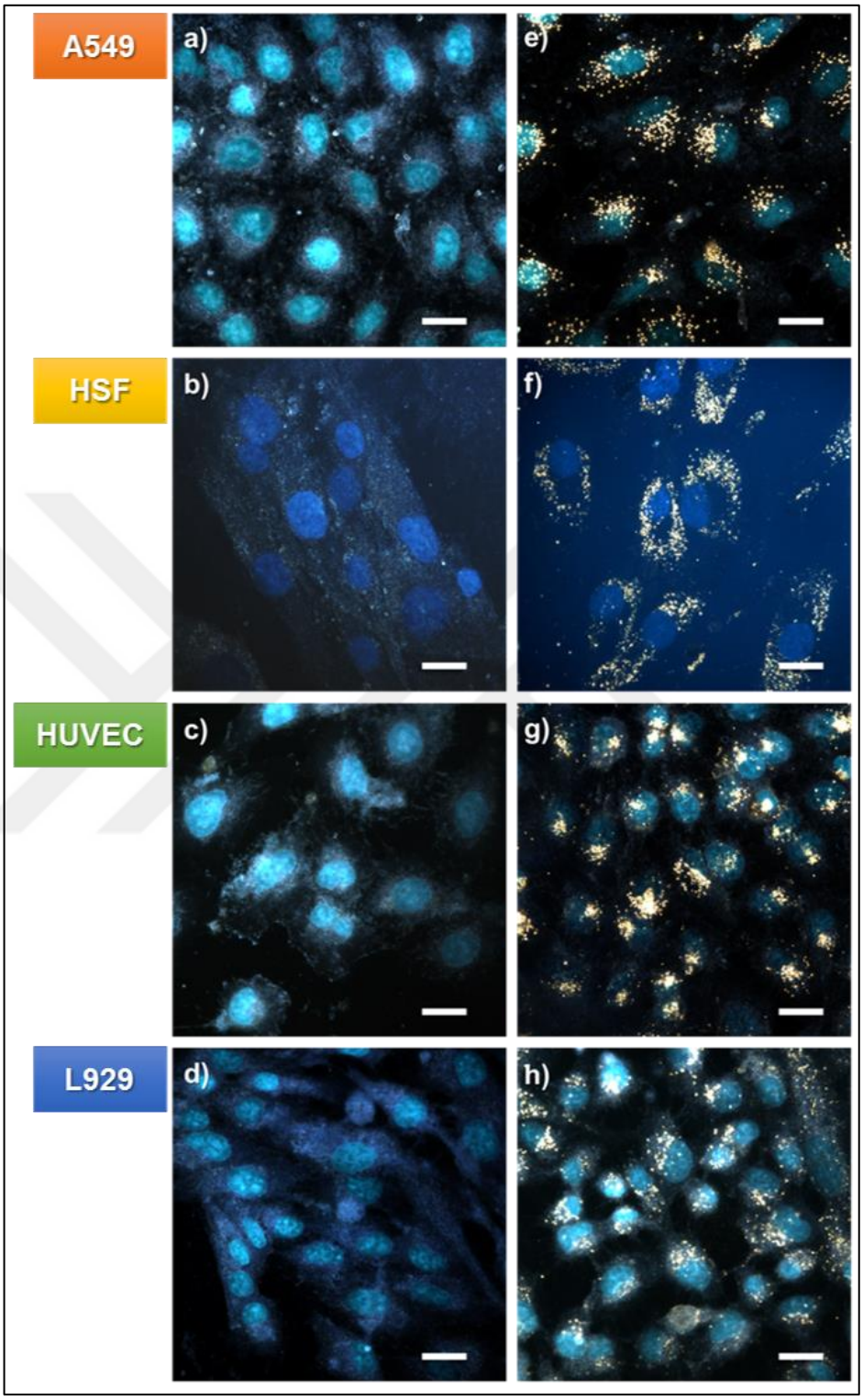

Figure 4.8. EDF images of A549, HSF, HUVEC and L929 cell lines **(a, b, c, d)** without and **(e, f, g, h)** with 24 h AuNP incubation. Cell nuclei were stained with DAPI and false colored to cyan. Scale bars are 20 μm.

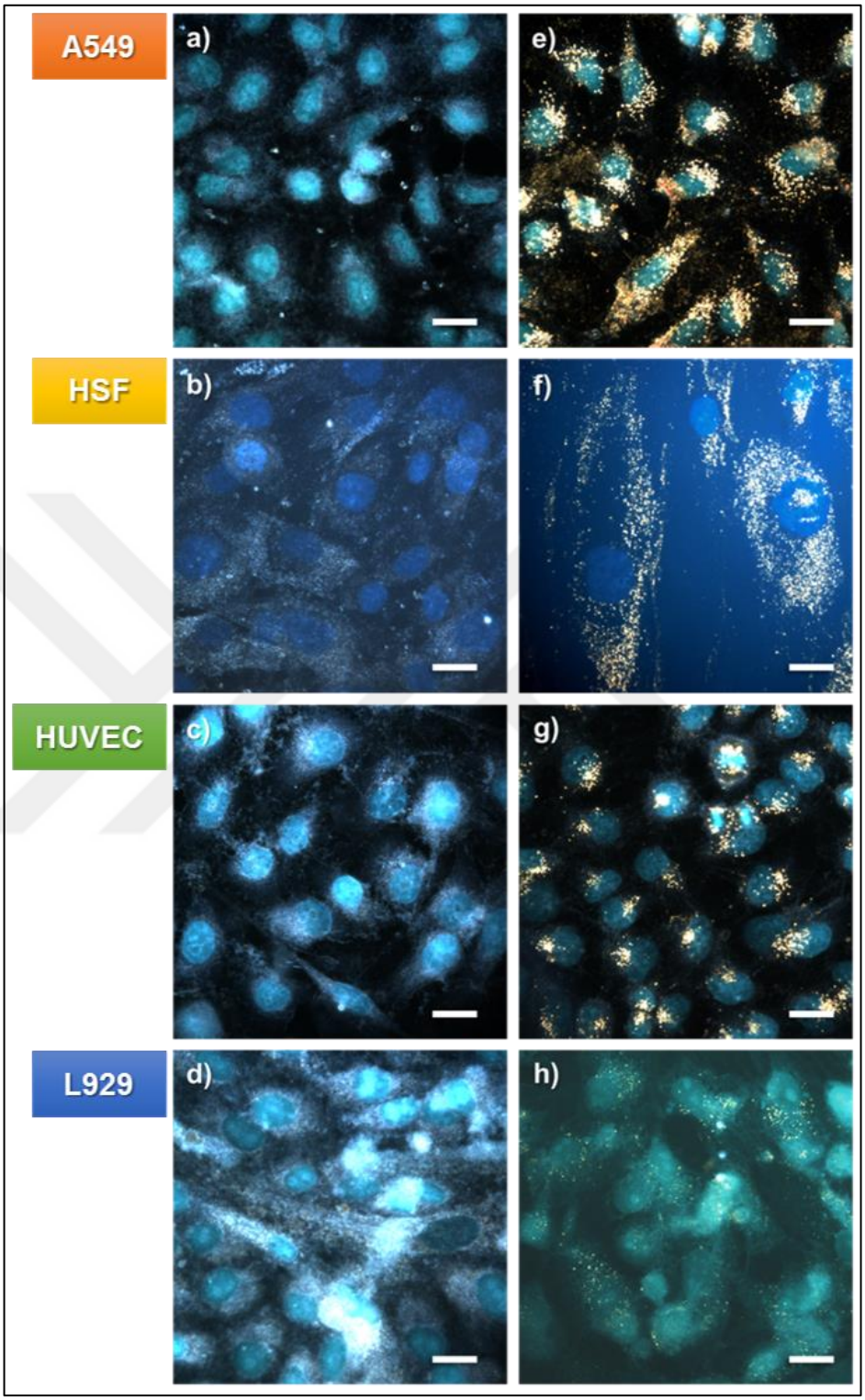

Figure 4.9. EDF images of A549, HSF, HUVEC and L929 cell lines exposed to 5 µg/ml ZnO NPs **(a, b, c, d)** without and **(e, f, g, h)** with 24 h AuNP incubation. Cell nuclei were stained with DAPI and false colored to cyan. Scale bars are 20 µm.

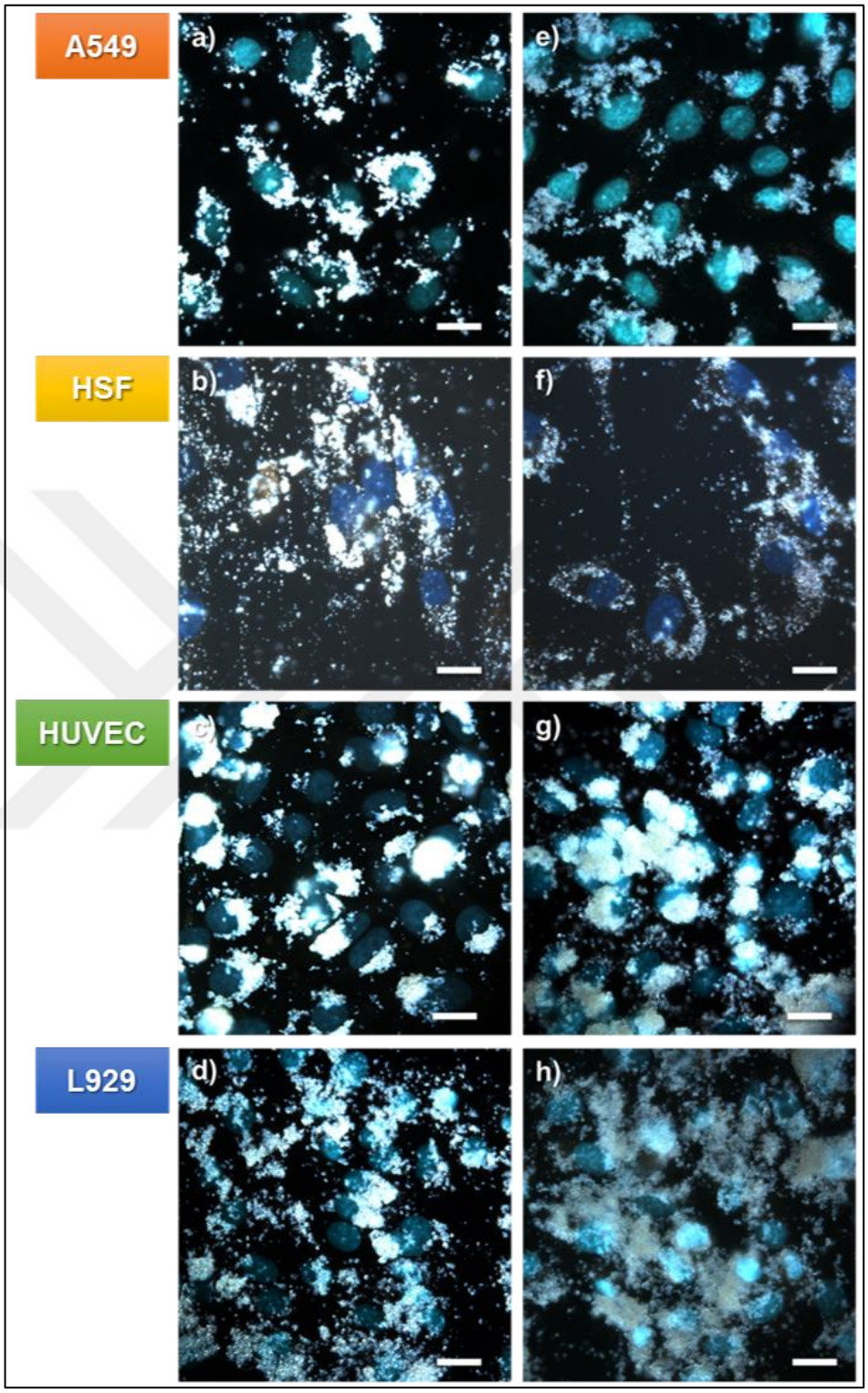

Figure 4.10. EDF images of A549, HSF, HUVEC and L929 cell lines exposed to 40 µg/ml TiO_2 NPs **(a, b, c, d)** without and **(e, f, g, h)** with 24 h AuNP incubation. Cell nuclei were stained with DAPI and false colored to cyan. Scale bars are 20 µm.

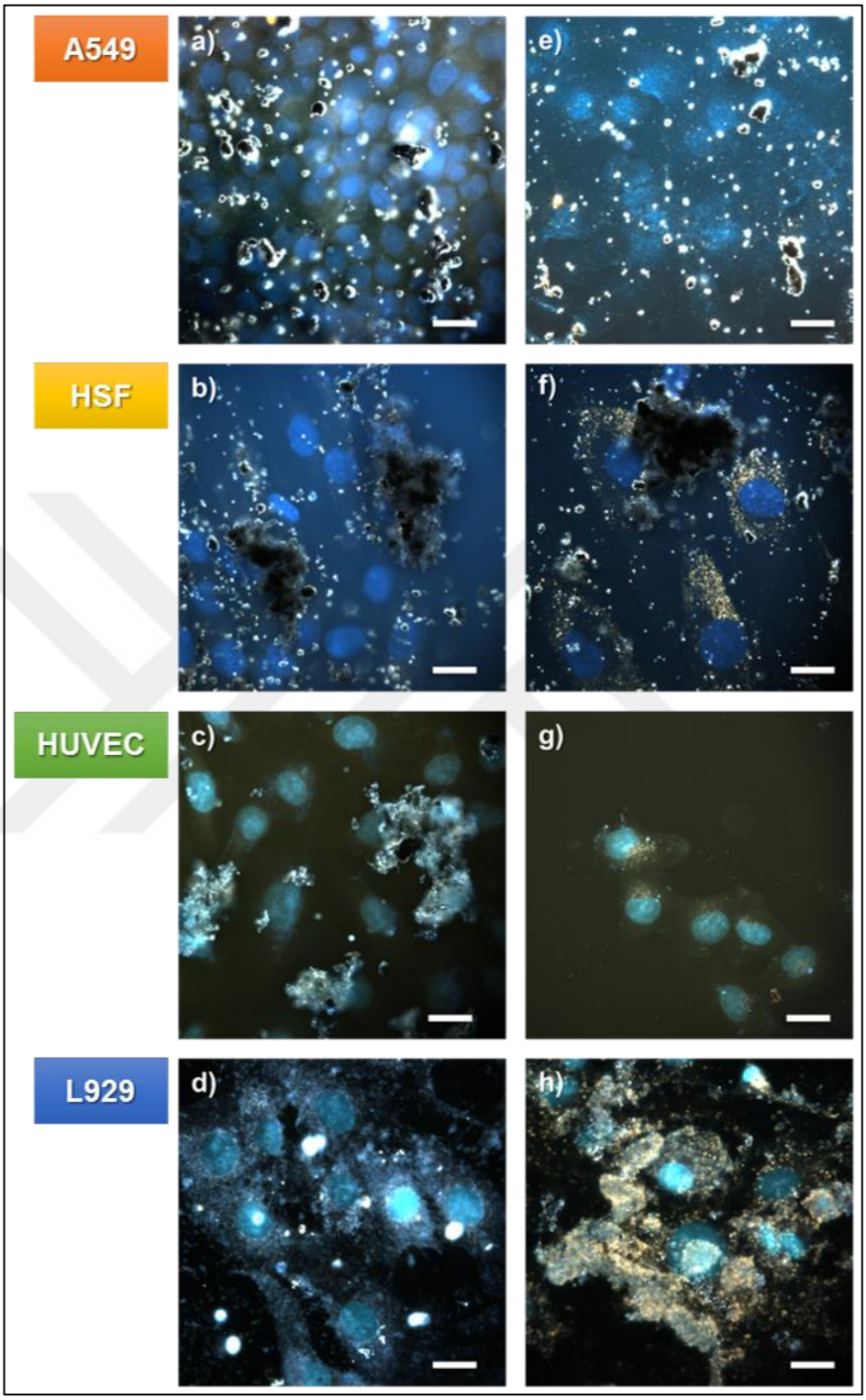

Figure 4.11. EDF images of A549, HSF, HUVEC and L929 cell lines exposed to 0.1 mg/ml SWCNTs **(a, b, c, d)** without and **(e, f, g, h)** with 24 h AuNP incubation. Cell nuclei were stained with DAPI and false colored to cyan. Scale bars are 20 μm.

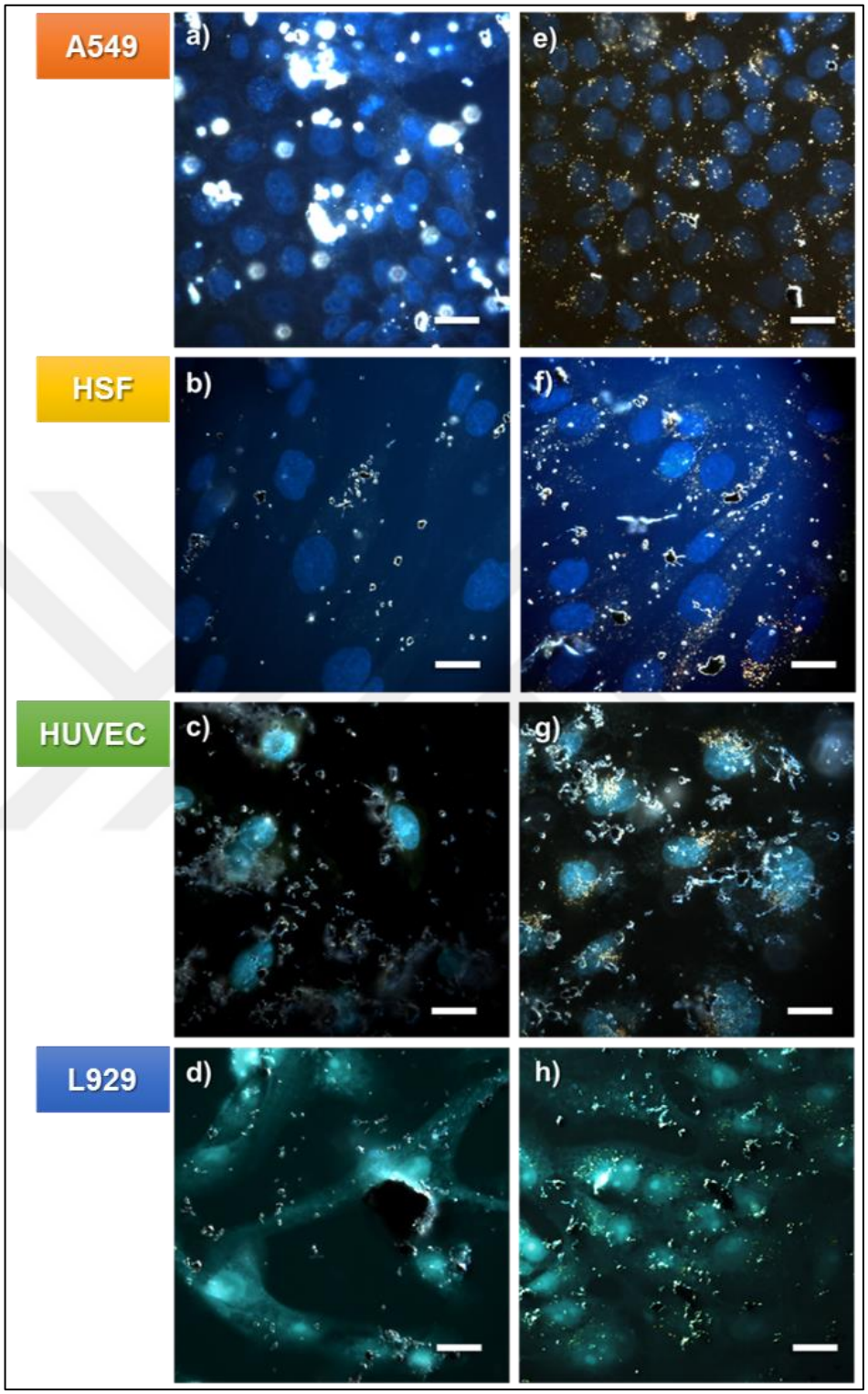

Figure 4.12. EDF images of A549, HSF, HUVEC and L929 cell lines exposed to 0.25 mg/ml MWCNTs **(a, b, c, d)** without and **(e, f, g, h)** with 24 h AuNP incubation. Cell nuclei were stained with DAPI and false colored to cyan. Scale bars are 20 µm

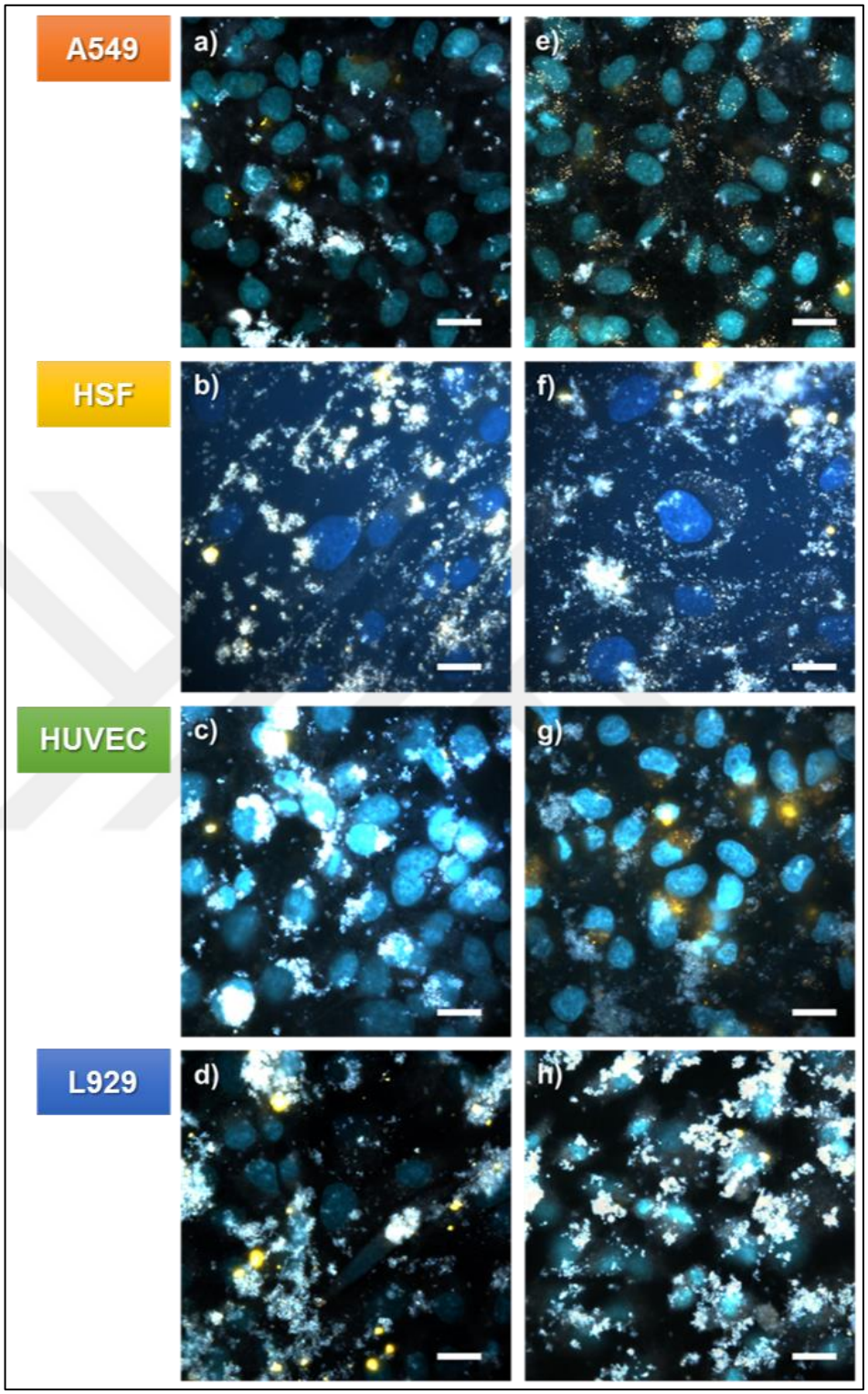

Figure 4.13. EDF images of A549, HSF, HUVEC and L929 cell lines exposed to 25 µg/ml QDs **(a, b, c, d)** without and **(e, f, g, h)** with 24 h AuNP incubation. Cell nuclei were stained with DAPI and false colored to cyan. Scale bars are 20 µm.

4.2.5. Summary of Cytotoxicity Implications

In summary, the conventional cytotoxicity analyses apoptosis/necrosis and WST-1 cell proliferation assays were not fully conclusive for the NMs tested because the presence of NMs were found to manipulate the assay results in most cases. This was an expected outcome considering the literature on the drawbacks of the existing nanotoxicity evaluation approaches. However, it was still possible to extract important implications of cytotoxicity that would be useful in the evaluation of SERS-based results.

First of all, it was seen that AuNPs were efficiently internalized by all cell lines. Particles were mostly seen in the endolysosomal system unless there was a leakage or rupture of these vesicles. Therefore, the SERS spectra would be expected to give information about the changes in these vesicles and their content, which are highly dynamic especially upon cellular stress conditions.

A brief comparison among the cell lines revealed that L929 cell surface tended to adsorb more NMs at the same NM concentration regardless of NM type. However, WST-1 assay results indicated that the cell line was quite resistant to NM toxicity. On the other hand, HSF cell line was more prone to damage upon NM exposure.

A comparison at NM level showed that ZnO NPs were the most nanotoxic among the tested NMs even at lower concentrations. TiO_2 NP nanotoxicity appeared to be ROS-mediated and the extensive uptake of TiO_2 NPs would possibly lead to mechanical stress on the cells. SWCNTs were more nanotoxic than MWCNTs and induced ER-mediated stress, mitochondria granulation and elongation. QDs induced apoptosis especially at higher concentrations.

The reports where same type of NMs of similar size range were tested for their nanotoxicity in the literature were in agreement with the above findings [24], [39], [166], [167].

4.3. METHOD OPTIMIZATION FOR LIVING-CELL SERS MEASUREMENTS

Before moving on to nanotoxicity evaluation, several parameters were to be optimized for SERS measurements. For instance, the extent of AuNP accumulation in cells at various time points were investigated. An important point to consider was the evaluation of spectral

contributors to living-cell SERS. A clear understanding should be established on the contributors to come to healthy conclusions on the SERS spectral patterns upon NM exposure. Apart from these, AuNP concentration to be used, and instrument settings such as microscope objective, laser power, and focus adjustment were optimized to obtain high signal intensity whereas to limit additional cytotoxicity that could be introduced to the cells. The effect of the size of the sampling space was also discussed.

4.3.1. Intracellular AuNP Localization

In "Section 4.2.3." and Figure 4.5a, AuNPs were shown to accumulate in the endolysosomal compartments. The extent of AuNP accumulation through time was also evaluated and correlated to the SERS spectra obtained at these time points (Figure 4.14). In a short time incubation such as 15 minutes, AuNP accumulation was not visible to eye and SERS spectrum was the same as blank, thus excluded. Upon six hour incubation, surface of cells were mostly covered with AuNPs and the amount of AuNPs were more than the amount observed at 24 hour. However, SERS signal intensity was higher at 24 h (Figure 4.14e). In the six hour samples, playing with the microscope focus showed that AuNPs were located more on the upper parts of the cells, which could also be observed in Figure 4.14c where AuNPs looked blurry when focus was adjusted on cell nuclei. On the other hand, in 24 hour samples, the AuNPs looked more clearly and at the same plane with cell nuclei. Therefore, it was concluded that AuNP uptake was in its later stages at 24 hour, thus the particles were localized inside cells in larger aggregates. In the cells incubated with AuNPs for six hours, the aggregation was less prominent thus they looked more blurry and dispersed on the cells. Although the normalized SERS spectra carried the same pattern in both time points, 24 hour AuNP incubation was chosen for ease of operation during NM exposure studies.

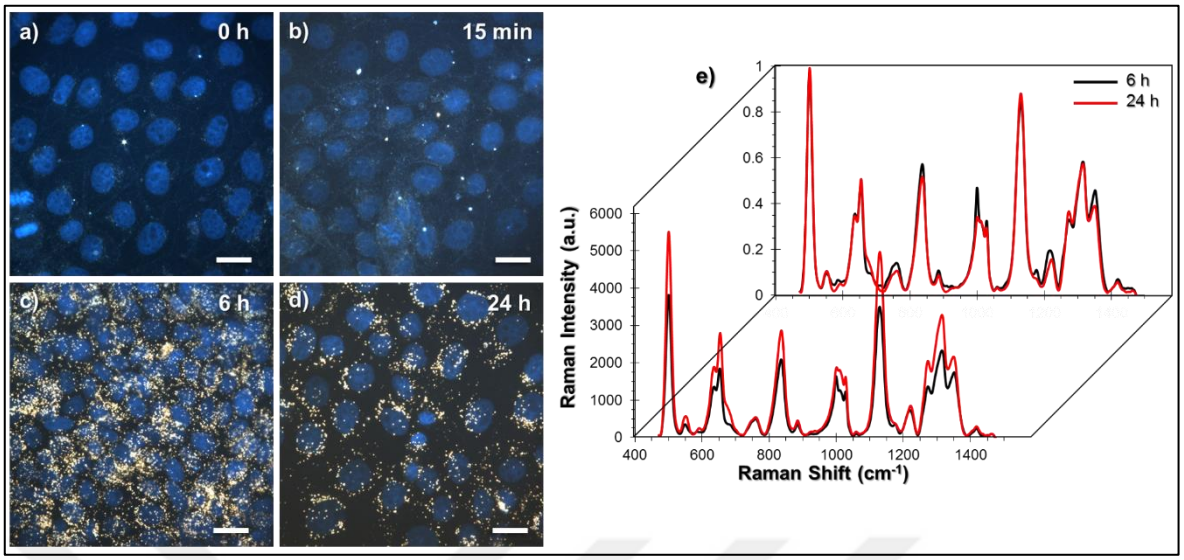

Figure 4.14. AuNP accumulation in A549 cell line at **(a)** 0h, **(b)** 15 minutes, **(c)** 6 h and **(d)** 24 h. Scale bars are 20 µm. **(e)** Overlapped SERS spectra obtained after incubation with AuNPs for 6 h and 24 h. The above spectra are the same spectra after normalization.

4.3.2. The Spectral Contributors to Living-Cell SERS

In a chaotic environment like cell, there is a prior question to be answered; that is "*What are the spectral contributors to the average spectrum?*". At this stage, the biological corona around the SERS substrate that is formed right after the first interaction into the incubation medium containing molecules such as proteins, lipids, carbohydrates plays a vital role. This is because the SERS effect occurs in a few nanometer scale (about one to five nm) from the substrate surface at furthest [113]. Therefore, the corona and its dynamics are highly important in data interpretation. In an attempt to enlighten the subject "*To what extent the SERS spectra are affected from the changes on corona?*", two approaches were applied. A cell-free approach where external stimuli were tested on corona-formed AuNPs, and a cell-related approach where the living cell spectrum was compared to the cell-free and ruptured-cell spectra.

First of all, as-synthesized AuNPs (referred as "bare" in Figure 4.15) were observed to have about 10 nm increase in their hydrodynamic diameter, meaning a corona layer of five nm thickness was around them.

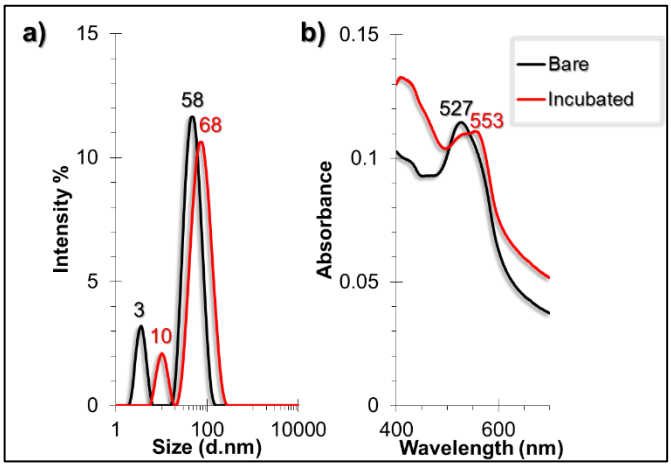

Figure 4.15. Protein corona characterization results. **(a)** DLS and **(b)** UV-Vis plots of bare AuNPs as control and AuNPs incubated with cell culture medium.

Heating the corona to 42°C led to loosening of the proteins and an enlargement of hydrodynamic diameter, whereas at 55°C loss of corona due to detached corona content was observed (Figure 4.16a). At 72°C, however, an increase in diameter was again observed probably due to aggregation of AuNPs upon heating which was also observed as a redshift in UV-Vis spectra (Figure 4.16b). The redshift was not thought to be due to corona thickening because the UV-Vis spectrum of 55°C-heated sample also showed a redshift, meaning a gradual aggregation occurred which was also visible from the AuNP pellets in test tubes; at the higher temperatures there were precipitates of AuNPs at the bottom of the tubes. These changes were traced in SERS spectra as changes in α-helix content (1284 cm^{-1}), lipid deformation vibrations (1437 cm^{-1}), and C=C stretching vibrations (1583 cm^{-1}) (Figure 4.16c). At 42°C, C=C stretching vibrations were higher compared to control, whereas with the increasing temperature, thus loosening of proteins from the AuNP surface, led to a gradual decrease of this peak. Similarly, depletion of α-helix content and lipid deformation were increased especially at 72°C.

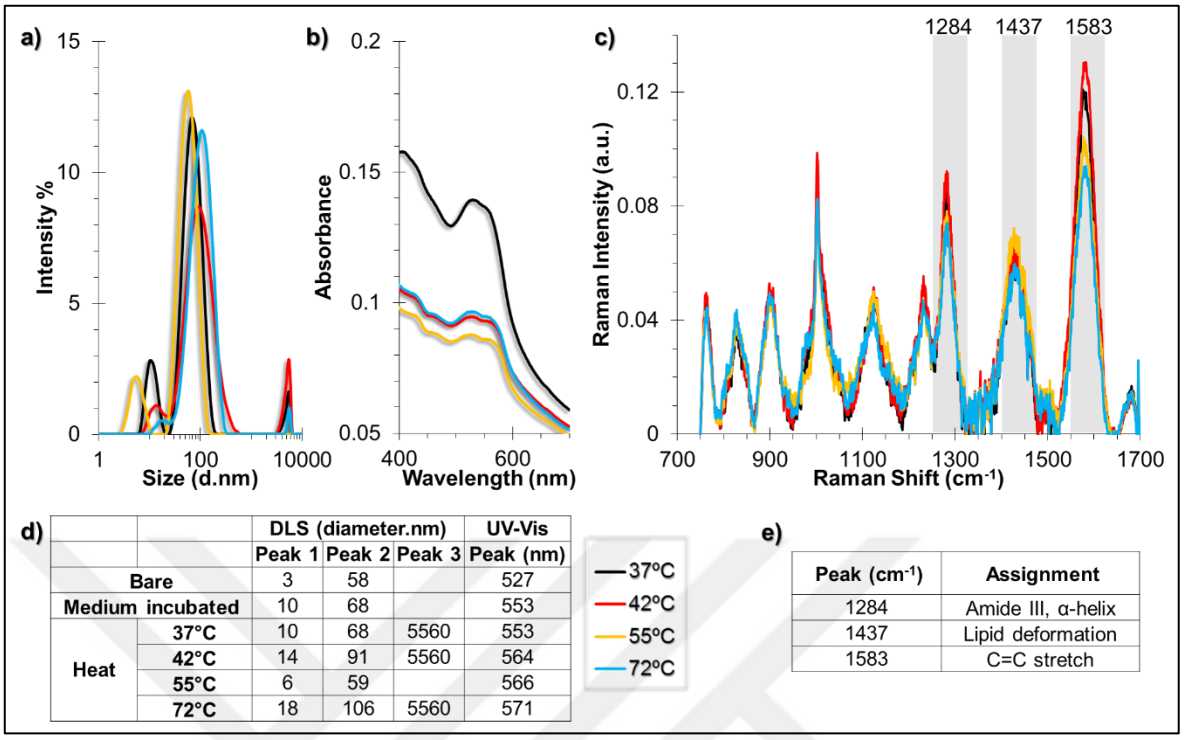

d)

		DLS (diameter.nm)			UV-Vis
		Peak 1	Peak 2	Peak 3	Peak (nm)
Bare		3	58		527
Medium incubated		10	68		553
Heat	37°C	10	68	5560	553
	42°C	14	91	5560	564
	55°C	6	59		566
	72°C	18	106	5560	571

e)

Peak (cm^{-1})	Assignment
1284	Amide III, α-helix
1437	Lipid deformation
1583	C=C stretch

Figure 4.16. Protein corona characterization results. **(a)** DLS **(b)** UV-Vis and **(c)** SERS spectra of medium-incubated AuNPs treated with increasing temperature. **(d)** Peak positions for each sample were summarized in the table. **(e)** Assignments of the most prominently changed SERS peaks.

Incubation with the protein digesting enzyme, trypsin, caused a gradual breakdown of corona and aggregation of AuNPs at the highest tested concentration (Figure 4.17a). This was traced from the UV-Vis spectra as peak broadening and redshift from 553 nm up to 574 nm (Figure 4.17b). In the SERS spectra, the pattern change was more evident compared to heated samples. Up to 250 µg/ml trypsin concentration, C=C stretching vibrations increased which can be attributed to increased number of peptide fragments upon trypsin activity. At 2500 µg/ml, the enzyme activity led to loss of protein corona, thus a sudden decrease in this peak was observed together with a decrease in 1284 cm^{-1} α-helix peak.

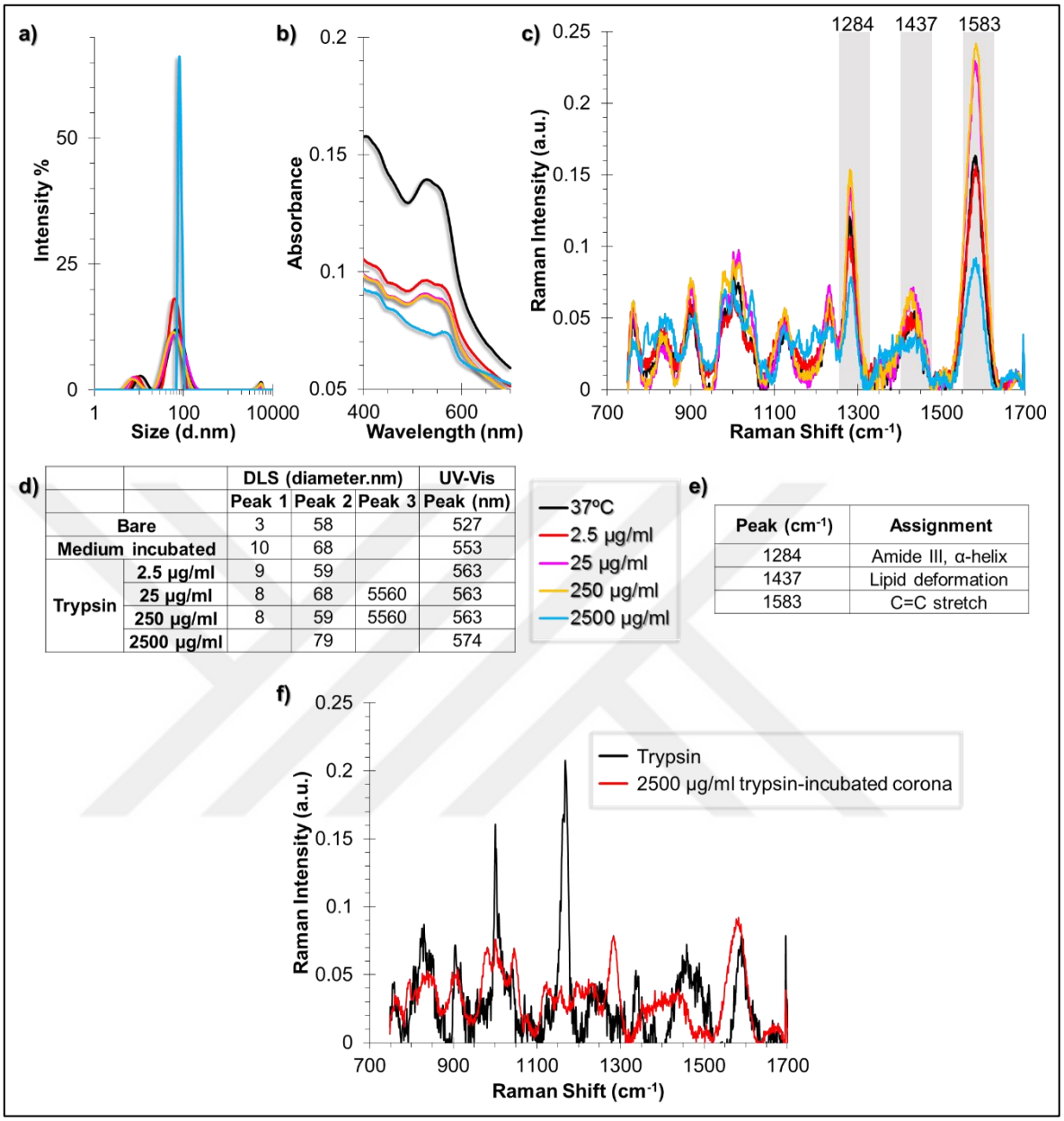

Figure 4.17. Protein corona characterization results. **(a)** DLS **(b)** UV-Vis and **(c)** SERS spectra of medium-incubated AuNPs treated with increasing concentrations of trypsin. **(d)** Peak positions for each sample were summarized in the table. **(e)** Assignments of the most prominently changed SERS peaks. **(f)** Trypsin SERS spectrum compared to spectrum of 2500 µg/ml trypsin incubated corona.

Testing H_2O_2, a member of ROS family, on corona was of interest because most of the NMs exert nanotoxicity via ROS-dependent mechanisms as mentioned previously. Increasing concentration of H_2O_2 caused a dramatic loss of corona leading to the precipitation and

sticking of the AuNPs to the tubes in high amounts. This was especially evident at 180 µM H_2O_2 concentration (Figure 4.18a and b). Moreover, the SERS spectral pattern was significantly affected from the exposure (Figure 4.18c). Different from the two previous stimuli, heating and trypsinization, phenylalanine (Phe) peaks were affected from H_2O_2 exposure. It has been shown that 1030/1000 cm^{-1} peak ratio is sensitive to oxidative environment and increases upon exposure to free radicals [168]. Furthermore, lipid deformation was much more evident, indicating the lipid components of the corona were oxidized when contacted with H_2O_2.

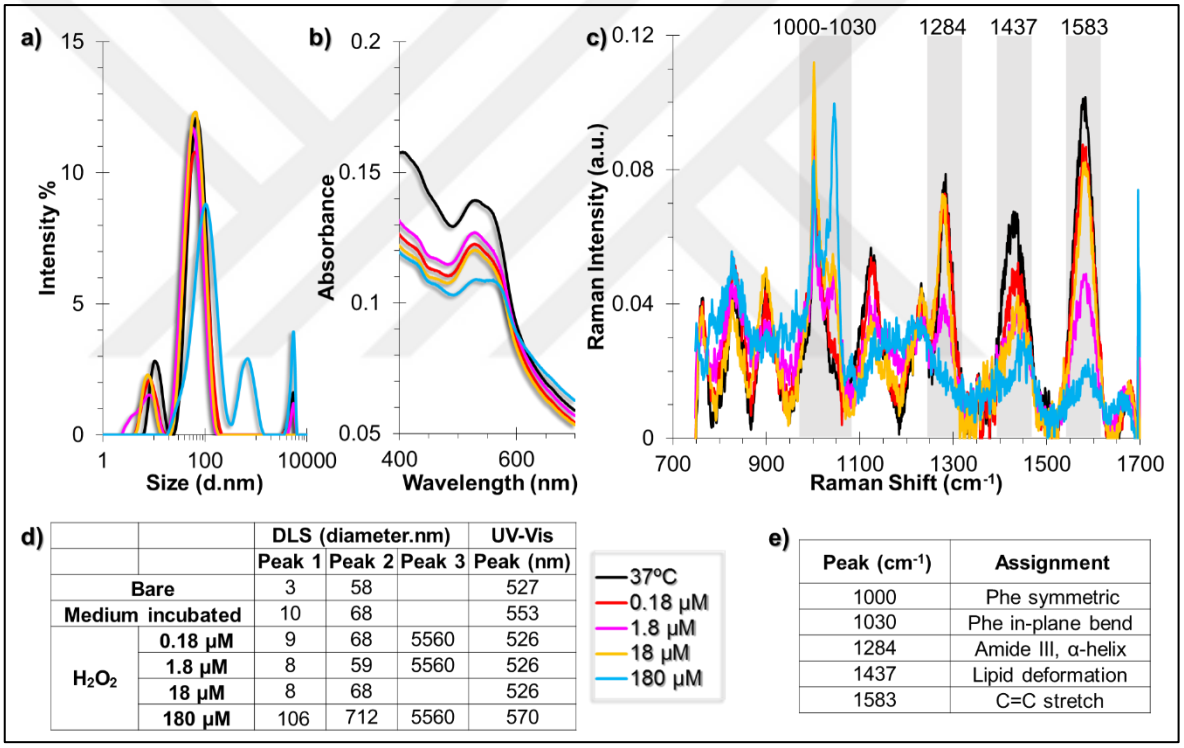

d)

		DLS (diameter.nm)			UV-Vis
		Peak 1	Peak 2	Peak 3	Peak (nm)
Bare		3	58		527
Medium incubated		10	68		553
H_2O_2	0.18 µM	9	68	5560	526
	1.8 µM	8	59	5560	526
	18 µM	8	68		526
	180 µM	106	712	5560	570

e)

Peak (cm^{-1})	Assignment
1000	Phe symmetric
1030	Phe in-plane bend
1284	Amide III, α-helix
1437	Lipid deformation
1583	C=C stretch

Figure 4.18. Protein corona characterization results. **(a)** DLS **(b)** UV-Vis and **(c)** SERS spectra of medium-incubated AuNPs treated with increasing concentrations of H_2O_2. **(d)** Peak positions for each sample were summarized in the table. **(e)** Assignments of the most prominently changed SERS peaks.

These findings confirmed that corona on AuNPs were highly affected from external stimuli and the effects could successfully be traced on SERS spectra. Taking a step further, the average spectrum obtained from living cells were compared to cell-free, medium-incubated

AuNP spectrum and the spectrum obtained from ruptured cells (Figure 4.19). To rupture the cells, ultrasonication was applied and cellular compartments were all ruptured. Therefore, the nuclear content as well as the plasma membrane were all in the same mixture with AuNPs which led to increase in nucleotide and lipid-related peaks. Combining the ruptured cell spectra to cell-free corona spectrum, a spectrum very similar to living-cells was obtained, only except the presence of excess nucleotide and lipid contents.

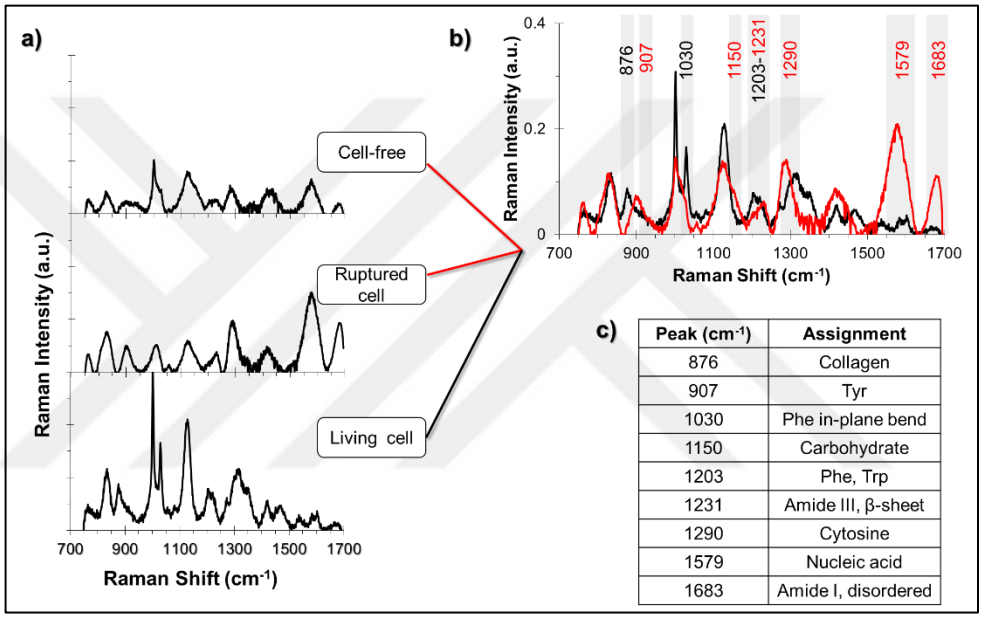

Peak (cm^{-1})	Assignment
876	Collagen
907	Tyr
1030	Phe in-plane bend
1150	Carbohydrate
1203	Phe, Trp
1231	Amide III, β-sheet
1290	Cytosine
1579	Nucleic acid
1683	Amide I, disordered

Figure 4.19. **(a)** Average SERS spectra obtained from cell-free protein corona, ruptured cell and living cell. **(b)** The average spectrum of living cell (black spectrum) overlapped with the summed spectrum of cell-free protein corona, and ruptured cell average spectra (red spectrum). **(c)** The assignment list of peaks highlihgted with gray in **(b)**.

In conclusion, the corona content was found to evolve upon stimulation which could also be traced on SERS spectra. The information obtained from these experiments was the starting point of SERS spectral interpretation in the coming sections.

4.3.3. Experimental Optimization

4.3.3.1. SERS Substrate Concentration

It is important to minimize any possible contribution from AuNPs to nanotoxicity while utilizing AuNPs for SERS experiments. Thus, the concentration of AuNPs in the exposure medium was adjusted. Although the approximate number of particles were provided in "Section 3.6.", for ease of explanation the final amount of AuNPs in the incubation medium will be referred to the final amount of $HAuCl_4$ taken from the initial $HAuCl_4$ in AuNP synthesis, which was 0.01 grams in 100 ml.

First, cells were incubated with 50 μg/ml AuNPs, which corresponded to half of the incubation medium volume (1/2, v/v), whereas the other half contained complete cell culture medium. Then 37.5 μg/ml (3/8, v/v) and 25 μg/ml (1/4, v/v) AuNP concentrations were tested. The spectral pattern as well as the signal intensity were almost the same for all groups (Figure 4.20). Therefore, to avoid any possible additional stress on the cells, 25 μg/ml concentration was chosen as optimal. Lower concentrations were also tested. However, the signal was noisy, thus the results were excluded.

Incubating the cells for 48 hours resulted in reduction of signal intensity which was expected due to cell doubling [169]. After cell division, the amount of internalized AuNPs were diluted. However, the spectral pattern was still consistent with the other spectra. The chosen AuNP concentration was also tested for its toxicity by WST-1 assay. There was not any significant cell viability change.

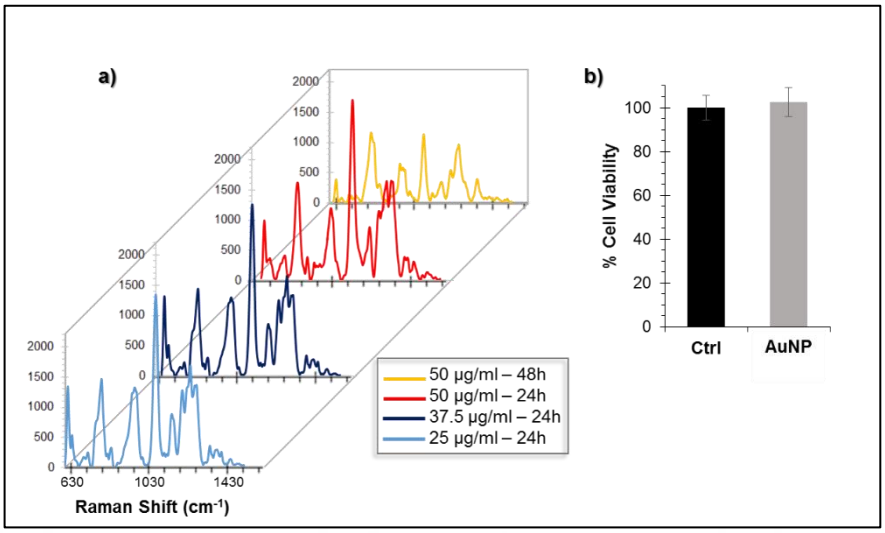

Figure 4.20. **(a)** SERS signal intensities of AuNPs at increasing concentrations and incubation duration. **(b)** Cell viability upon 24 h incubation with 25 µg/ml AuNPs. Error bars were calculated from three independent experiments and plotted as per cent S.D.

4.3.3.2. Objective, Laser Power and Focus Adjustment

Using higher magnification objectives with higher numerical aperture (N.A.) provides higher spatial resolution. However, working with living cells makes it laborious to adjust the proper settings for each sample. Therefore, both 50 × and 20× objectives were tested for SERS measurements. Although the signal intensity was about 10 times higher in measurements carried out with a 50× objective, after spectra normalization the spectral patterns were the same with the ones obtained with a 20× objective (Figure 4.21a). Therefore, 20× objective was chosen for further studies.

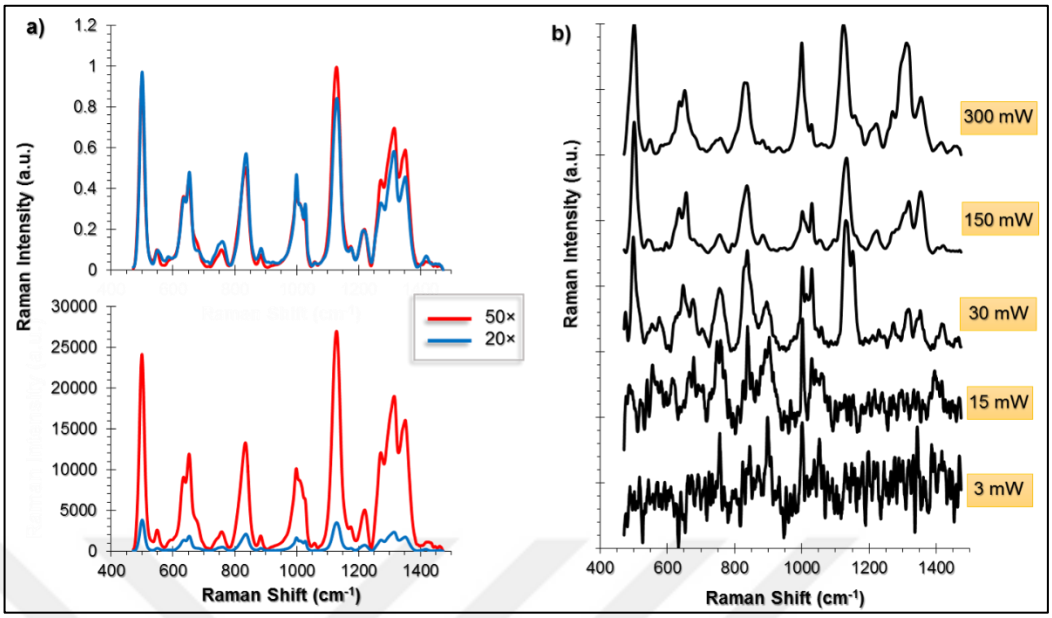

Figure 4.21. Selection of **(a)** microscope objective and **(b)** laser power for SERS measurements. The above spectra in **(a)** are the same spectra after normalization.

A near-IR laser (830 nm) was used in the experiments in the present work. Although a near-IR laser is less harmful compared to a laser in the visible wavelength region, it can still induce damage if the laser power (L.P.) is not chosen properly. Because a long-distance objective was used and the samples were in liquid to prevent drying during measurements, low laser powers such as 15 mW were not enough to obtain satisfactory signal intensity. In Figure 4.21b, spectra obtained at various laser powers at two seconds laser exposure time were plotted. Although at 30 mW L.P. the spectral intensity looked satisfactory, it was not always possible to obtain meaningful SERS spectra from each sample. Therefore, 150 mW L.P. was chosen. At 300 mW L.P., it was observed in some samples that the laser-exposed areas on cells were burnt during analyses, thus 300 mW was not chosen.

One other issue was the adjustment of focus for the SERS measurements. It is known that culturing cells in a two dimensional cell culture affects the localization of organelles and vesicles due to gravity [170], [171]. Upon exposure to AuNPs, the vesicles containing AuNP agglomerates are also expected to localize near the culture vessel surface. In Figure 4.22, the focus adjustment that was used in the experiments were labelled as “0 µm”. with an increment of 1 µm, 5 µm above (-5 to -1 µm) and below (1 to 5 µm) this Z-stack were

scanned. It was observed that the spectral pattern was more reproducible in the deeper parts of the cell. Thus, the focus was always kept at this region for SERS measurements.

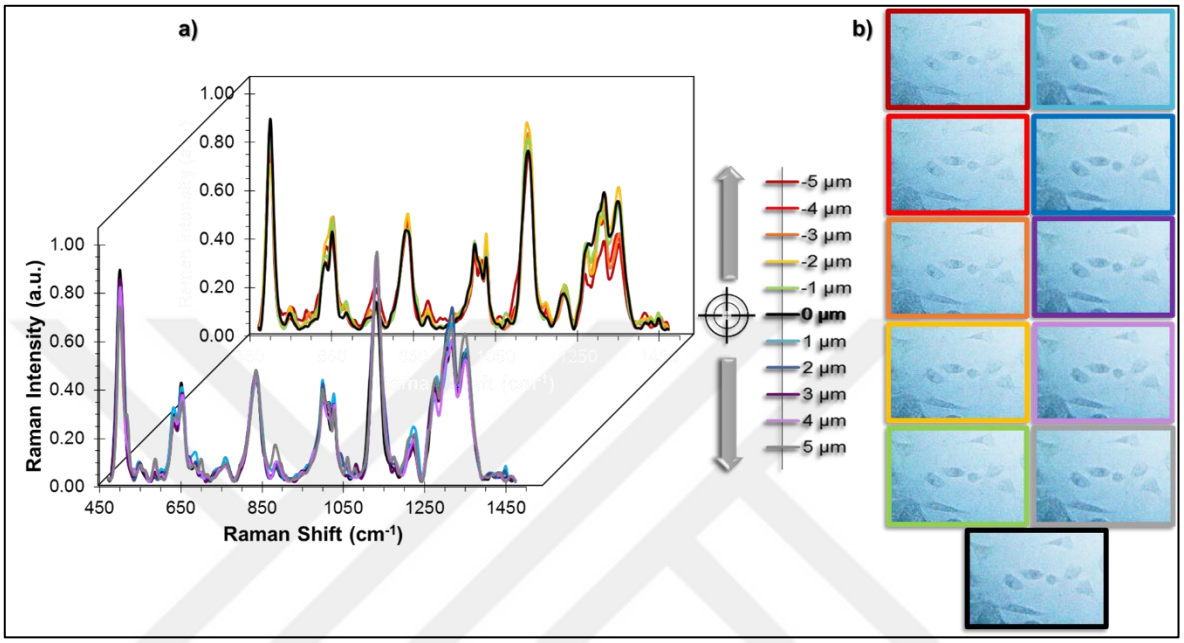

Figure 4.22. **(a)** SERS spectral pattern of the same area at various focus adjustment from -5 µm to 5 µm. The color code shows the respective Z-stacks. **(b)** Light microscope images of the spectra obtained from Z-stacks.

4.3.4. Variations Originating from the Size of the Sample Space

Eukaryotic cells consist of diverse compartments made of complex biomolecules, which creates heterogeneity within cells (Figure 4.23). This can be both a strength and a limiting factor for cellular SERS analyses. Because SERS can provide label-free detection, it is possible to extract multi-dimensional information about the cellular conditions in a simple setting with proper experimental setup. For instance, unlike many typical cytotoxicity assays where only one-dimension of cytotoxicity, such as lipid peroxidation status, can be detected, it is possible to obtain information about lipid, protein or nucleic acid-related conditions all at the same time by utilizing SERS.

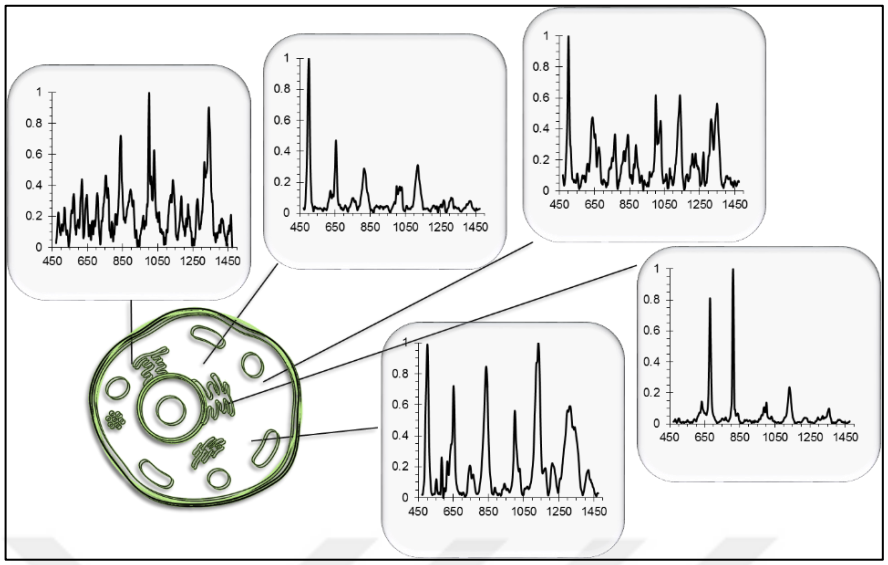

Figure 4.23. Example to spectral variations within a cell.

On the other hand, the heterogeneity can be a limiting factor because the reproducibility of the results are not guaranteed, knowing that SERS signals come from the close vicinity of accumulated AuNPs in various parts of the cell [172]. The heterogeneity issue is not limited to intracellular dynamics. In a population of cells, there are dividing, growing or dying cells, simultaneously. Thus, proper sampling is a crucial step in cellular SERS analysis to improve the reproducibility of the results. As a rule of statistics, a minimum of 20 cases are necessary to form a normally distributed population, whereas 30 cases would be desired. To demonstrate this, in Figure 4.24, average spectrum of 50 cells was compared to average of one, two, five, ten, and twenty cells randomly selected from the 50-cell population. With the increasing number of cases, above 10, the average spectra started to look alike. Therefore, a minimum of 50 cells were scanned for each test group throughout SERS experiments.

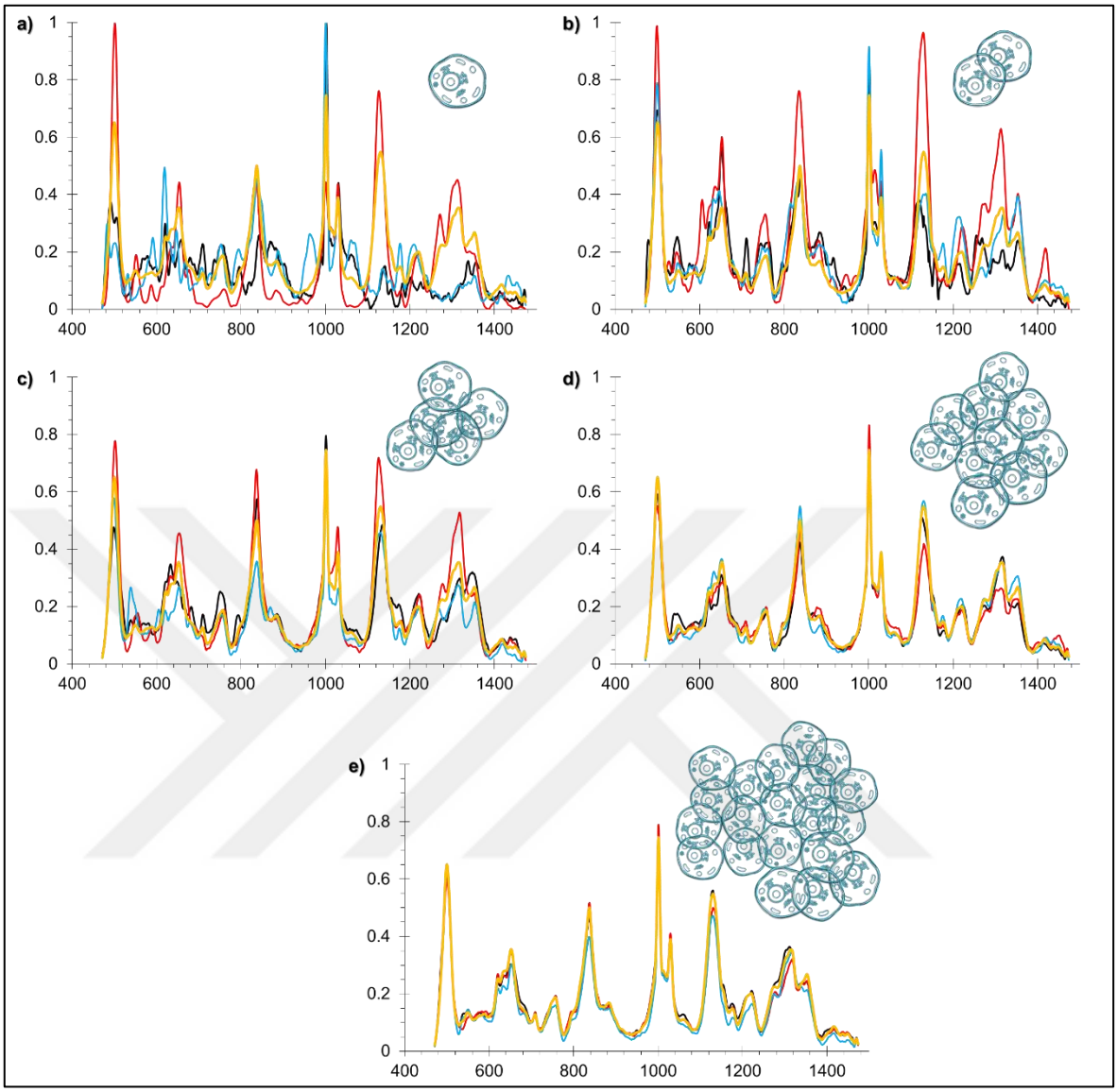

Figure 4.24. Spectral variations in a population of 50 cells and the spectral patterns obtained from the average spectrum of **(a)** one, **(b)** two, **(c)** five, **(d)** 10 and **(e)** 20 random cells in triplicates (red, blue, and black spectra) within a population of 50 cells. The average spectrum of 50 cells (yellow spectrum) was included in each group as comparison.

4.4. SERS SPECTRAL DATA UPON NANOMATERIAL EXPOSURE

4.4.1. The Background Spectra of Nanomaterials

The background spectra of the samples were acquired as the initial step of the analyses. ZnO NPs, TiO_2 NPs, and QDs did not give a different background spectrum than the NM-free, culture medium containing background spectrum (Figure 4.25). The spectrum only contained a sharp peak at 1002 cm^{-1} and two less prominent peaks at 1031 and 1041 cm^{-1}. The same spectrum was obtained for Raman measurements of samples both with or without cells. In Figure 4.25a, a typical average cellular spectrum was given with the average signal intensity obtained. It should be noted that the background spectrum had a constant signal intensity at the tested laser power and exposure time.

SWCNTs and MWCNTs, that are known to have high Raman scattering characteristics, had their unique spectral pattern even in the absence of AuNPs. With the 830 nm NIR laser, peaks at 495, 573, 826, 836, 998, 1061, 1127 and the D band at 1292 cm^{-1} were observed (Figure 4.25b). However, the signal intensity at the used laser settings was as low as 150 units. For MWCNTs, only a peak at 1307 cm^{-1} was observed, that was the D band of MWCNTs (Figure 4.25c). Again the signal intensity was very low, even lower than SWCNTs.

Although the contribution of the background spectra of SWCNTs and MWCNTs were not high in terms of spectral intensity, the interpretation of the peaks at mentioned regions were made cautiously.

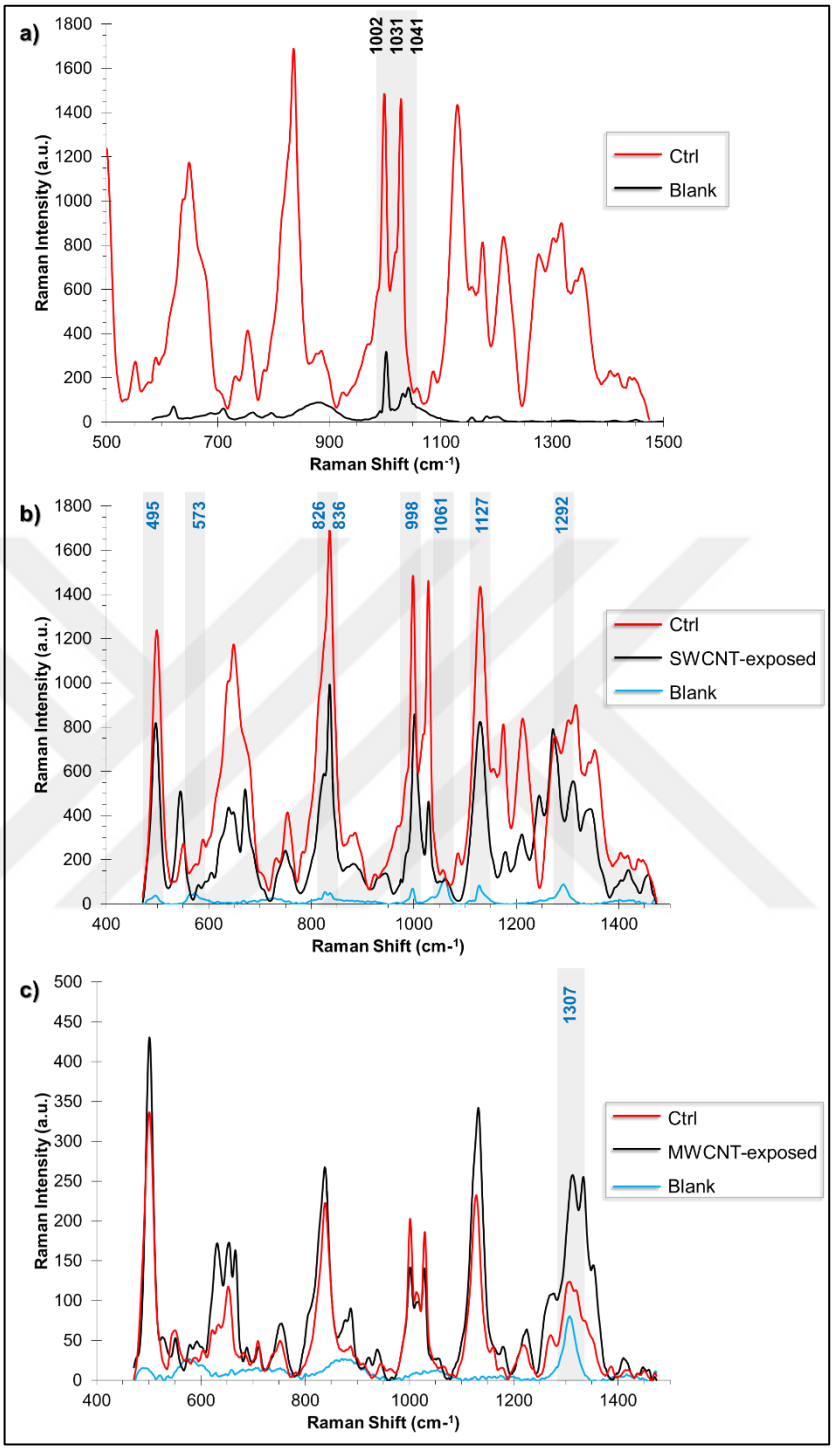

Figure 4.25. Background spectra of samples compared to cellular SERS spectra. **(a)** Background spectrum of ZnO NPs, TiO_2 NPs, and QDs. The spectrum also represents the Raman spectrum obtained from the samples with and without cells. **(b)** Background spectrum of SWCNTs and **(c)** MWCNTs.

4.4.2. Comparison of Cell-Line Dependent SERS Spectral Patterns

The SERS spectra obtained from each cell line were given in Figure 4.26 and the full list of peak assignments were given in Table 4.1. the visual inspection of the spectra already revealed the spectral variations between cell lines especially at Phe-related 1000 and 1030 cm^{-1} peaks.

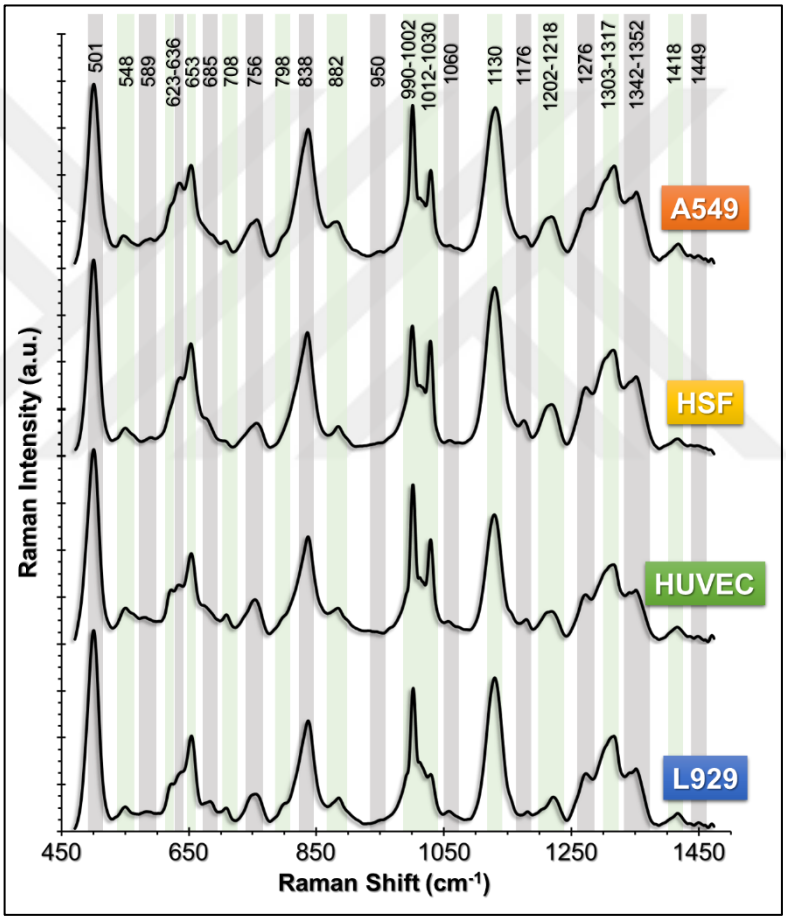

Figure 4.26. Average SERS spectra of each cell line in the absence of any NM exposure. The most prominent peaks were highlighted and their respective Raman shifts were given at the top of each line.

Table 4.1. Peak assignment list for SERS spectra [173].

Peak (cm^{-1})	**Assignment**
501	*v*(S-S) gauche-gauche-gauche
548	Cholesterol
589	OH out-of-plane bending (free)
623	C-C twisting of aromatic ring
636	*v*(C-S)
653	C-C twisting of Tyr
685	DNA, G ring breating
708	*v*(C-S) trans
756	DNA
798	O-P-O stretching
838	Tyr ring breath
882	Protein
950	Proline, α-helix
990-1002	Phe
1012	Trp ring breathing
1030	Phe in-plane bending
1060	C-C PO_2 stretch
1130	Phospholipid structural changes (trans versus gauche isomerism)
1176	Tyr
1202	Phe, Trp
1218	Protein
1276	Protein (α-helix)
1303	Lipid
1317	Amide III (α-helix)
1342	CH_3CH_2 wagging (collagen assignment)
1352	Protein (β-sheet)
1418	A,G
1449	CH_2 deformation of lipids and proteins

A more detailed analysis of the peaks correlates well with the current knowledge on the variations between these cell lines. The analyses were carried out through intensity ratios of

peaks assigned to several biomolecules, namely; collagen, fibronectin, cholesterol, phospholipids, the amino acids Phe and tyrosine (Tyr), as well as the C-S and S-S vibrational modes that can be easily affected from the redox reactions occurring in cells. The chosen intensity ratios help understand extracellular matrix (ECM)-related changes, membrane deformation or structural changes, inflammation and ROS activity, all of which can be indictors of toxic response initiated upon NM exposure.

Collagen, an ECM protein that is extensively produced by fibroblasts, mostly consists of α-helix structure and proline (Pro) or hydroxyproline residues [174], [175]. Therefore, the intensity ratio $I_{collagen}$ was calculated from (1342/950) cm^{-1}. As expected, the fibroblast cell lines HSF and L929 gave the highest values (Table 4.2).

Table 4.2. SERS intensity ratios of control samples that are the four cell lines used in NM toxicity studies. Each row was highlighted with a color code (from green to red) that indicate the increasing values of each intensity ratio.

Ratio	A549	HSF	HUVEC	L929
$I_{collagen}$	4.06	5.76	4.09	5.00
$I_{Fibronectin}$	2.4	2.5	3.6	3.2
$I_{Phe/Tyr}$	1.21	1.02	1.28	2.16
$I_{TyrPhos}$	0.31	0.21	0.30	0.28
$I_{Cholesterol}$	0.71	0.55	0.63	0.83
$I_{Lipid\ stability}$	6.96	11.05	5.66	7.52
I_{CS-SS}	2.45	4.41	1.67	2.16

Fibronectin, on the other hand, was highest in HUVECs. The ratio for fibronectin $I_{Fibronectin}$ was calculated from (501/1352) cm^{-1}, from the peaks assigned to S-S vibrations and β-sheet structures of proteins because fibronectins consist of β-sheets connected with disulfide bridges [176].

Phe/Tyr conversion by phenylalanine hydroxylases (PAHs) was shown to be impaired at inflammatory conditions and has been used as an **inflammation marker** [177]. Therefore,

$I_{Phe/Tyr}$ was calculated from the ratio of peak intensities assigned to Phe in-plane bend (1030 cm^{-1}) vibrations to Phe symmetric (1002 cm^{-1}) vibrations, divided by Tyr C-C twisting (653 cm^{-1}) vibrations to Tyr ring breathing (838 cm^{-1}) vibrations for Phe deformation and Tyr deformation, respectively. The overall ratio was (1030/1002)/(653/838) cm^{-1}. For the control group, the highest $I_{Phe/Tyr}$ was calculated for L929 cell line. Compared to HSF cell line, which ranked the second highest value, L929 cell line was previously shown to have a larger pool of Phe than Tyr at normal conditions. Thus, the calculated ratios were in-line with the literature [178].

Tyrosine phosphorylation is one of the early markers of oxidative stress and is increased in cancer cells [179]. The ratio $I_{TyrPhos}$ was thus calculated from (798/653) cm^{-1} assigned to O-P-O stretch and Tyr C-C twisting vibrations. The adenocarcinoma cell line, A549, ranked the highest value for $I_{TyrPhos}$ among the other cell lines.

Cholesterol is a vital component of cell membranes and helps providing fluidity to the membrane, through the formation of lipid rafts and is important for efficient particle uptake [66]. The ratio of phospholipid peak (1060 cm^{-1}) to cholesterol peak (548 cm^{-1}) is therefore can be an important indicator of **cholesterol depletion**, which was shown to play role in cytoskeleton reorganization and membrane stiffness [180]. Among the four cell lines, the highest cholesterol depletion, $I_{Cholesterol}$, was calculated for L929 cell line.

Cell membrane also contains a large portion of phospholipids. Upon external stress these phospholipids might be peroxidized and lead to membrane leakage or further structural deformations [181]. The ratio, $I_{Lipid\ stability}$, was thus calculated from (1130/1060) cm^{-1}, where 1130 cm^{-1} is assigned to phospholipid trans-gauche isomerism, to determine the level of **phospholipid stability**. For the control samples, the highest value was obtained from HSF cell line.

One other **oxidative stress indicator** is the ratio of S-S vibrational peaks (501 cm^{-1}) to C-S vibrational peaks (708/636 cm^{-1}, the ratio of *ν*(C-S) trans vibrations to *ν*(C-S) vibrations) termed as I_{CS-SS}. C-S groups are very sensitive to their environmental changes in terms of redox potentials [182]. Therefore, tracing the changes of this ratio can give precious information on the cellular oxidative stress. The higher the I_{CS-SS} ratio, the more disulfide formation is expected. For the control groups, HSF showed the highest I_{CS-SS} value (4.41), approximately 2.6 times more than HUVECs (1.67). In a study by Stone *et al.*, it was

reported that the antioxidant capacity of HUVECs were higher than HSF cell line, which could also be observed from the calculated I_{CS-SS} values because an increased antioxidant activity would result in a higher degree of free **C-S formation** [182].

4.4.3. Comparison of SERS Spectral Patterns upon Nanomaterial Exposure

The intensity ratios that were found to be convenient for toxicity determination were calculated for the four cell lines upon exposure to each of the five NMs at increasing concentrations, independently. The toxicity of NMs was evaluated based on cell-type specific responses.

4.4.3.1. A549 Cell Line

Being of cancer origin, A549 adenocarcinoma cell line have a greater tendency to be resistant to oxidative stress than the healthy cells [183]. This phenomenon was also traced in the SERS intensity ratios especially in I_{CS-SS} fluctuations.

For instance, ZnO NPs that are known to induce oxidative stress in cells did not cause a sudden decrease in I_{CS-SS} value at increasing ZnO NP concentrations. Therefore, inflammation ($I_{Phe/Tyr}$) and cholesterol depletion ($I_{Cholesterol}$) assigned ratios were quite stable (Figure 4.27). However, above 15 μg/ml dose I_{CS-SS} showed a sharp decrease which also resulted in loss of collagen ($I_{Collagen}$) and phospholipid stability ($I_{Lipid\ stability}$), whereas fibronectin assigned $I_{Fibronectin}$ increased significantly. The gradual decrease of $I_{Lipid\ stability}$ can be due to membrane lipid peroxidation causing a sudden viability decrease at above 15 μg/ml ZnO NP concentration.

TiO_2 NPs, on the other hand, resulted in an increasing trend in I_{CS-SS} ratio (Figure 4.28). A mild increase in oxidative stress was shown to induce cell survival which might also be the case in TiO_2 NP exposure [184]. A mild decrease in $I_{Lipid\ stability}$ and $I_{Fibronectin}$ can be because of the oxidative as well as mechanical stress introduced by TiO_2 NPs on cells. It has been previously shown that mechanical stress causes relaxation of fibronectin β-sheets, leading to loss of secondary structure [185], [186].

Pristine SWCNTs that were used in this study are known to be hydrophobic which makes them prefer interacting with hydrophobic molecules around them, which is the cell membrane at first place. From the intensity ratios it was observed that $I_{Fibronectin}$ increased in response to stress caused upon exposure to SWCNTs (Figure 4.29). Although I_{CS-SS} had a decrease at 0.1 mg/ml SWCNT concentration, the ratio was stable at higher doses, indicating and confirming the existing literature that the stress caused by SWCNTs was also through their physical presence on cells. SWCNTs were shown to indirectly damage the cell through depleting the cell culture medium proteins and lead to starvation of cells [43]. From the calculated ratio $I_{Cholesterol}$ it could be said that SWCNT exposure caused massive cholesterol depletion and lipid instability as well as loss of collagen. One important point to note here is that the increase in peaks 1060 and 1130 cm^{-1} can be originating from the background spectrum of SWCNTs themselves as was also discussed in "Section 4.4.1.".

Another type of CNTs, MWCNTs, induced a relatively different response compared to SWCNTs. The relatively stable $I_{Cholesterol}$ levels were in agreement with a previous study by Cavallo and coworkers, where they showed MWCNT penetration into cells, instead of agglomerating/aggregating on the cell membrane at large amounts (Figure 4.30) [187]. The sharp increase followed by a sharp decrease of $I_{Lipid\ stability}$ ratio can be an indication of membrane blebbing followed by cell death [187]. At lower concentrations, MWCNTs induced inflammation that also cause an increase at $I_{Fibronectin}$ levels.

QDs that contain Cd are known to release Cd^{2+} ions leading to oxidative stress in cells [188]. This phenomenon was also observed in SERS spectra through the sudden decrease of I_{CS-SS}, leading to sharp decrease of $I_{Lipid\ stability}$ and $I_{Collagen}$, whereas an increase of $I_{TyrPhos}$, $I_{Phe/Tyr}$ and $I_{Fibronectin}$ (Figure 4.31). However, the high level of toxicity introduced by QDs led to decrease of $I_{Fibronectin}$ and cells were mostly dead at concentrations above 10 μg/ml.

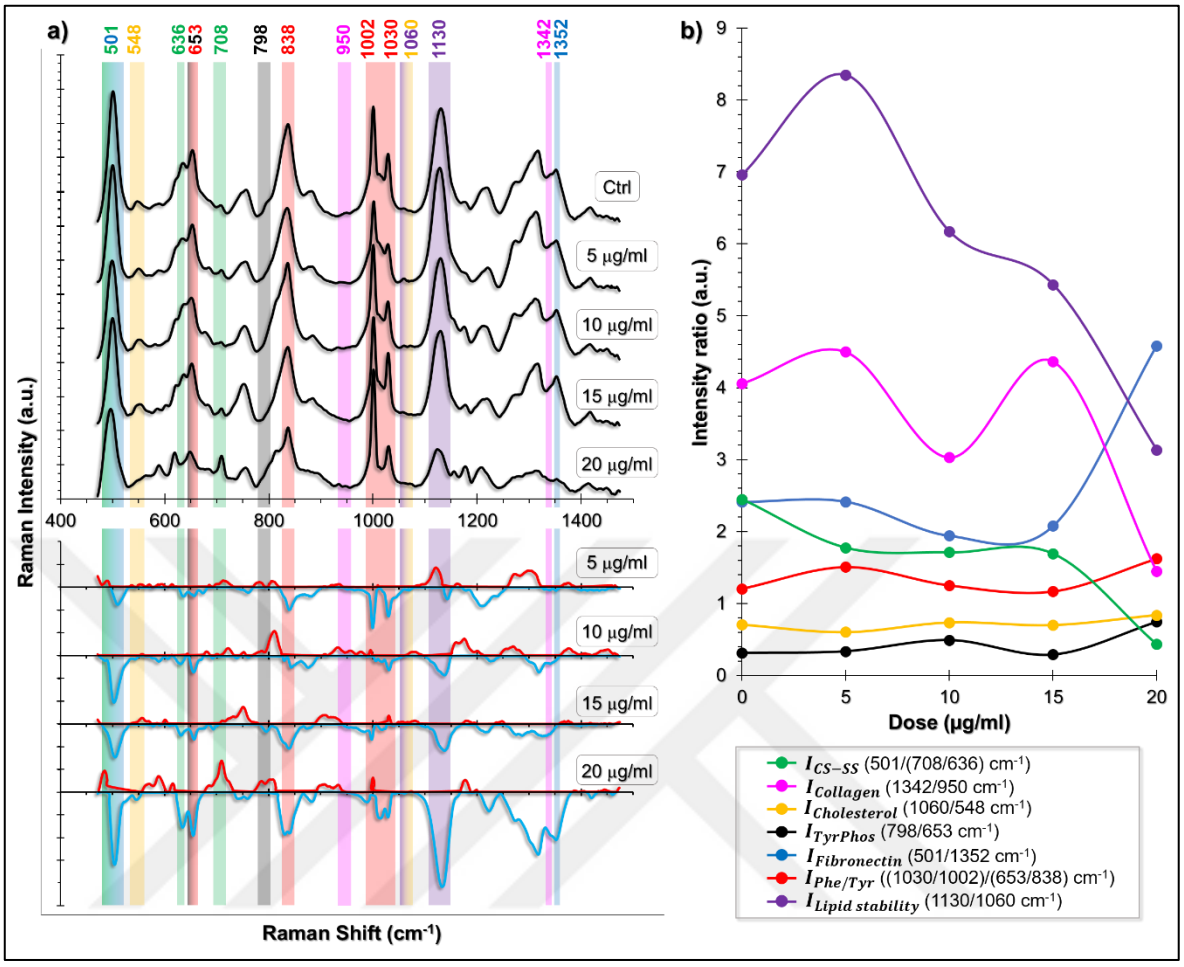

Figure 4.27. **(a)** SERS pattern of A549 cell line exposed to ZnO NPs at increasing concentrations. In the lower panel, NM-exposed spectra were subtracted from the control spectrum to better visualize the spectral differences. The highlighted areas show the spectral peaks that were used in **(b)** intensity ratio calculations and the color code depicts the respective intensity ratio. The two peaks that were used in intensity ratio calculations were highlighted with those two colors.

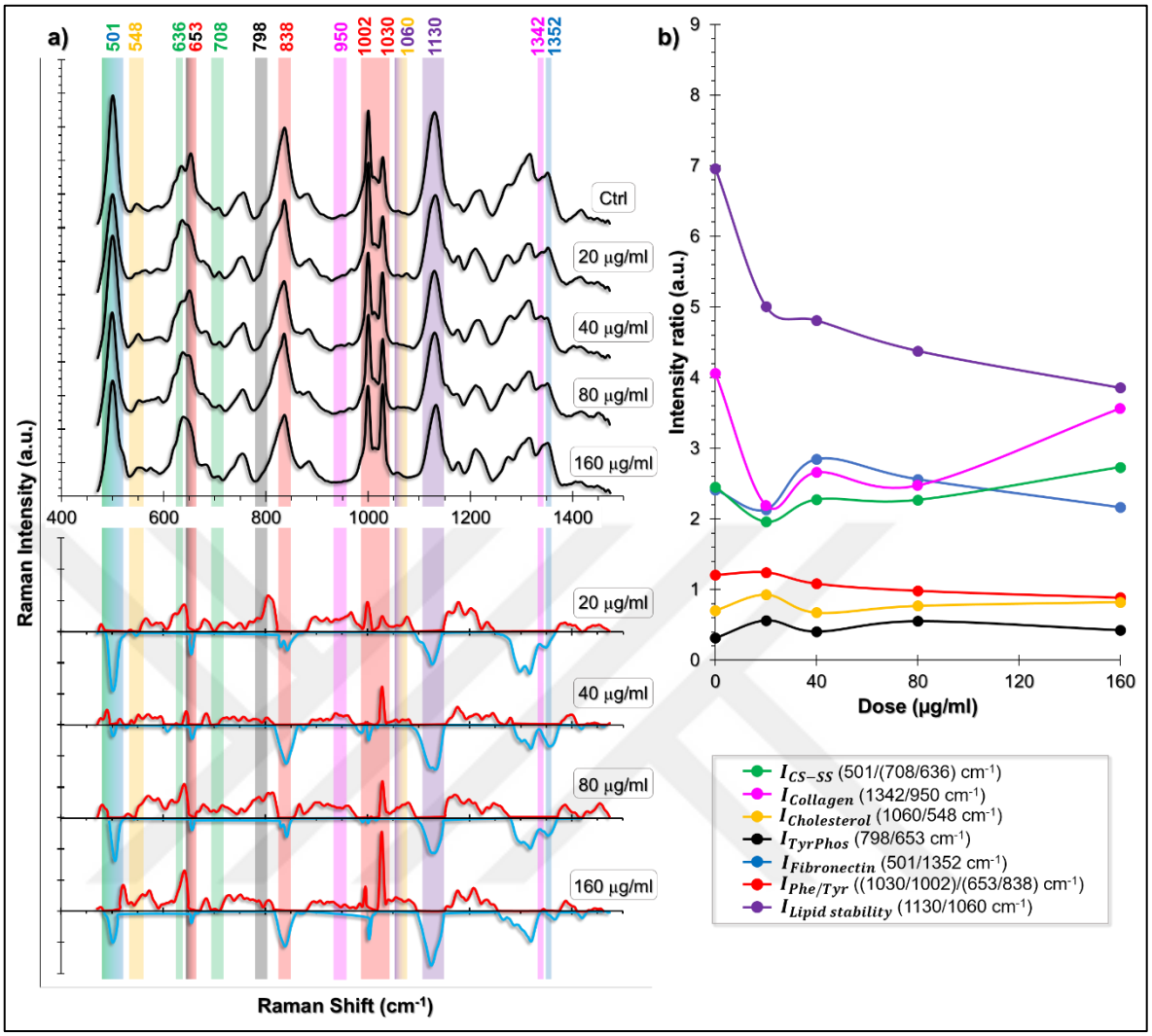

Figure 4.28. **(a)** SERS pattern of A549 cell line exposed to TiO_2 NPs at increasing concentrations. In the lower panel, NM-exposed spectra were subtracted from the control spectrum to better visualize the spectral differences. The highlighted areas show the spectral peaks that were used in **(b)** intensity ratio calculations and the color code depicts the respective intensity ratio. The two peaks that were used in intensity ratio calculations were highlighted with those two colors.

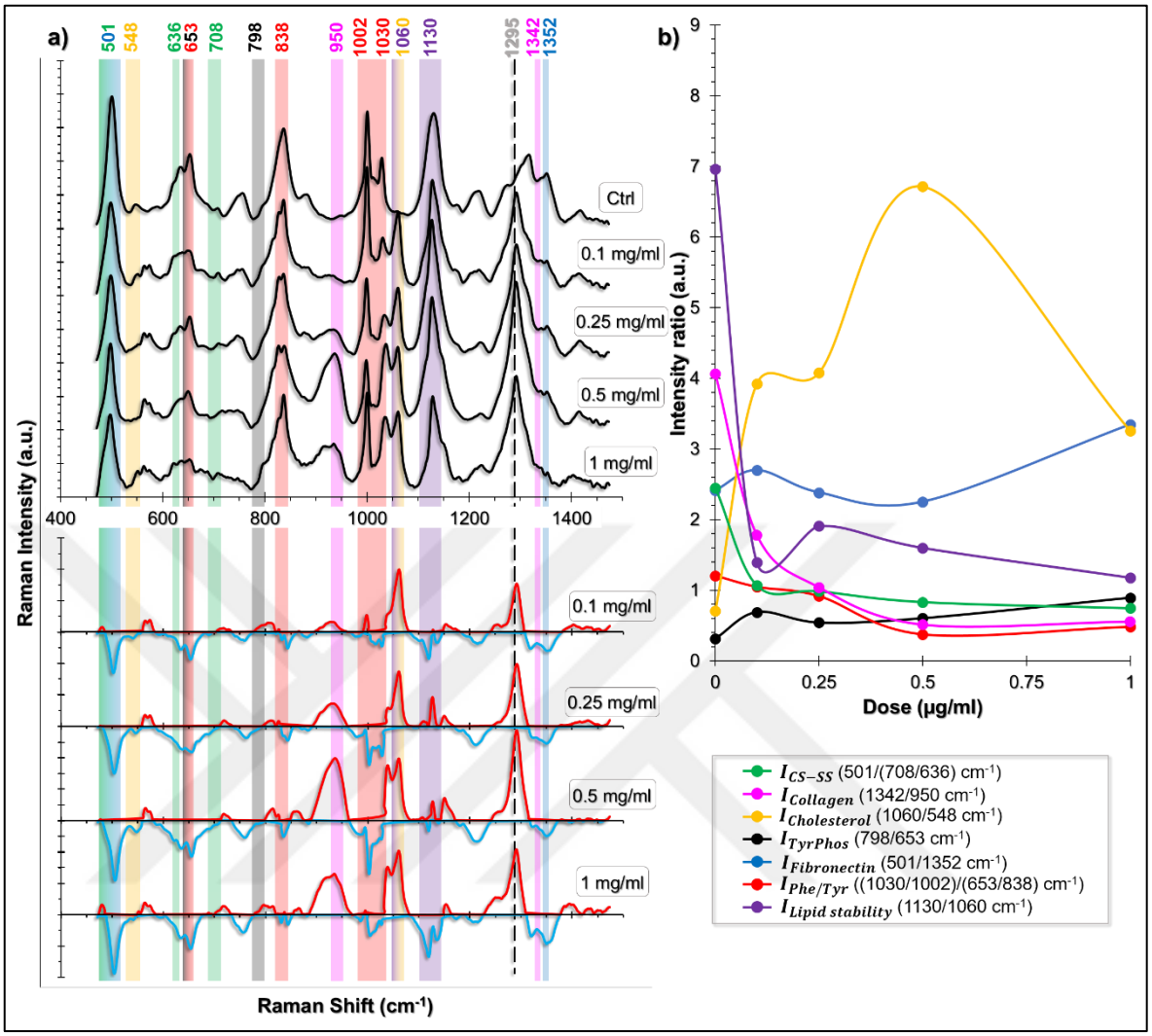

Figure 4.29. **(a)** SERS pattern of A549 cell line exposed to SWCNTs at increasing concentrations. In the lower panel, NM-exposed spectra were subtracted from the control spectrum to better visualize the spectral differences. The highlighted areas show the spectral peaks that were used in **(b)** intensity ratio calculations and the color code depicts the respective intensity ratio. The two peaks that were used in intensity ratio calculations were highlighted with those two colors. The peak belonging to SWCNTs was highlighted with a dashed line.

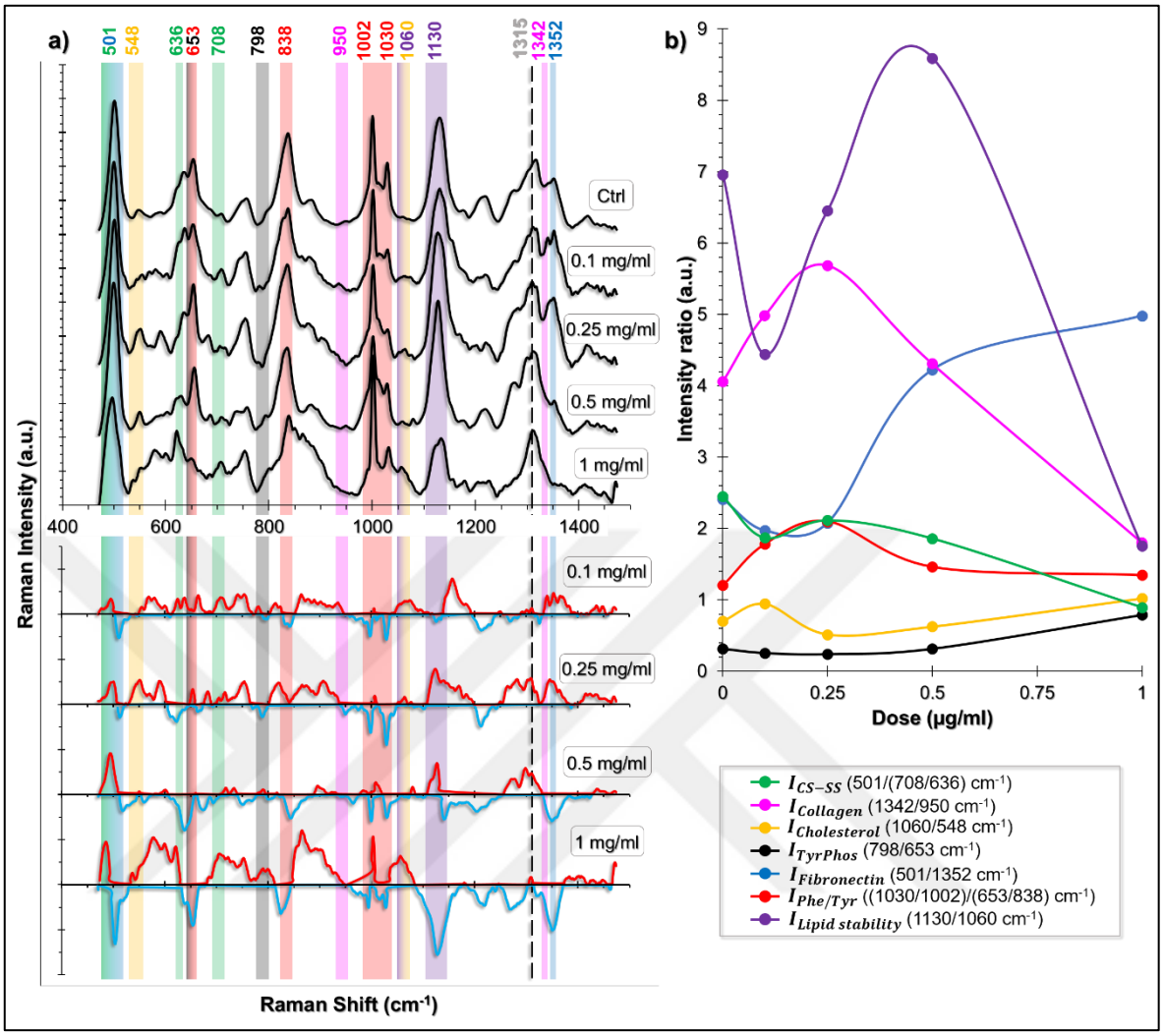

Figure 4.30. **(a)** SERS pattern of A549 cell line exposed to MWCNTs at increasing concentrations. In the lower panel, NM-exposed spectra were subtracted from the control spectrum to better visualize the spectral differences. The highlighted areas show the spectral peaks that were used in **(b)** intensity ratio calculations and the color code depicts the respective intensity ratio. The two peaks that were used in intensity ratio calculations were highlighted with those two colors. The peak belonging to MWCNTs was highlighted with a dashed line.

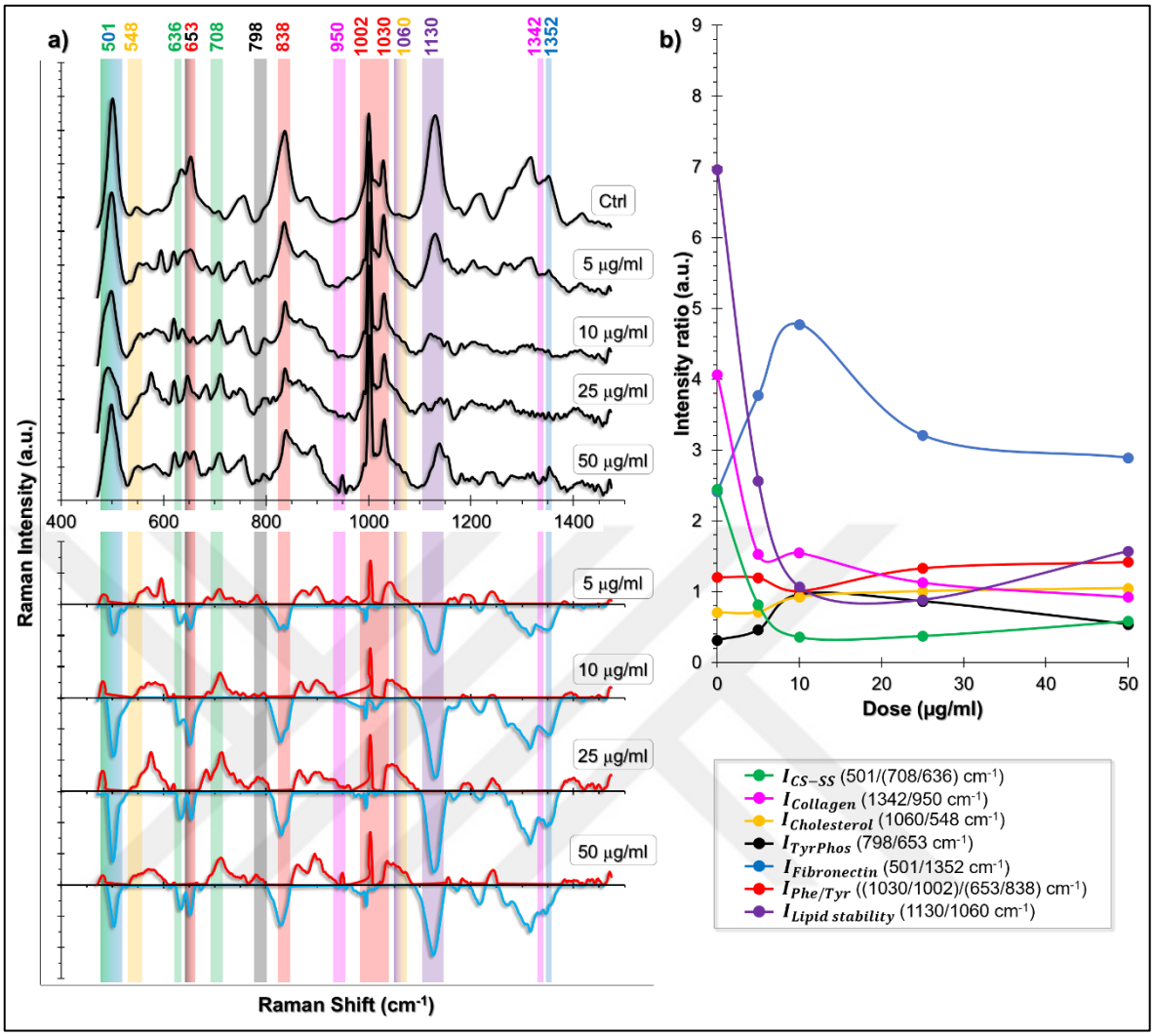

Figure 4.31. **(a)** SERS pattern of A549 cell line exposed to QDs at increasing concentrations. In the lower panel, NM-exposed spectra were subtracted from the control spectrum to better visualize the spectral differences. The highlighted areas show the spectral peaks that were used in **(b)** intensity ratio calculations and the color code depicts the respective intensity ratio. The two peaks that were used in intensity ratio calculations were highlighted with those two colors.

4.4.3.2. HSF Cell Line

The fibroblast cell line HSF was found to be more prone to damage upon ZnO NP exposure and the toxicity increase was in correlation with $I_{Phe/Tyr}$ inflammation-related ratio increase (Figure 4.32). Toxic response started with relatively sharp decrease of I_{CS-SS} and the loss of CS pool led to $I_{Phe/Tyr}$ increase. Inflammation increase was coupled to $I_{Fibronectin}$ increase and $I_{collagen}$ and $I_{Lipid\ stability}$ decrease.

TiO_2 NPs caused moderate oxidative stress that was apparently balanced through cellular defense systems because I_{CS-SS} levels were in a tendency to reach its starting values after a gradual decrease (Figure 4.33). Moreover, other ratios were mostly stable at all TiO_2 NP concentrations. On the other hand, lipid stability continued decreasing which can be an indication of lipid peroxidation as the main mechanism of damage to cells.

SWCNT (Figure 4.34), MWCNT (Figure 4.35) and QD (Figure 4.36) exposure on HSF cell line showed similar spectral trends to what was observed in A549 cell line. $I_{Fibronectin}$ levels were observed in SWCNT-exposed cells, whereas MWCNTs induced increased $I_{Phe/Tyr}$, indicating inflammatory response. QDs also showed increased $I_{Phe/Tyr}$ levels as well as $I_{TyrPhos}$ even though 10 µg/ml QD exposure was seen to be less toxic compared to a lower dose 5 µg/ml.

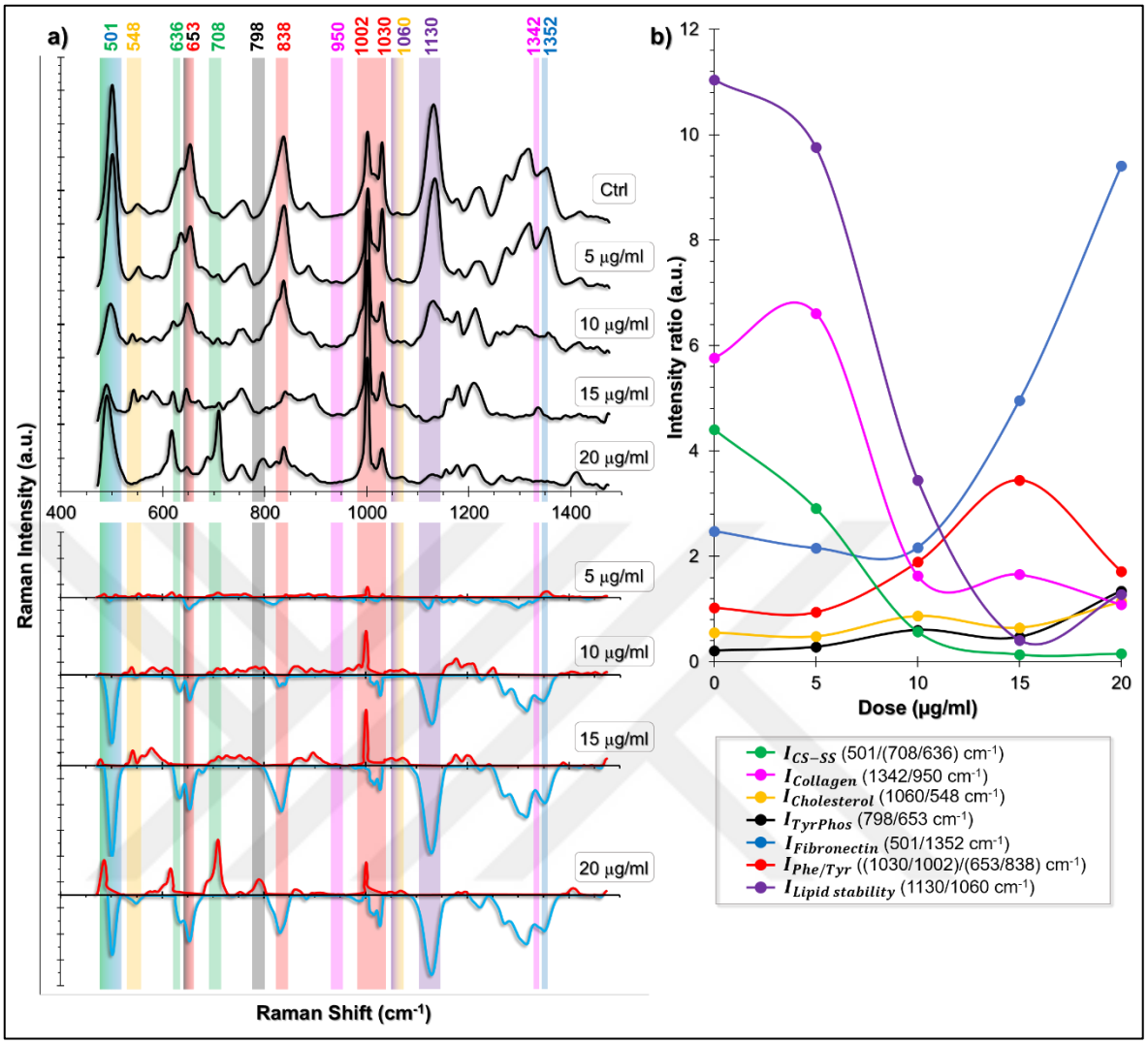

Figure 4.32. **(a)** SERS pattern of HSF cell line exposed to ZnO NPs at increasing concentrations. In the lower panel, NM-exposed spectra were subtracted from the control spectrum to better visualize the spectral differences. The highlighted areas show the spectral peaks that were used in **(b)** intensity ratio calculations and the color code depicts the respective intensity ratio. The two peaks that were used in intensity ratio calculations were highlighted with those two colors.

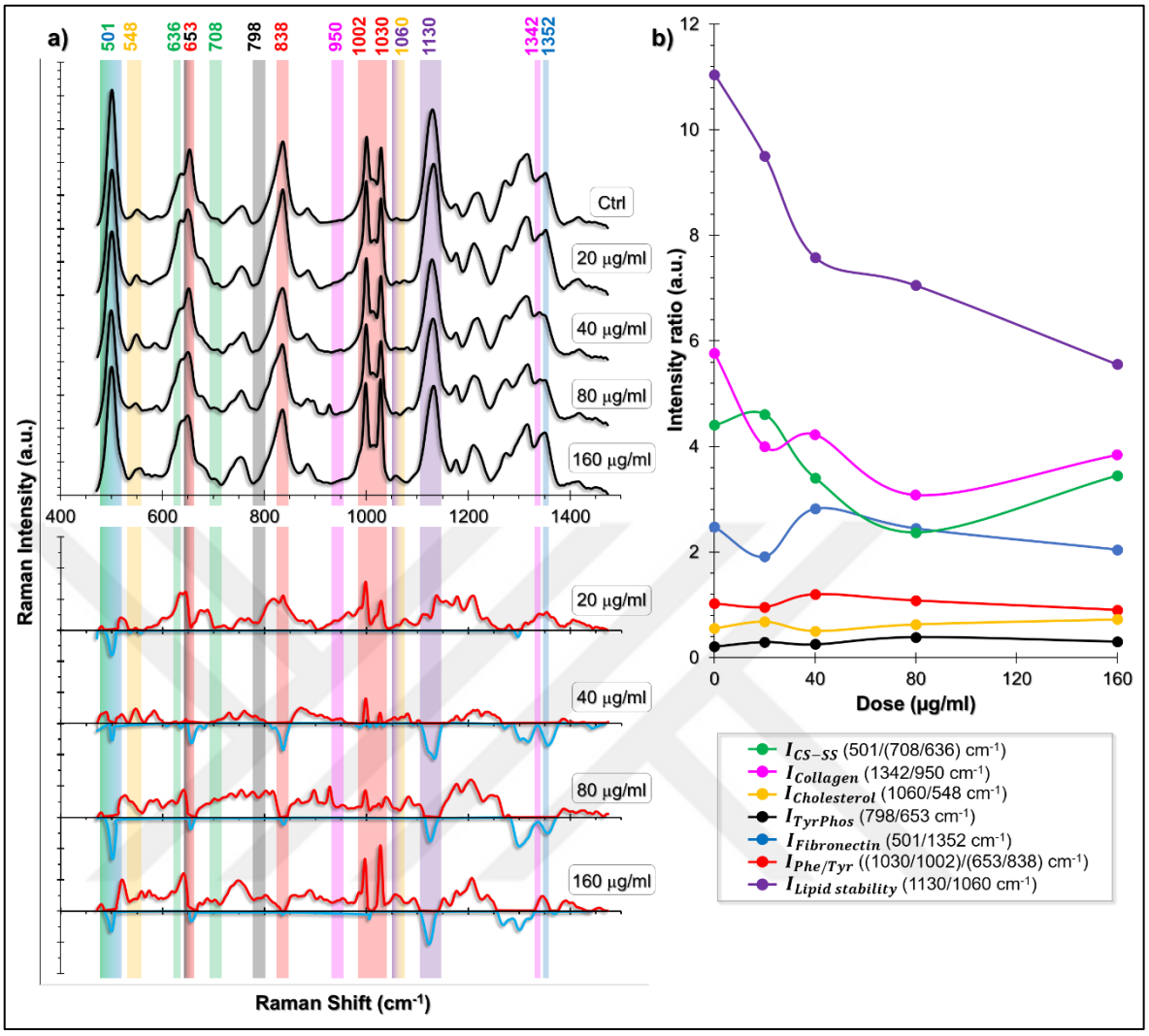

Figure 4.33. **(a)** SERS pattern of HSF cell line exposed to TiO_2 NPs at increasing concentrations. In the lower panel, NM-exposed spectra were subtracted from the control spectrum to better visualize the spectral differences. The highlighted areas show the spectral peaks that were used in **(b)** intensity ratio calculations and the color code depicts the respective intensity ratio. The two peaks that were used in intensity ratio calculations were highlighted with those two colors.

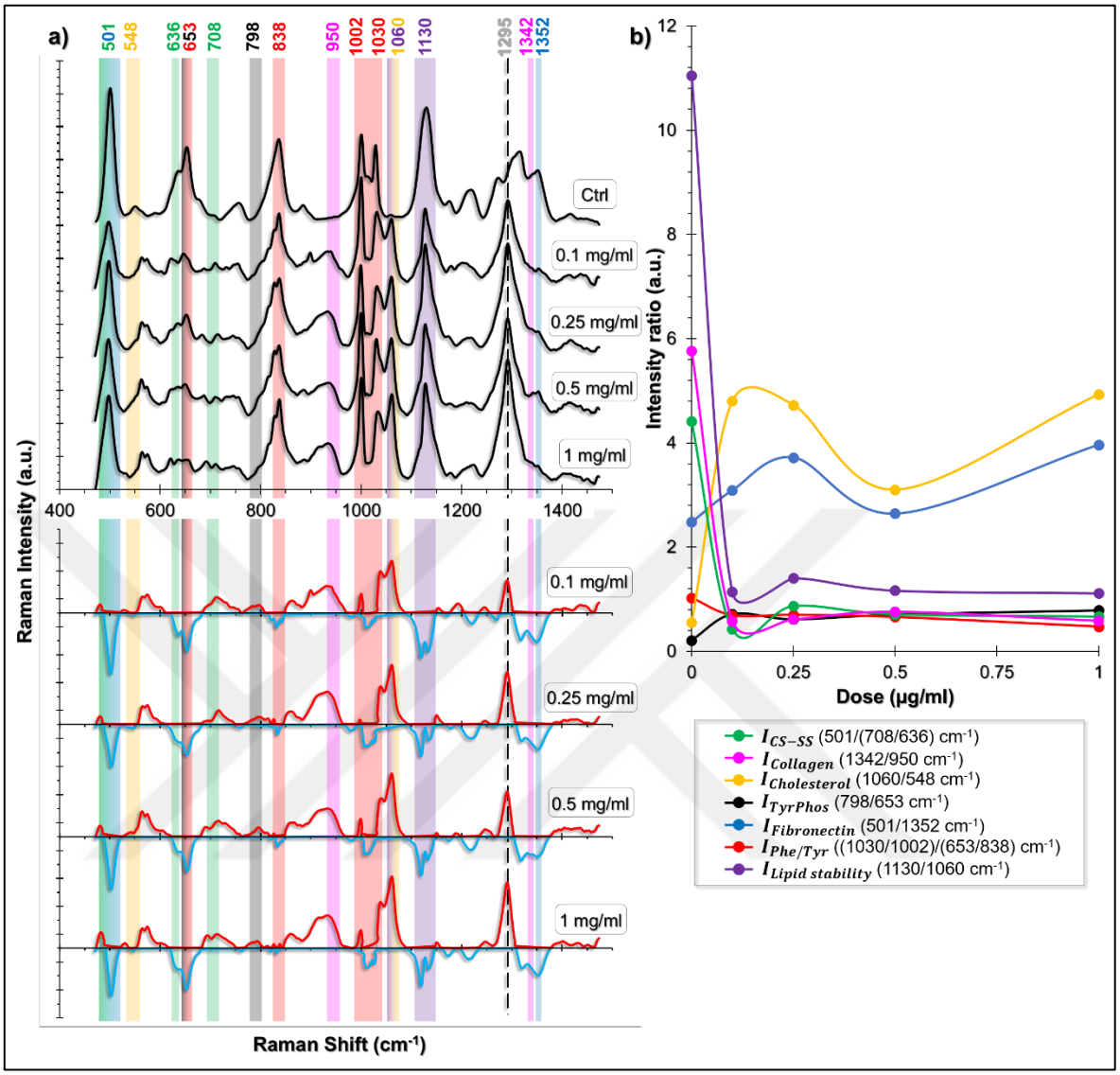

Figure 4.34. **(a)** SERS pattern of HSF cell line exposed to SWCNTs at increasing concentrations. In the lower panel, NM-exposed spectra were subtracted from the control spectrum to better visualize the spectral differences. The highlighted areas show the spectral peaks that were used in **(b)** intensity ratio calculations and the color code depicts the respective intensity ratio. The two peaks that were used in intensity ratio calculations were highlighted with those two colors. The peak belonging to SWCNTs was highlighted with a dashed line.

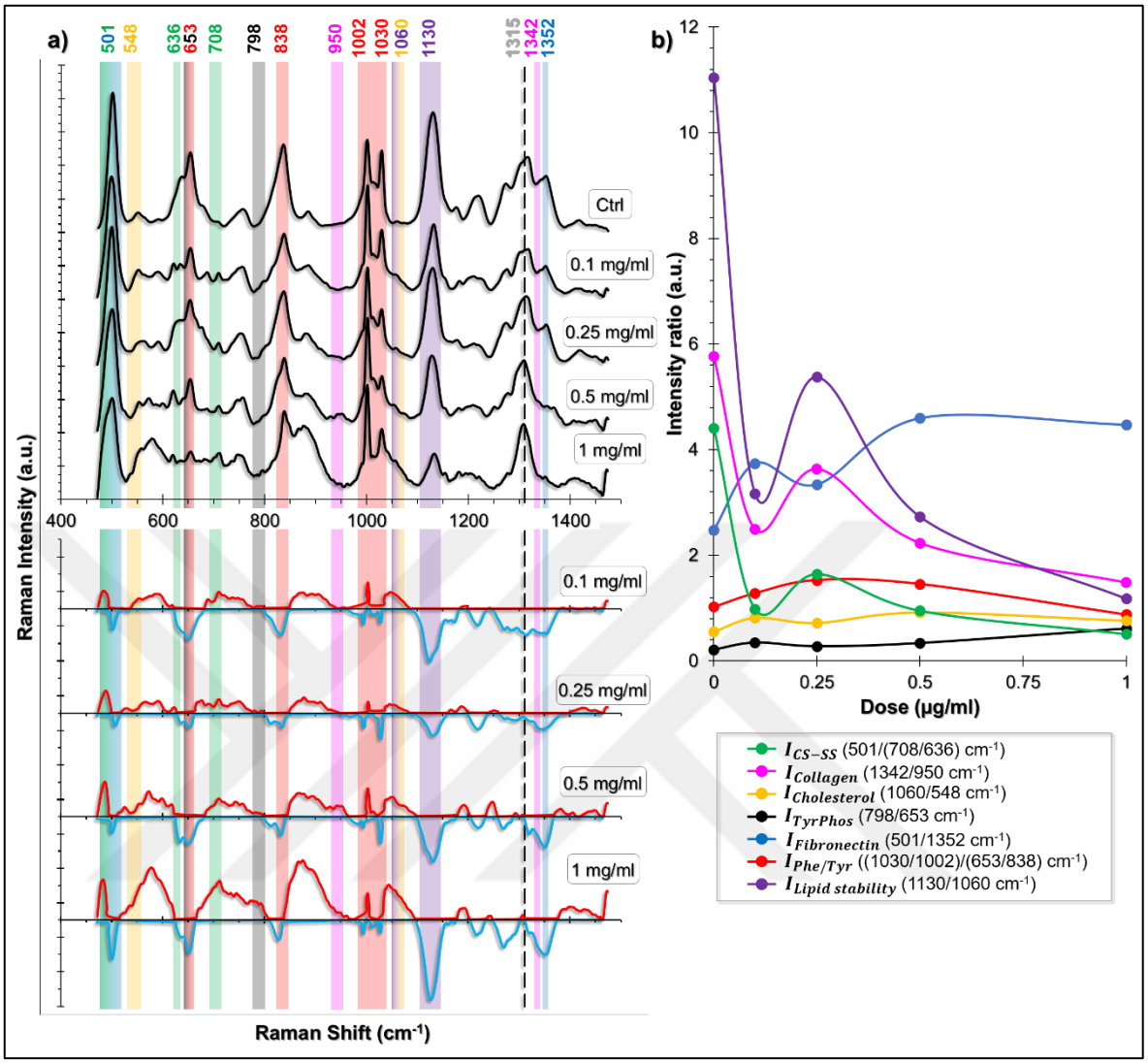

Figure 4.35. **(a)** SERS pattern of HSF cell line exposed to MWCNTs at increasing concentrations. In the lower panel, NM-exposed spectra were subtracted from the control spectrum to better visualize the spectral differences. The highlighted areas show the spectral peaks that were used in **(b)** intensity ratio calculations and the color code depicts the respective intensity ratio. The two peaks that were used in intensity ratio calculations were highlighted with those two colors. The peak belonging to MWCNTs was highlighted with a dashed line.

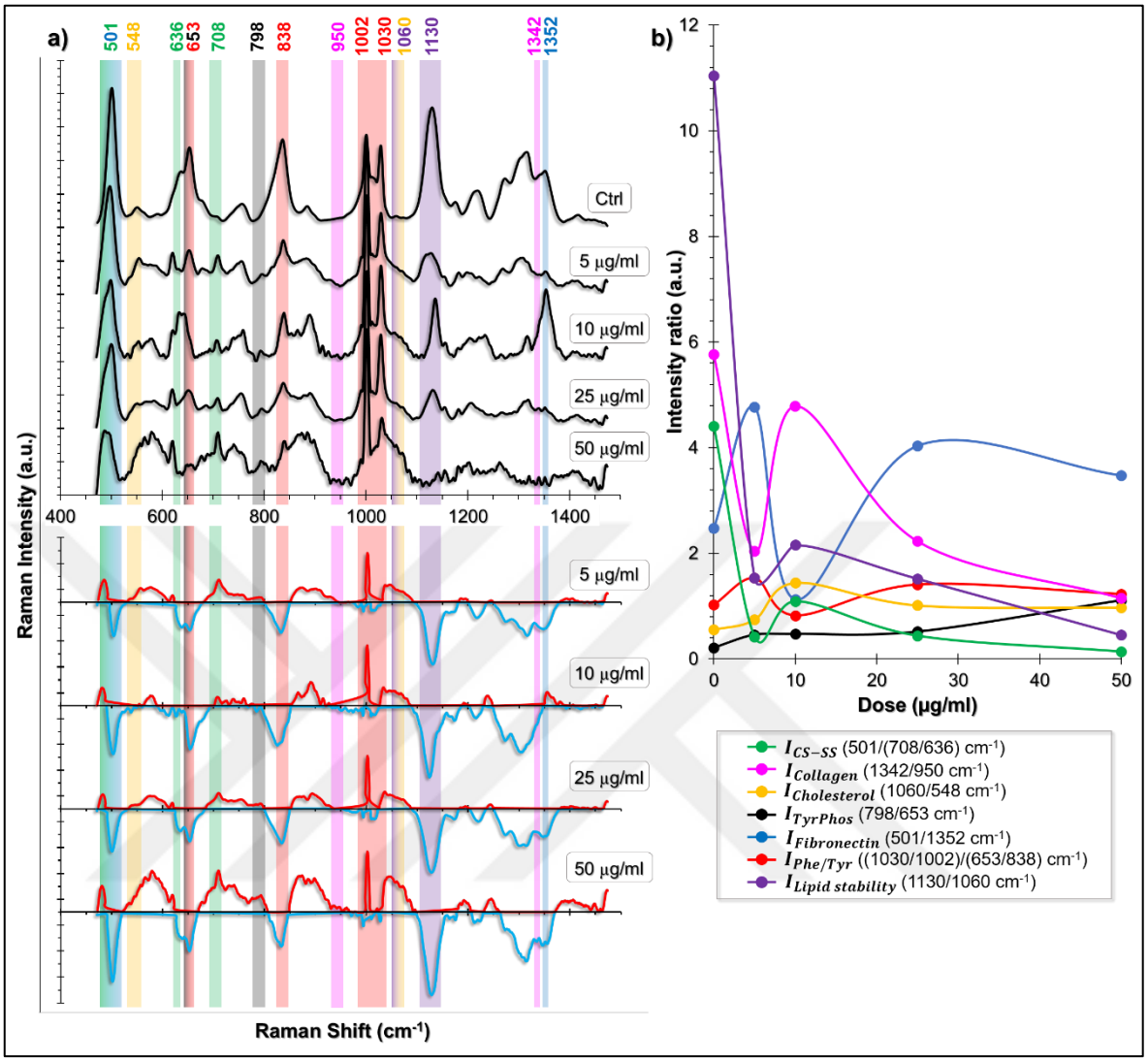

Figure 4.36. **(a)** SERS pattern of HSF cell line exposed to QDs at increasing concentrations. In the lower panel, NM-exposed spectra were subtracted from the control spectrum to better visualize the spectral differences. The highlighted areas show the spectral peaks that were used in **(b)** intensity ratio calculations and the color code depicts the respective intensity ratio. The two peaks that were used in intensity ratio calculations were highlighted with those two colors.

4.4.3.3. HUVEC Cell Line

Although in the previous section (Section 4.4.1.) the antioxidant capacity of HUVECs were calculated to be lower compared to other cell lines, I_{CS-SS} levels were found to be more stable and resistant to change upon NM exposure. For instance, as in the case for ZnO NP exposure, the stable I_{CS-SS} levels prevented remarkable decrease of $I_{Lipid\ stability}$ and $I_{collagen}$ (Figure 4.37). However, at a certain point, that is 15 μg/ml ZnO NPs, the accumulated oxidative stress led to the decrease of I_{CS-SS} and increase of $I_{TyrPhos}$ and $I_{Fibronectin}$.

Similarly, TiO_2 NPs caused milder toxicity to HUVECs compared to A549 and HSF cell lines due to more balanced I_{CS-SS} levels (Figure 4.38). Above 80 μg/ml TiO_2 NP concentration, however, oxidative stress caused lipid and collagen deformation whereas increased $I_{Fibronectin}$.

Another remarkable difference of HUVEC intensity ratios was in $I_{Fibronectin}$ levels. The already-higher value of this ratio was more resistant to further changes, indicating a higher level of defense capability of this cell line upon external damage. Although this was possible to be confirmed through the intensity ratios calculated for each NM for HUVECs, the only significant exception was upon SWCNT exposure (Figure 4.39). Tyrosine phosphorylation increase, which was to an extent that was not observed in any other test group, led to massive oxidative stress coupled with an incredible increase of cholesterol depletion. Again, the cholesterol depletion ratio was not considered as relevant for this NM because of the possibility of SWCNT background signal contribution.

MWCNT (Figure 4.40) and QD (Figure 4.41) exposures caused mild toxicity again mostly through balanced CS-SS levels, even though high concentrations led cell death especially in QD-exposed cells. For MWCNT exposure, $I_{Lipid\ stability}$ decrease was the most remarkable change, indicating membrane damage could be the main cause of toxicity.

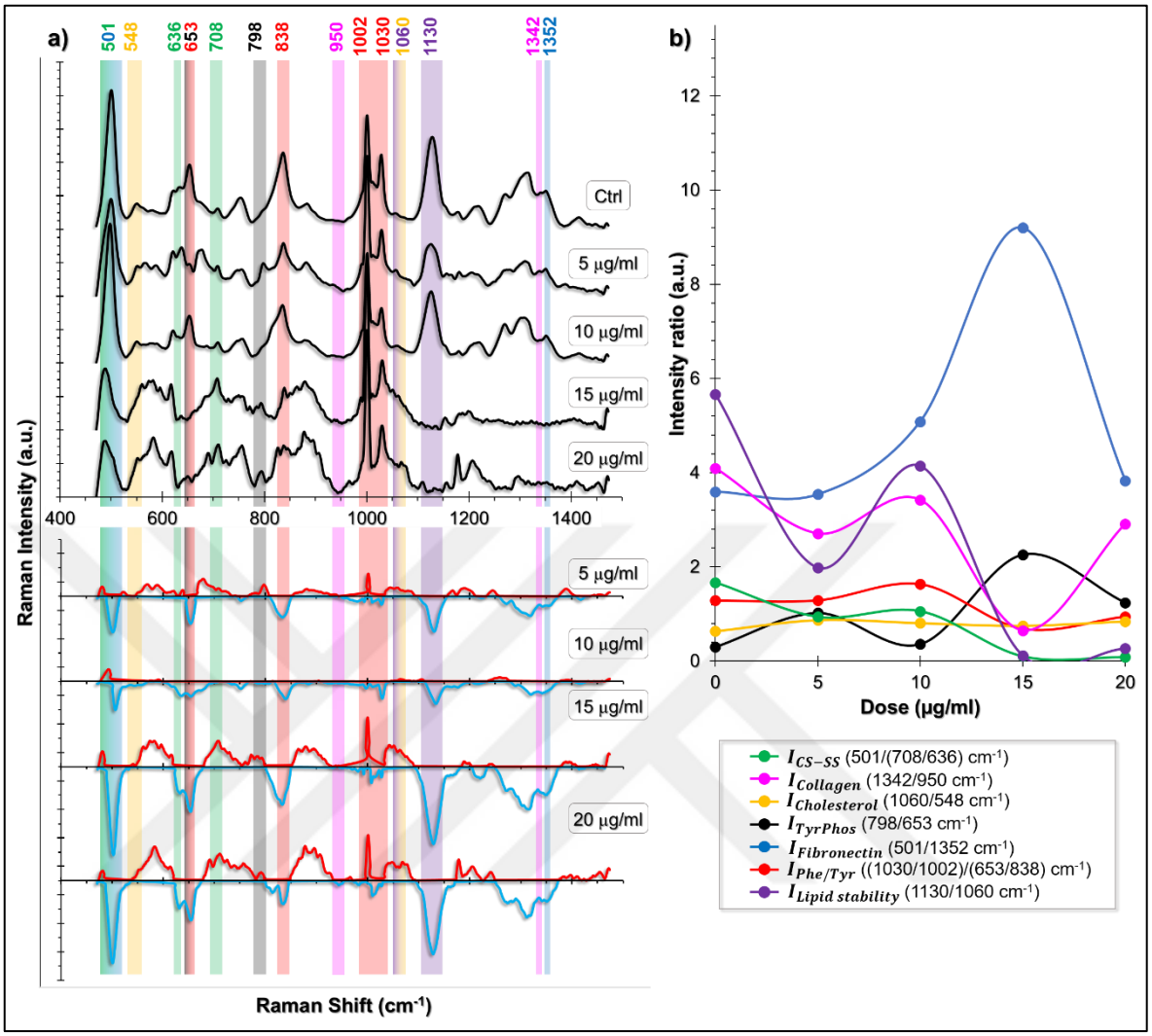

Figure 4.37. **(a)** SERS pattern of HUVEC cell line exposed to ZnO NPs at increasing concentrations. In the lower panel, NM-exposed spectra were subtracted from the control spectrum to better visualize the spectral differences. The highlighted areas show the spectral peaks that were used in **(b)** intensity ratio calculations and the color code depicts the respective intensity ratio. The peaks that were used in two intensity ratio calculations were highlighted with those two colors.

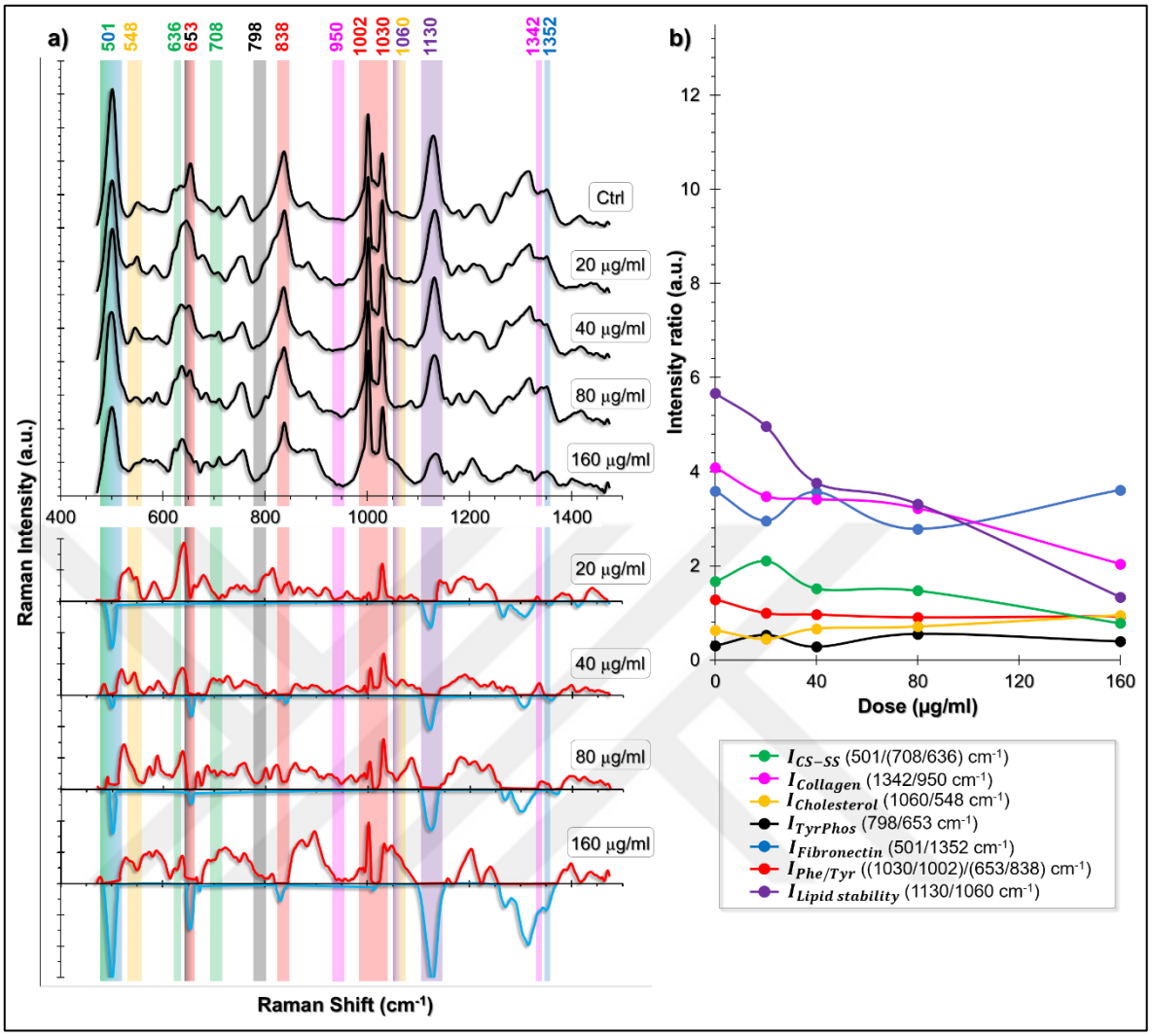

Figure 4.38. **(a)** SERS pattern of HUVEC cell line exposed to TiO_2 NPs at increasing concentrations. In the lower panel, NM-exposed spectra were subtracted from the control spectrum to better visualize the spectral differences. The highlighted areas show the spectral peaks that were used in **(b)** intensity ratio calculations and the color code depicts the respective intensity ratio. The two peaks that were used in intensity ratio calculations were highlighted with those two colors.

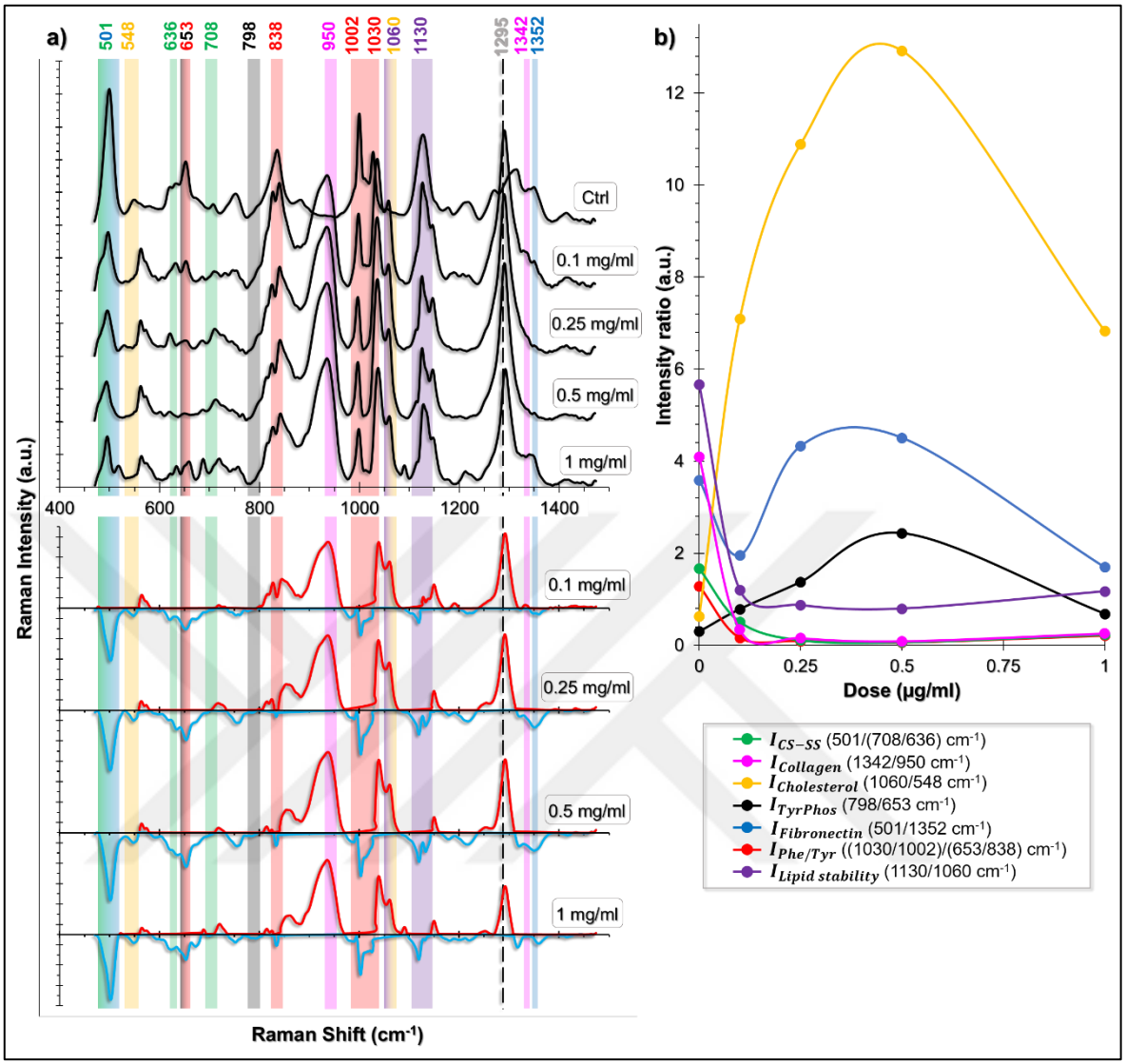

Figure 4.39. **(a)** SERS pattern of HUVEC cell line exposed to SWCNTs at increasing concentrations. In the lower panel, NM-exposed spectra were subtracted from the control spectrum to better visualize the spectral differences. The highlighted areas show the spectral peaks that were used in **(b)** intensity ratio calculations and the color code depicts the respective intensity ratio. The two peaks that were used in intensity ratio calculations were highlighted with those two colors. The peak belonging to SWCNTs was highlighted with a dashed line.

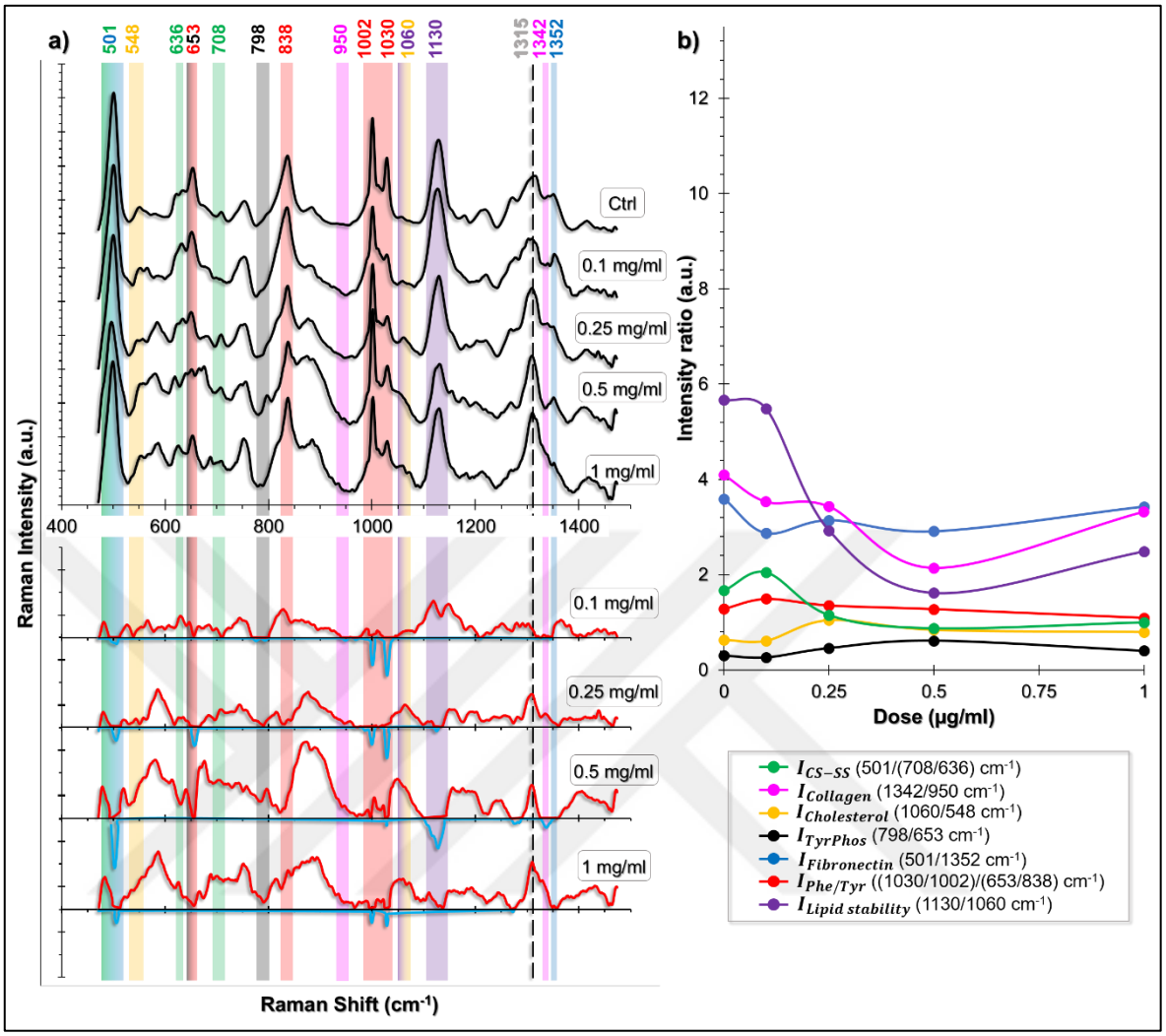

Figure 4.40. **(a)** SERS pattern of HUVEC cell line exposed to MWCNTs at increasing concentrations. In the lower panel, NM-exposed spectra were subtracted from the control spectrum to better visualize the spectral differences. The highlighted areas show the spectral peaks that were used in **(b)** intensity ratio calculations and the color code depicts the respective intensity ratio. The two peaks that were used in intensity ratio calculations were highlighted with those two colors. The peak belonging to MWCNTs was highlighted with a dashed line.

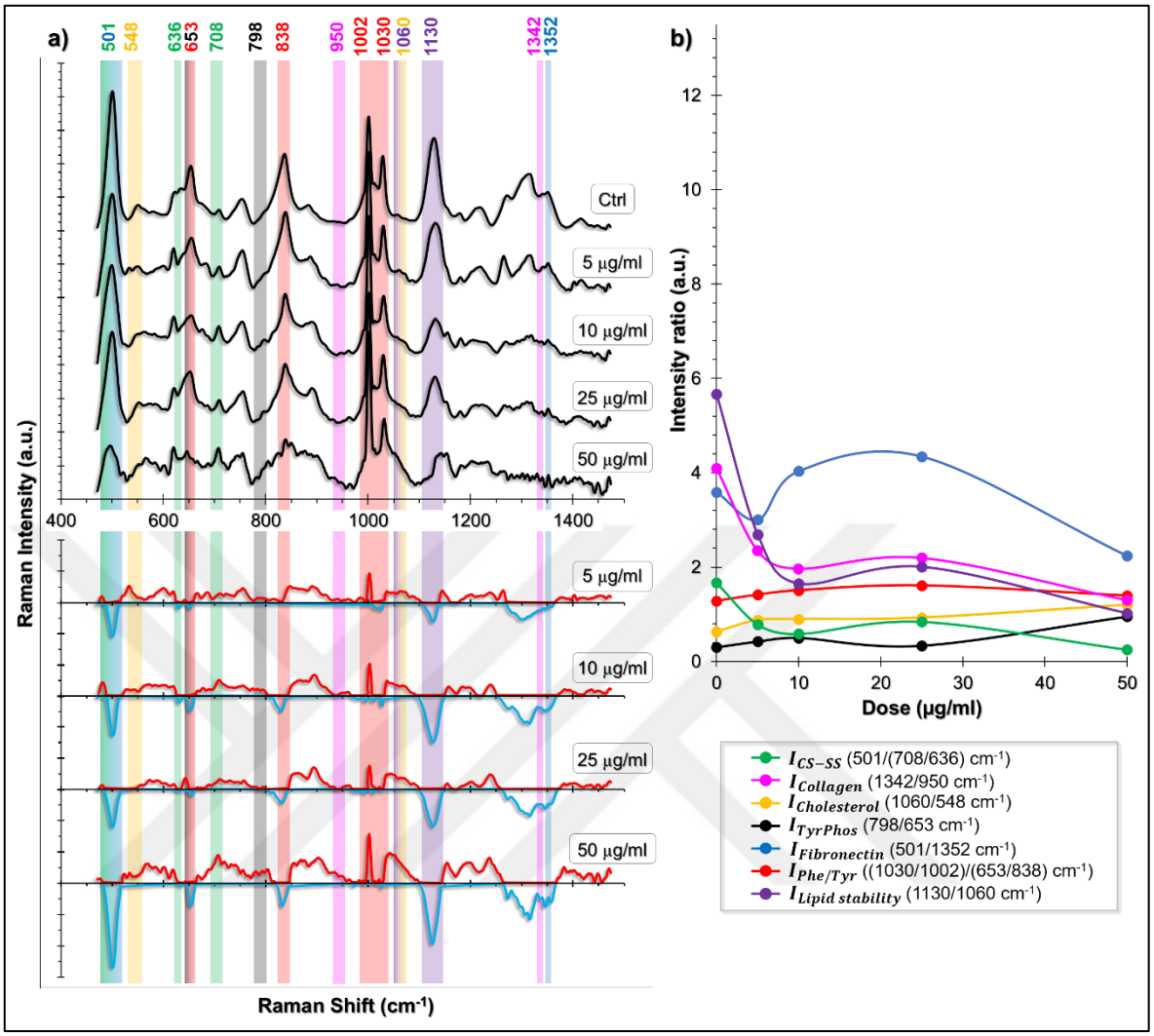

Figure 4.41. **(a)** SERS pattern of HUVEC cell line exposed to QDs at increasing concentrations. In the lower panel, NM-exposed spectra were subtracted from the control spectrum to better visualize the spectral differences. The highlighted areas show the spectral peaks that were used in **(b)** intensity ratio calculations and the color code depicts the respective intensity ratio. The two peaks that were used in intensity ratio calculations were highlighted with those two colors.

4.4.3.4. L929 Cell Line

The mouse fibroblast cell line L929 is known to produce cholesterol-poor high density lipoproteins (HDL), have less overall cholesterol content and was also calculated in Section 4.4.1. to have the highest cholesterol depletion $I_{Cholesterol}$ ratio [189]. Knowing the importance of cholesterol homeostasis and presence in membrane stability, $I_{Lipid\ stability}$ was the most affected intensity ratio in L929 cells, regardless of the type of exposed NMs. ZnO NPs caused an almost linear decrease in $I_{Lipid\ stability}$ with increasing ZnO NP concentration, whereas $I_{Phe/Tyr}$ and $I_{TyrPhos}$ levels increased at 15 µg/ml ZnO NP (Figure 4.42). The pattern of the ratios was similar to the HSF fibroblasts.

The response observed in TiO_2 NP-exposed L929 cell line was exceptional to the other three cell lines used. $I_{Lipid\ stability}$ as well as I_{CS-SS} levels significantly increased whereas other ratios were almost stable (Figure 4.43). From the knowledge that oxidative stress might cause both proliferative and anti-proliferative effect on cells depending on its extent, it can be speculated that the possible mild oxidative stress might have caused this positive effect on the cells.

SWCNT (Figure 4.44) and MWCNT (Figure 4.45) exposure response was again similar to HSF cell line. Cholesterol depletion was not in excess amount. Interestingly, the relatively increased I_{CS-SS} value at 0.25 mg/ml SWCNT exposure might be related to the increased $I_{Lipid\ stability}$ ratio at 0.5 mg/ml SWCNT exposure as a sign of cellular defence activation, which was seen already at the same dose of MWCNT exposure.

QD exposure response pattern was similar to what was obtained from HUVEC cell line (Figure 4.46). A very slight increase of $I_{Phe/Tyr}$ and $I_{TyrPhos}$ coupled with increase of $I_{Fibronectin}$ values indicated initiation of inflammation.

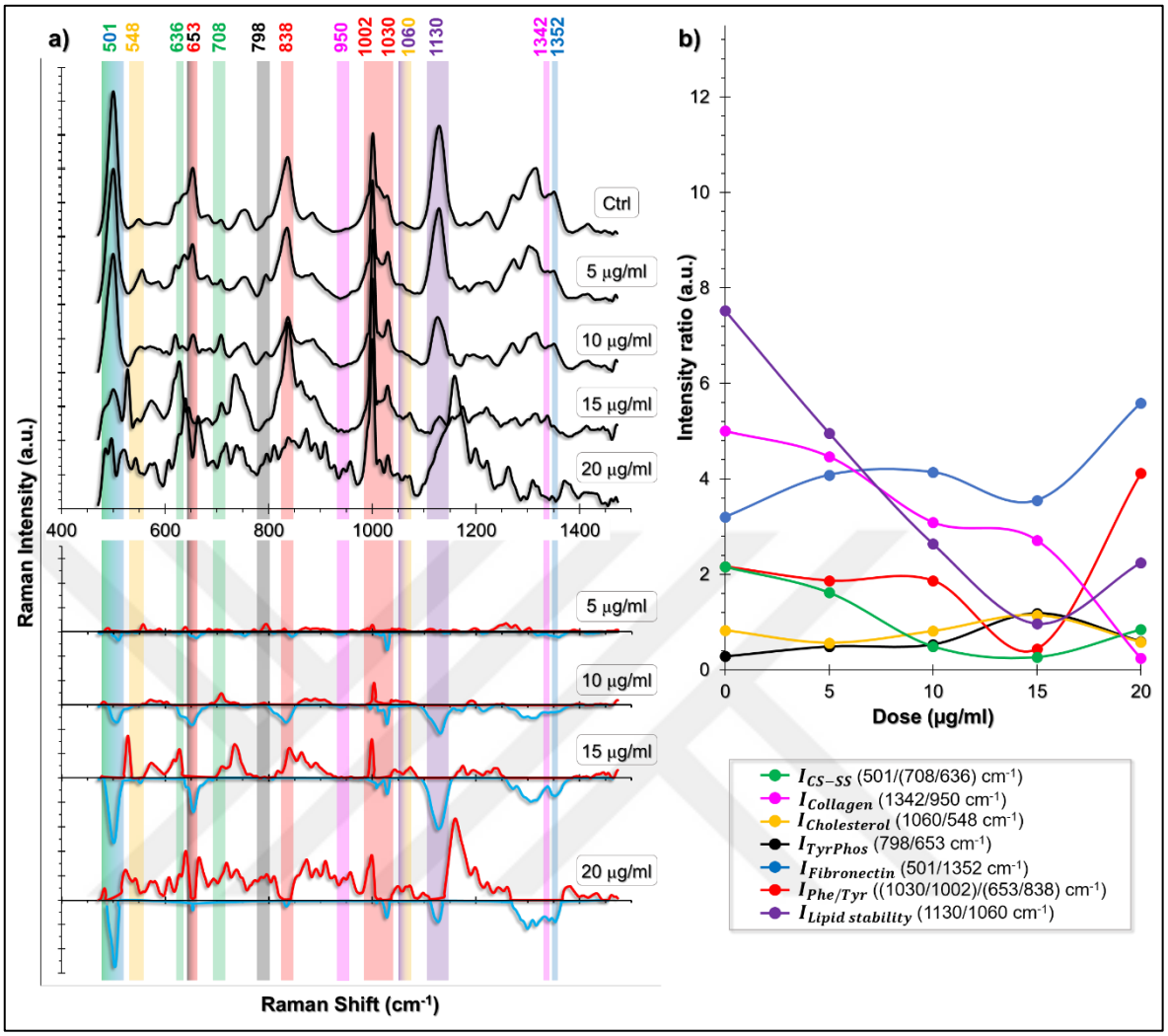

Figure 4.42. **(a)** SERS pattern of L929 cell line exposed to ZnO NPs at increasing concentrations. In the lower panel, NM-exposed spectra were subtracted from the control spectrum to better visualize the spectral differences. The highlighted areas show the spectral peaks that were used in **(b)** intensity ratio calculations and the color code depicts the respective intensity ratio. The two peaks that were used in intensity ratio calculations were highlighted with those two colors.

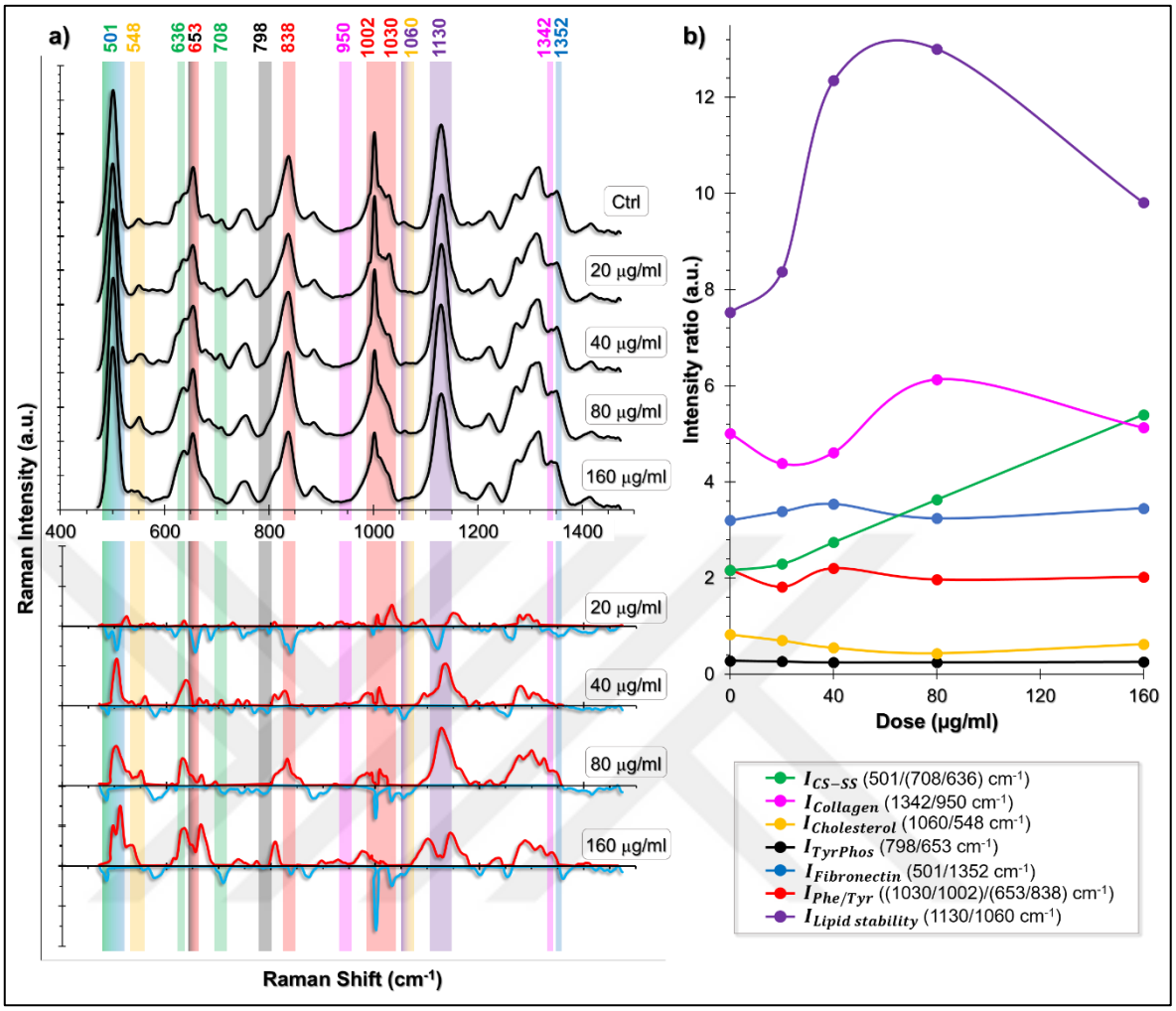

Figure 4.43. **(a)** SERS pattern of L929 cell line exposed to TiO_2 NPs at increasing concentrations. In the lower panel, NM-exposed spectra were subtracted from the control spectrum to better visualize the spectral differences. The highlighted areas show the spectral peaks that were used in **(b)** intensity ratio calculations and the color code depicts the respective intensity ratio. The two peaks that were used in intensity ratio calculations were highlighted with those two colors.

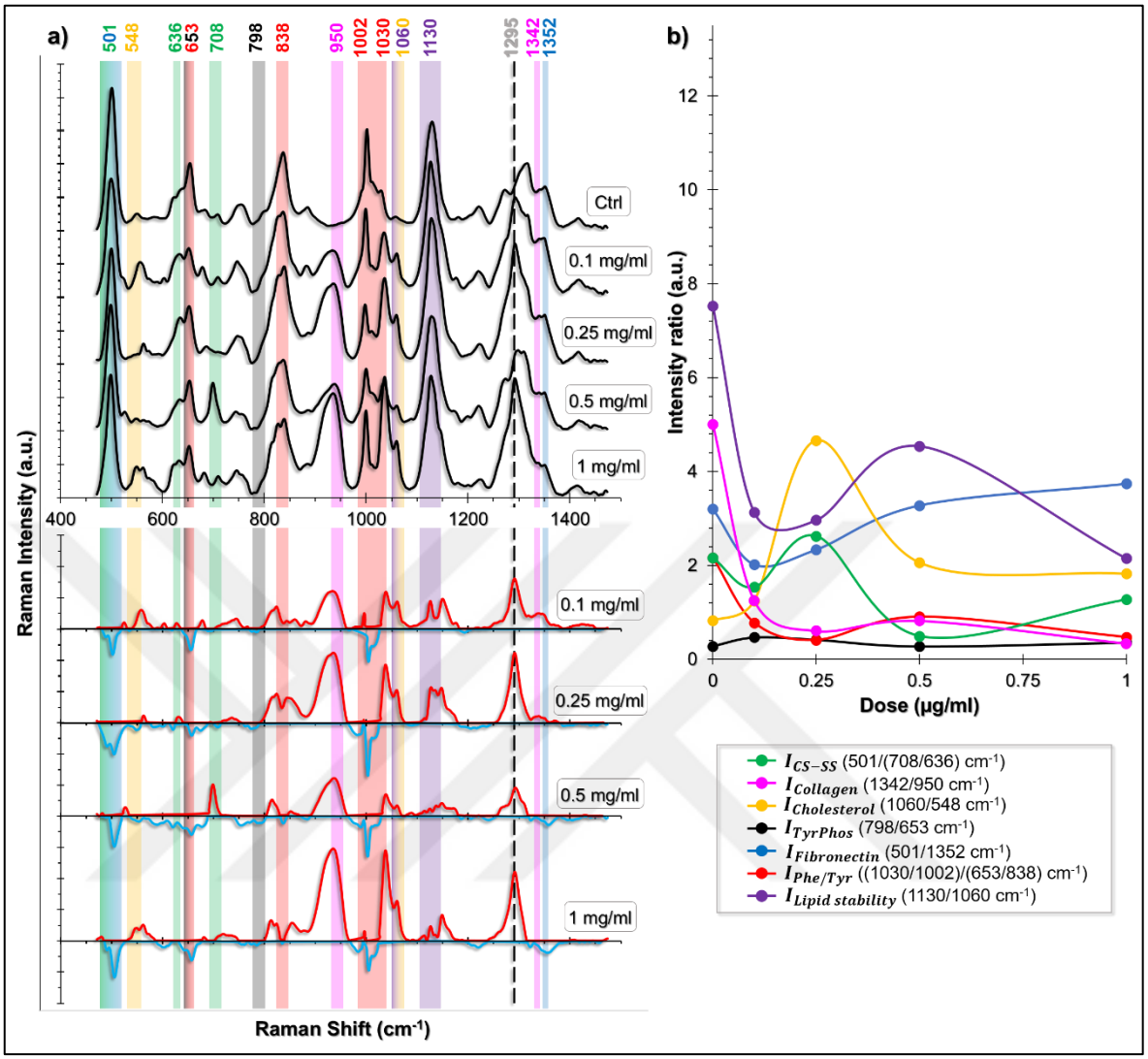

Figure 4.44. **(a)** SERS pattern of L929 cell line exposed to SWCNTs at increasing concentrations. In the lower panel, NM-exposed spectra were subtracted from the control spectrum to better visualize the spectral differences. The highlighted areas show the spectral peaks that were used in **(b)** intensity ratio calculations and the color code depicts the respective intensity ratio. The two peaks that were used in intensity ratio calculations were highlighted with those two colors. The peak belonging to SWCNTs was highlighted with a dashed line.

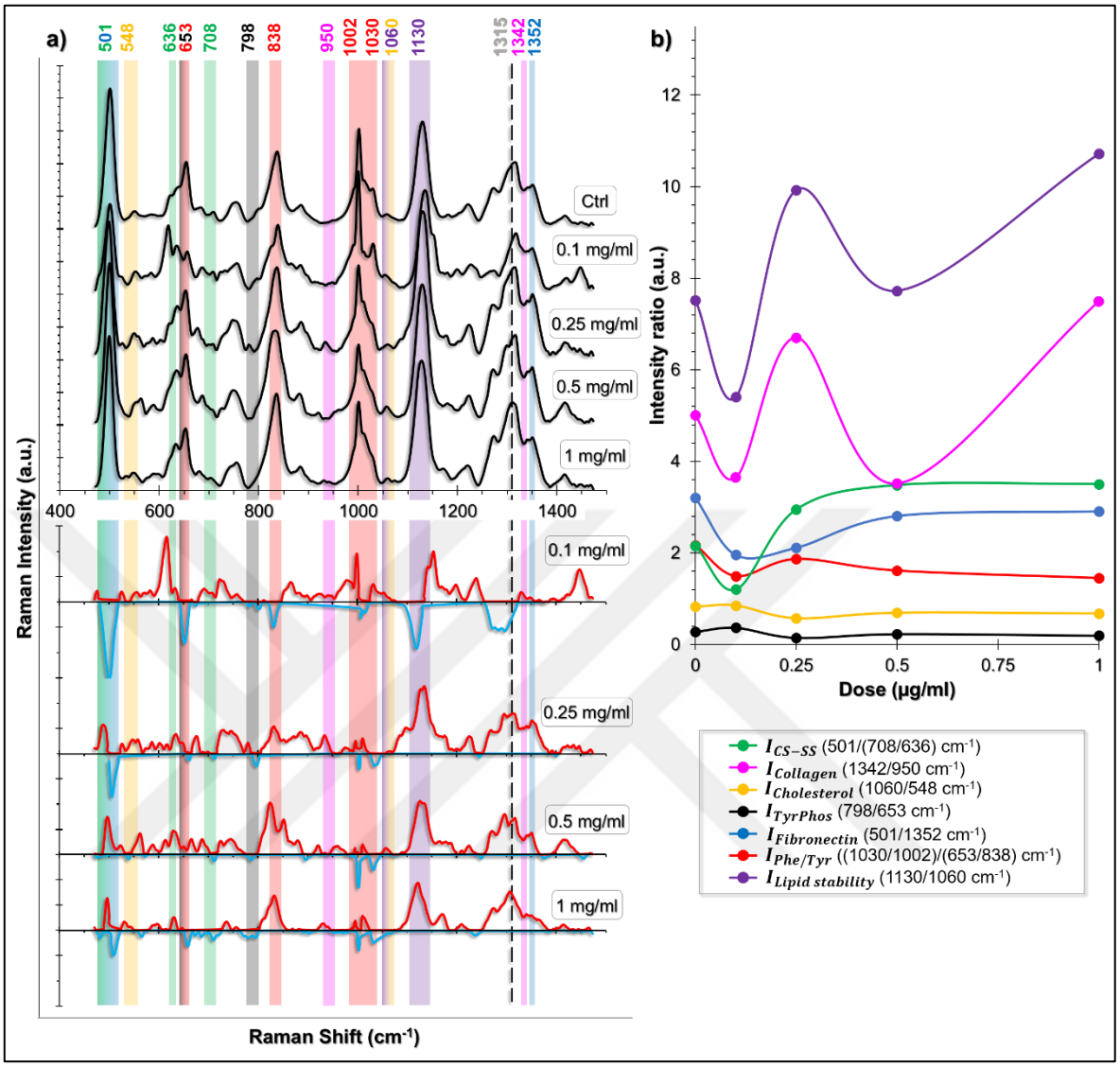

Figure 4.45. **(a)** SERS pattern of L929 cell line exposed to MWCNTs at increasing concentrations. In the lower panel, NM-exposed spectra were subtracted from the control spectrum to better visualize the spectral differences. The highlighted areas show the spectral peaks that were used in **(b)** intensity ratio calculations and the color code depicts the respective intensity ratio. The two peaks that were used in intensity ratio calculations were highlighted with those two colors. The peak belonging to MWCNTs was highlighted with a dashed line.

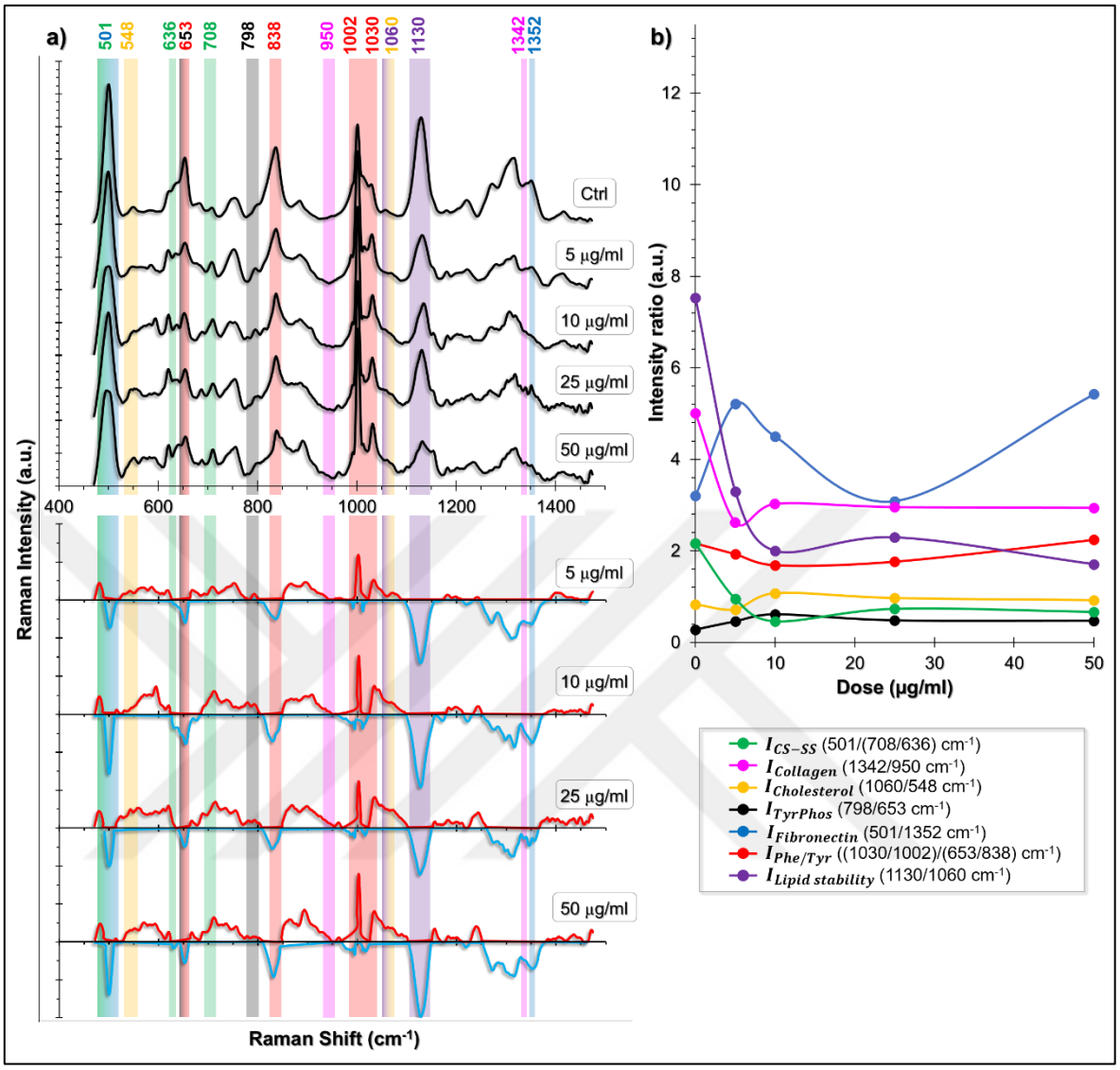

Figure 4.46. **(a)** SERS pattern of L929 cell line exposed to QDs at increasing concentrations. In the lower panel, NM-exposed spectra were subtracted from the control spectrum to better visualize the spectral differences. The highlighted areas show the spectral peaks that were used in **(b)** intensity ratio calculations and the color code depicts the respective intensity ratio. The two peaks that were used in intensity ratio calculations were highlighted with those two colors.

5. CONCLUSIONS AND OUTLOOK

The applicability of SERS in nanotoxicity assessment of living cells were demonstrated in the present work with promising observations. Moreover, two original research articles were published as outcomes that can be found in references [190], [191] as well as a review article on single-cell analysis by using AuNPs as SERS substrates [192]. Indeed, throughout the time span of this thesis work, from 2013 to 2017, several groups also reported the potential use of SERS as a toxicity detection method [193]–[195]. A study on nanotoxicity detection of polystyrene nanoparticles with Raman spectroscopy was also recently reported [196] and the topic seems to be trending more in the future. Those studies, however, relied more on multivariate statistical analyses to discriminate the treated and non-treated sample groups. In this study, an alternative approach was chosen; searching for spectral intensity ratios that would point out to important cellular stress markers such as inflammation, redox dynamics, lipid content- and ECM protein-related changes. The approach provided a clear comparison between cell lines as well as among increasing NM concentrations.

Prior to spectral analyses of NM-exposed cells, however, important points in experimental optimization were cleared out. The localization of the SERS substrates was one of these. AuNPs were mostly found in endolysosomal system unless the vesicles were ruptured or AuNPs leaked out from the vesicles. This meant that the spectral interpretation should have been made based on the possible content of endolysosomal vesicles such as membrane and ECM proteins that were to be recycled, and lipid content of vesicles.

With this observation, the second question that was answered was the extent of corona contribution to the spectral pattern. Corona-formed AuNPs were exposed to heat, trypsin and H_2O_2 in a cell-free environment. In addition to that, cells were ruptured upon AuNP exposure for 24 hours. The results obtained from these studies showed that the spectral changes were a combination of corona modifications and the changes in the microenvironment around the corona; meaning that NM-exposed cell spectra could successfully mirror the biochemical changes in cells.

Then, in the absence of NM-exposure, SERS spectra belonging to the four cell lines were compared and correlated to their well-known distinct features in the literature through

comparing seven spectral intensity ratios. The observations were in-line with the literature. Therefore, a cell-line dependent response could be monitored by the applied method.

The five NMs initiated distinct cellular responses at increasing NM concentrations. From the results, ZnO NPs were seen to be the most cytotoxic NM and the mechanism of nanotoxicity appeared to be mainly through lipid peroxidation leading to membrane deformations. QD nanotoxicity was observed to be of similar mechanism but inflammation induction was more pronounced. TiO_2 NPs initiated a mild oxidative stress that was overcome in most of the cell lines through their antioxidant activities. Even though the visual inspection of the cells upon NM exposure showed that the cells were affected, the results of WST-1 assays carried out with TiO_2 NPs and QDs were found to be false positive or negative due to their interaction with the assay components or light scattering properties, respectively. Therefore, SERS nanotoxicity detection was more powerful and provided more insight than this method for these NMs. Among the two CNTs, MWCNTs were less cytotoxic but caused an increase in fibronectin-related peaks, indicating the formation of stress fibers upon interaction with these NMs. Due to the observed background signals originating from SWCNTs themselves, spectral interpretation was made cautiously even though the rate of SWCNT signal contribution (continuos Raman) to the overall signal intensity was shown to be subtle. A Raman scattering-based SWCNT nanotoxicity evaluation report from 2009 have also shown similar results to the findings herein; significant changes in lipid-related peaks. Their results were also supported by an additional report from the same group where they acquired TEM images of cells upon SWCNT exposure and showed an increase in lamellar bodies in cells [197], [198]. Therefore, the increased cholesterol depletion rates might be relevant. Indeed, acquiring spectra from the high wavenumber region (between 2400-3800 cm^{-1}) could be beneficial to bypass the SWCNT interference in lipid-related peaks observed in this work [199]–[201].

In the scope of this thesis, some complementary experiments could be done and indeed these experiments can be suggested as future directions to the project. One of them was the isolation of endolysosomal vesicles from the cells for SERS analysis and their comparison to cellular spectra. Analyzing the endosomes by mass spectroscopy for vesicle contents could confirm the obtained results [202]. Similarly, lipid content changes, antioxidant capacity as well as ROS induction upon NM exposure of each test group could be detected. However, the ROS detection assay, DCFH-DA assay, would likely not be efficient because

the literature reports demonstrated that most of the NMs result in absorbance artefacts in this assay.

All in all, with the established protocol, it is possible to successfully assess nanotoxicity from a multidimensional perspective and more importantly in a fast, cheap, and simple way. Upon NM exposure step, the analysis takes about four to five hours including the data processing step of spectral acquisition from about 100 cells. Considering the time that would require to conduct several types of conventional cytotoxicity assays to obtain such multidimensional information, four to five hour duration is actually faster and less laborious. Because the obtained results are semi-quantitative, the method can also be used as a starting point in nanotoxicity investigations. Through checking the important cellular parameters such as lipid stability, inflammation induction or oxidative stress, further quantitative studies can be chosen accordingly, which can reduce the time, cost and effort spent on conducting various tests.

Moreover, the intensity ratios created herein can be applied to any other toxicity screening studies including drugs and other chemicals, of course with cautious evaluation of background spectra of the chemicals themselves. It is also possible to carry out comparative nanotoxicity experiments. As in the case for the two CNTs in this study, SWCNTs and MWCNTs, it was possible to point out the variations in toxic response when only the type of the CNT was different. Similarly, it is possible to investigate the effect of surface chemistry, size, shape and other physicochemical properties of NMs on the toxic outcome; for instance the effect of various sizes of the same NMs can be investigated.

REFERENCES

1. M. José-Yacamán, L. Rendón, J. Arenas, and M. C. S. Puche, Maya Blue Paint: An Ancient Nanostructured Material, *Science*, 273:223–225, 1996.

2. A. Ruivo, C. Gomes, A. Lima, M. L. Botelho, R. Melo, A. Belchior, and A. Pires de Matos, Gold Nanoparticles in Ancient and Contemporary Ruby Glass, *Journal of Cultural Heritage*, 9:134–137, 2008.

3. M. Reibold, N. Pätzke, A. A. Levin, W. Kochmann, I. P. Shakhverdova, P. Paufler, and D. C. Meyer, Structure of Several Historic Blades at Nanoscale, *Crystal Research and Technology*, 44:1139–1146, 2009.

4. S. Mahdihassan, Cinnabar-gold as the Best Alchemical Drug of Longevity, Called Makaradhwaja in India, *The American Journal of Chinese Medicine*, 13:93–108, 1985.

5. M. Faraday, The Bakerian Lecture: Experimental Relations of Gold (and Other Metals) to Light, *Philosophical Transactions of the Royal Society of London*, 147:145–181, 1857.

6. M.-C. Daniel and D. Astruc, Gold Nanoparticles: Assembly, Supramolecular Chemistry, Quantum-Size-Related Properties, and Applications Toward Biology, Catalysis, and Nanotechnology, *Chemical Reviews*, 104:293–346, 2004.

7. G. T. Beilby, The Effects of Heat and of Solvents on Thin Films of Metal, *Proceedings of the Royal Society of London*, 72:226–235, 1903.

8. J. C. M. Garnett, Colours in Metal Glasses and in Metallic Films, *Philosophical Transactions of the Royal Society of London A: Mathematical, Physical and Engineering Sciences*, 203:385–420, 1904.

9. T. Turner, Transparent Silver and Other Metallic Films, *Proceedings of the Royal Society of London. Series A*, 81:301–310, 1908.

10. R. P. Feynman, There's Plenty of Room at the Bottom, *Engineering and science*, 23:22–36, 1960.

11. C. Toumey, Plenty of Room, Plenty of History, *Nature Nanotechnology*, 4:783–784, 2009.

12. X. Gao, Y. Cui, R. M. Levenson, L. W. K. Chung, and S. Nie, In vivo Cancer Targeting and Imaging with Semiconductor Quantum Dots, *Nature Biotechnology*, 22:969–976, 2004.

13. W. Cai, D.-W. Shin, K. Chen, O. Gheysens, Q. Cao, S. X. Wang, S. S. Gambhir, and X. Chen, Peptide-Labeled Near-Infrared Quantum Dots for Imaging Tumor Vasculature in Living Subjects, *Nano Letters*, 6:669–676, 2006.

14. K. R. Carter, Nanofabrication: Past, Present and Future, *Journal of Materials Chemistry*, 21:14095–14096, 2011.

15. S. M. Amini, M. Gilaki, and M. Karchani, Safety of Nanotechnology in Food Industries, *Electronic Physician*, 6:962–968, 2014.

16. N. A. Singh, Nanotechnology Definitions, Research, Industry and Property Rights, in *Nanoscience in Food and Agriculture 1*, S. Ranjan, N. Dasgupta, and E. Lichtfouse, editors, Springer International Publishing, 43–64, 2016.

17. A. K. Hussein, Applications of Nanotechnology to Improve the Performance of Solar Collectors – Recent Advances and Overview, *Renewable and Sustainable Energy Reviews*, 62:767–792, 2016.

18. M. L. Etheridge, S. A. Campbell, A. G. Erdman, C. L. Haynes, S. M. Wolf, and J. McCullough, The Big Picture on Small Medicine: The State of Nanomedicine Products Approved for Use or in Clinical Trials, *Nanomedicine : nanotechnology, biology, and medicine*, 9:1–14, 2013.

19. K. J. Cash and H. A. Clark, Nanosensors and Nanomaterials for Monitoring Glucose in Diabetes, *Trends in molecular medicine*, 16:584–593, 2010.

20. A. Soloperto, G. Palazzolo, H. Tsushima, E. Chieregatti, M. Vassalli, and F. Difato, Laser Nano-Neurosurgery from Gentle Manipulation to Nano-Incision of Neuronal Cells and Scaffolds: An Advanced Neurotechnology Tool, *Frontiers in Neuroscience*, 10:101, 2016.

21. K. Donaldson, V. Stone, C. L. Tran, W. Kreyling, and P. J. A. Borm, Nanotoxicology, *Occupational and Environmental Medicine*, 61:727–728, 2004.

22. G. Oberdörster, A. Maynard, K. Donaldson, V. Castranova, J. Fitzpatrick, K. Ausman, J. Carter, B. Karn, W. Kreyling, D. Lai, S. Olin, N. Monteiro-Riviere, D. Warheit, H. Yang, and ILSI Research Foundation/Risk Science Institute Nanomaterial Toxicity Screening Working Group, Principles for Characterizing the Potential Human Health Effects from Exposure to Nanomaterials: Elements of a Screening Strategy, *Particle and Fibre Toxicology*, 2:8, 2005.

23. P. M. J. Bos, S. Gottardo, J. J. Scott-Fordsmand, M. van Tongeren, E. Semenzin, T. F. Fernandes, D. Hristozov, K. Hund-Rinke, N. Hunt, M.-A. Irfan, R. Landsiedel, W. J. G. M. Peijnenburg, A. Sánchez Jiménez, P. C. E. van Kesteren, and A. G. Oomen, The MARINA Risk Assessment Strategy: A Flexible Strategy for Efficient Information Collection and Risk Assessment of Nanomaterials, *International Journal of Environmental Research and Public Health*, 12:15007–15021, 2015.

24. O. M. Bondarenko, M. Heinlaan, M. Sihtmäe, A. Ivask, I. Kurvet, E. Joonas, A. Jemec, M. Mannerström, T. Heinonen, R. Rekulapelly, S. Singh, J. Zou, I. Pyykkö, D. Drobne, and A. Kahru, Multilaboratory Evaluation of 15 Bioassays for (Eco)toxicity Screening and Hazard Ranking of Engineered Nanomaterials: FP7 project NANOVALID, *Nanotoxicology*, 10:1229–1242, 2016.

25. J. Hastings, N. Jeliazkova, G. Owen, G. Tsiliki, C. R. Munteanu, C. Steinbeck, and E. Willighagen, eNanoMapper: Harnessing Ontologies to Enable Data Integration for Nanomaterial Risk Assessment, *Journal of Biomedical Semantics*, 6:10, 2015.

26. J. Jiang, G. Oberdörster, and P. Biswas, Characterization of size, surface charge, and agglomeration state of nanoparticle dispersions for toxicological studies, *Journal of Nanoparticle Research*, 11:77–89, 2009.

27. S. Lanone, F. Rogerieux, J. Geys, A. Dupont, E. Maillot-Marechal, J. Boczkowski, G. Lacroix, and P. Hoet, Comparative Toxicity of 24 Manufactured Nanoparticles in Human Alveolar Epithelial and Macrophage Cell Lines, *Particle and Fibre Toxicology*, 6:14, 2009.

28. T. Chen, J. Hu, C. Chen, J. Pu, X. Cui, and G. Jia, Cardiovascular Effects of Pulmonary Exposure to Titanium Dioxide Nanoparticles in ApoE Knockout Mice, *Journal of Nanoscience and Nanotechnology*, 13:3214–3222, 2013.

29. Q. Zeng, D. Shao, W. Ji, J. Li, L. Chen, and J. Song, The Nanotoxicity Investigation of Optical Nanoparticles to Cultured Cells In Vitro, *Toxicology Reports*, 1:137–144, 2014.

30. C. A. Poland, R. Duffin, I. Kinloch, A. Maynard, W. A. H. Wallace, A. Seaton, V. Stone, S. Brown, W. MacNee, and K. Donaldson, Carbon Nanotubes Introduced into the Abdominal Cavity of Mice Show Asbestos-Like Pathogenicity in a Pilot Study, *Nature Nanotechnology*, 3:423–428, 2008.

31. H. Yin, H. P. Too, and G. M. Chow, The Effects of Particle Size and Surface Coating on the Cytotoxicity of Nickel Ferrite, *Biomaterials*, 26:5818–5826, 2005.

32. V. Iswarya, M. Bhuvaneshwari, S. A. Alex, S. Iyer, G. Chaudhuri, P. T. Chandrasekaran, G. M. Bhalerao, S. Chakravarty, A. M. Raichur, N. Chandrasekaran, and A. Mukherjee, Combined Toxicity of Two Crystalline Phases (Anatase and Rutile) of Titania Nanoparticles Towards Freshwater Microalgae: Chlorella sp, *Aquatic Toxicology*, 161:154–169, 2015.

33. R. Y. Prasad, K. Wallace, K. M. Daniel, A. H. Tennant, R. M. Zucker, J. Strickland, K. Dreher, A. D. Kligerman, C. F. Blackman, and D. M. DeMarini, Effect of Treatment Media on the Agglomeration of Titanium Dioxide Nanoparticles: Impact on Genotoxicity, Cellular Interaction, and Cell Cycle, *ACS Nano*, 7:1929–1942, 2013.

34. N. Tripathy, T.-K. Hong, K.-T. Ha, H.-S. Jeong, and Y.-B. Hahn, Effect of ZnO nanoparticles aggregation on the toxicity in RAW 264.7 murine macrophage, *Journal of Hazardous Materials*, 270:110–117, 2014.

35. A. K. Suresh, D. A. Pelletier, W. Wang, J. L. Morrell-Falvey, B. Gu, and M. J. Doktycz, Cytotoxicity Induced by Engineered Silver Nanocrystallites Is Dependent on Surface Coatings and Cell Types, *Langmuir*, 28:2727–2735, 2012.

36. Y.-S. Lin and C. L. Haynes, Impacts of Mesoporous Silica Nanoparticle Size, Pore Ordering, and Pore Integrity on Hemolytic Activity, *Journal of the American Chemical Society*, 132:4834–4842, 2010.

37. A. M. El Badawy, R. G. Silva, B. Morris, K. G. Scheckel, M. T. Suidan, and T. M. Tolaymat, Surface Charge-Dependent Toxicity of Silver Nanoparticles, *Environmental Science & Technology*, 45:283–287, 2011.

38. C. Shan, W. Zhao, X. L. Lu, D. J. O'Brien, Y. Li, Z. Cao, A. L. Elias, R. Cruz-Silva, M. Terrones, B. Wei, and J. Suhr, Three-Dimensional Nitrogen-Doped Multiwall Carbon Nanotube Sponges with Tunable Properties, *Nano Letters*, 13:5514–5520, 2013.

39. B. B. Manshian, U. Himmelreich, and S. J. Soenen, Standard Cellular Testing Conditions Generate an Exaggerated Nanoparticle Cytotoxicity Profile, *Chemical Research in Toxicology*, 2:595-603, 2016.

40. D. Wingett, P. Louka, C. B. Anders, J. Zhang, and A. Punnoose, A role of ZnO Nanoparticle Electrostatic Properties in Cancer Cell Cytotoxicity, *Nanotechnology, Science and Applications*, 9:29–45, 2016.

41. B. B. Manshian, S. J. Soenen, A. Al-Ali, A. Brown, N. Hondow, J. Wills, G. J. S. Jenkins, and S. H. Doak, Cell Type-Dependent Changes in CdSe/ZnS Quantum Dot Uptake and Toxic Endpoints, *Toxicological Sciences: An Official Journal of the Society of Toxicology*, 144:246–258, 2015.

42. N. Nafee, M. Schneider, U. F. Schaefer, and C.-M. Lehr, Relevance of the Colloidal Stability of Chitosan/PLGA Nanoparticles on Their Cytotoxicity Profile, *International Journal of Pharmaceutics*, 381:130–139, 2009.

43. A. Casey, E. Herzog, F. M. Lyng, H. J. Byrne, G. Chambers, and M. Davoren, Single Walled Carbon Nanotubes Induce Indirect Cytotoxicity by Medium Depletion in A549 Lung Cells, *Toxicology Letters*, 179:78–84, 2008.

44. M. Geiser, B. Rothen-Rutishauser, N. Kapp, S. Schürch, W. Kreyling, H. Schulz, M. Semmler, V. I. Hof, J. Heyder, and P. Gehr, Ultrafine Particles Cross Cellular

Membranes by Nonphagocytic Mechanisms in Lungs and in Cultured Cells, *Environmental Health Perspectives*, 113:1555–1560, 2005.

45. S. K. Banerji and M. A. Hayes, Examination of Nonendocytotic Bulk Transport of Nanoparticles Across Phospholipid Membranes, *Langmuir*, 23:3305–3313, 2007.

46. S. Barua and S. Mitragotri, Challenges associated with Penetration of Nanoparticles across Cell and Tissue Barriers: A Review of Current Status and Future Prospects, *Nano today*, 9:223–243, 2014.

47. X. Hu, D. Li, Y. Gao, L. Mu, and Q. Zhou, Knowledge Gaps Between Nanotoxicological Research and Nanomaterial Safety, *Environment International*, 94:8–23, 2016.

48. S. Tenzer, D. Docter, S. Rosfa, A. Wlodarski, J. Kuharev, A. Rekik, S. K. Knauer, C. Bantz, T. Nawroth, C. Bier, J. Sirirattanapan, W. Mann, L. Treuel, R. Zellner, M. Maskos, H. Schild, and R. H. Stauber, Nanoparticle Size is a Critical Physicochemical Determinant of the Human Blood Plasma Corona: A Comprehensive Quantitative Proteomic Analysis, *ACS Nano*, 5:7155–7167, 2011.

49. B. H. Rihn and O. Joubert, Comment on "Protein Corona Fingerprinting Predicts the Cellular Interaction of Gold and Silver Nanoparticles," *ACS Nano*, 9:5634–5635, 2015.

50. S. Wan, P. M. Kelly, E. Mahon, H. Stöckmann, P. M. Rudd, F. Caruso, K. A. Dawson, Y. Yan, and M. P. Monopoli, The "Sweet" Side of the Protein Corona: Effects of Glycosylation on Nanoparticle–Cell Interactions, *ACS Nano*, 9:2157–2166, 2015.

51. J. C. Y. Kah, C. Grabinski, E. Untener, C. Garrett, J. Chen, D. Zhu, S. M. Hussain, and K. Hamad-Schifferli, Protein Coronas on Gold Nanorods Passivated with Amphiphilic Ligands Affect Cytotoxicity and Cellular Response to Penicillin/Streptomycin, *ACS Nano*, 8:4608–4620, 2014.

52. D. Walczyk, F. B. Bombelli, M. P. Monopoli, I. Lynch, and K. A. Dawson, What the Cell "Sees" in Bionanoscience, *Journal of the American Chemical Society*, 132:5761–5768, 2010.

53. C. C. Fleischer and C. K. Payne, Nanoparticle–Cell Interactions: Molecular Structure of the Protein Corona and Cellular Outcomes, *Accounts of Chemical Research*, 47:2651–2659, 2014.

54. I. Dewald, O. Isakin, J. Schubert, T. Kraus, and M. Chanana, Protein Identity and Environmental Parameters Determine the Final Physicochemical Properties of Protein-Coated Metal Nanoparticles, *The Journal of Physical Chemistry C*, 119:25482–25492, 2015.

55. I. Lynch, A. Salvati, and K. A. Dawson, Protein-Nanoparticle Interactions: What Does the Cell See?, *Nature Nanotechnology*, 4:546–547, 2009.

56. M. M. Yallapu, N. Chauhan, S. F. Othman, V. Khalilzad-Sharghi, M. C. Ebeling, S. Khan, M. Jaggi, and S. C. Chauhan, Implications of Protein Corona on Physico-Chemical and Biological Properties of Magnetic Nanoparticles, *Biomaterials*, 46:1–12, 2015.

57. H. Kettiger, A. Schipanski, P. Wick, and J. Huwyler, Engineered Nanomaterial Uptake and Tissue Distribution: From Cell to Organism, *International Journal of Nanomedicine*, 8:3255–3269, 2013.

58. W. Rima, L. Sancey, M.-T. Aloy, E. Armandy, G. B. Alcantara, T. Epicier, A. Malchère, L. Joly-Pottuz, P. Mowat, F. Lux, O. Tillement, B. Burdin, A. Rivoire, C. Boulé, I. Anselme-Bertrand, J. Pourchez, M. Cottier, S. Roux, C. Rodriguez-Lafrasse, and P. Perriat, Internalization Pathways into cancer cells of Gadolinium-Based Radiosensitizing Nanoparticles, *Biomaterials*, 34:181–195, 2013.

59. T. J. Raub and K. L. Audus, Adsorptive Endocytosis and Membrane Recycling by Cultured Primary Bovine Brain Microvessel Endothelial Cell Monolayers, *Journal of Cell Science*, 97 (Pt 1):127–138, 1990.

60. B. M. Pearse, Clathrin: A Unique Protein Associated with Intracellular Transfer of Membrane by Coated Vesicles, *Proceedings of the National Academy of Sciences of the United States of America*, 73:1255–1259, 1976.

61. J. E. Schnitzer, J. Liu, and P. Oh, Endothelial Caveolae Have the Molecular Transport Machinery for Vesicle Budding, Docking, and Fusion Including VAMP, NSF, SNAP, Annexins, and GTPases, *Journal of Biological Chemistry*, 270:14399–14404, 1995.

62. P. Oh, D. P. McIntosh, and J. E. Schnitzer, Dynamin at the Neck of Caveolae Mediates Their Budding to Form Transport Vesicles by GTP-driven Fission from the Plasma Membrane of Endothelium, *The Journal of Cell Biology*, 141:101–114, 1998.

63. P. U. Le, G. Guay, Y. Altschuler, and I. R. Nabi, Caveolin-1 is a Negative Regulator of Caveolae-Mediated Endocytosis to the Endoplasmic Reticulum, *The Journal of Biological Chemistry*, 277:3371–3379, 2002.

64. A. Hayer, M. Stoeber, D. Ritz, S. Engel, H. H. Meyer, and A. Helenius, Caveolin-1 is ubiquitinated and targeted to intralumenal vesicles in Endolysosomes for Degradation, *The Journal of Cell Biology*, 191:615–629, 2010.

65. L. Pelkmans, T. Bürli, M. Zerial, and A. Helenius, Caveolin-Stabilized Membrane Domains as Multifunctional Transport and Sorting Devices in Endocytic Membrane Traffic, *Cell*, 118:767–780, 2004.

66. J. Rejman, V. Oberle, I. S. Zuhorn, and D. Hoekstra, Size-Dependent Internalization of Particles via the Pathways of Clathrin- and Caveolae-Mediated Endocytosis, *Biochemical Journal*, 377:159–169, 2004.

67. R. Montesano, J. Roth, A. Robert, and L. Orci, Non-Coated Membrane Invaginations are Involved in Binding and Internalization of Cholera and Tetanus Toxins, *Nature*, 296:651–653, 1982.

68. H. Radhakrishna and J. G. Donaldson, ADP-Ribosylation Factor 6 Regulates a Novel Plasma Membrane Recycling Pathway, *The Journal of Cell Biology*, 139:49–61, 1997.

69. C. Lamaze, A. Dujeancourt, T. Baba, C. G. Lo, A. Benmerah, and A. Dautry-Varsat, Interleukin 2 Receptors and Detergent-Resistant Membrane Domains Define a Clathrin-Independent Endocytic Pathway, *Molecular Cell*, 7:661–671, 2001.

70. D. R. Nogueira, M. Mitjans, C. M. B. Rolim, and M. P. Vinardell, Mechanisms Underlying Cytotoxicity Induced by Engineered Nanomaterials: A Review of In Vitro Studies, *Nanomaterials*, 4:454–484, 2014.

71. A. B. Djurišić, Y. H. Leung, A. M. C. Ng, X. Y. Xu, P. K. H. Lee, N. Degger, and R. S. S. Wu, Toxicity of Metal Oxide Nanoparticles: Mechanisms, Characterization, and Avoiding Experimental Artefacts, *Small*, 11:26–44, 2015.

72. S. Bakand and A. Hayes, Toxicological Considerations, Toxicity Assessment, and Risk Management of Inhaled Nanoparticles, *International Journal of Molecular Sciences*, 17:929, 2016.

73. R. K. Shukla, V. Sharma, A. K. Pandey, S. Singh, S. Sultana, and A. Dhawan, ROS-Mediated Genotoxicity Induced by Titanium Dioxide Nanoparticles in Human Epidermal Cells, *Toxicology in vitro: an international journal published in association with BIBRA*, 25:231–241, 2011.

74. A. A. Shvedova, E. R. Kisin, R. Mercer, A. R. Murray, V. J. Johnson, A. I. Potapovich, Y. Y. Tyurina, O. Gorelik, S. Arepalli, D. Schwegler-Berry, A. F. Hubbs, J. Antonini, D. E. Evans, B.-K. Ku, D. Ramsey, A. Maynard, V. E. Kagan, V. Castranova, and P. Baron, Unusual Inflammatory and Fibrogenic Pulmonary Responses to Single-Walled Carbon Nanotubes in Mice, *American Journal of Physiology. Lung Cellular and Molecular Physiology*, 289:698–708, 2005.

75. A. Nel, T. Xia, L. Mädler, and N. Li, Toxic Potential of Materials at the Nanolevel, *Science (New York, N.Y.)*, 311:622–627, 2006.

76. P. V. Asharani, Y. Lianwu, Z. Gong, and S. Valiyaveettil, Comparison of the Toxicity of Silver, Gold and Platinum Nanoparticles in Developing Zebrafish Embryos, *Nanotoxicology*, 5:43–54, 2011.

77. S. Barillet, M.-L. Jugan, M. Laye, Y. Leconte, N. Herlin-Boime, C. Reynaud, and M. Carrière, In Vitro Evaluation of SiC Nanoparticles Impact on A549 Pulmonary Cells: Cyto-, Genotoxicity and Oxidative Stress, *Toxicology Letters*, 198:324–330, 2010.

78. Z. Magdolenova, A. Collins, A. Kumar, A. Dhawan, V. Stone, and M. Dusinska, Mechanisms of genotoxicity. A Review of In Vitro and In Vivo Studies with Engineered Nanoparticles, *Nanotoxicology*, 8:233–278, 2014.

79. P. P. Fu, Q. Xia, H.-M. Hwang, P. C. Ray, and H. Yu, Mechanisms of Nanotoxicity: Generation of Reactive Oxygen Species, *Journal of Food and Drug Analysis*, 22:64–75, 2014.

80. S. T. Stern, P. P. Adiseshaiah, and R. M. Crist, Autophagy and Lysosomal Dysfunction as Emerging Mechanisms of Nanomaterial Toxicity, *Particle and Fibre Toxicology*, 9:20, 2012.

81. R. Guadagnini, B. Halamoda Kenzaoui, L. Walker, G. Pojana, Z. Magdolenova, D. Bilanicova, M. Saunders, L. Juillerat-Jeanneret, A. Marcomini, A. Huk, M. Dusinska, L. M. Fjellsbø, F. Marano, and S. Boland, Toxicity Screenings of Nanomaterials: Challenges due to Interference with Assay Processes and Components of Classic In Vitro Tests, *Nanotoxicology*, 9:13–24, 2013.

82. A. Casey, E. Herzog, M. Davoren, F. M. Lyng, H. J. Byrne, and G. Chambers, Spectroscopic Analysis Confirms the Interactions between Single Walled Carbon Nanotubes and Various Dyes Commonly Used to Assess Cytotoxicity, *Carbon*, 45:1425–1432, 2007.

83. A. Kroll, M. H. Pillukat, D. Hahn, and J. Schnekenburger, Interference of Engineered Nanoparticles with In Vitro Toxicity Assays, *Archives of Toxicology*, 86:1123–1136, 2012.

84. J. Tournebize, A. Sapin-Minet, G. Bartosz, P. Leroy, and A. Boudier, Pitfalls of Assays Devoted to Evaluation of Oxidative Stress Induced by Inorganic Nanoparticles, *Talanta*, 116:753–763, 2013.

85. A. R. Lupu and T. Popescu, The Noncellular Reduction of MTT Tetrazolium Salt by TiO_2 Nanoparticles and its Implications for Cytotoxicity Assays, *Toxicology in vitro: an international journal published in association with BIBRA*, 27:1445–1450, 2013.

86. K. J. Ong, T. J. MacCormack, R. J. Clark, J. D. Ede, V. A. Ortega, L. C. Felix, M. K. M. Dang, G. Ma, H. Fenniri, J. G. C. Veinot, and G. G. Goss, Widespread Nanoparticle-Assay Interference: Implications for Nanotoxicity Testing, *PLoS ONE*, 9:90650, 2014.

87. T. J. MacCormack, R. J. Clark, M. K. M. Dang, G. Ma, J. A. Kelly, J. G. C. Veinot, and G. G. Goss, Inhibition of Enzyme Activity by Nanomaterials: Potential Mechanisms and Implications for Nanotoxicity Testing, *Nanotoxicology*, 6:514–525, 2012.

88. O. Stueker, V. A. Ortega, G. G. Goss, and M. Stepanova, Understanding Interactions of Functionalized Nanoparticles with Proteins: A Case Study on Lactate Dehydrogenase, *Small*, 10:2006–2021, 2014.

89. M. Simkó, D. Nosske, and W. G. Kreyling, Metrics, Dose, and Dose Concept: The Need for a Proper Dose Concept in the Risk Assessment of Nanoparticles, *International Journal of Environmental Research and Public Health*, 11:4026–4048, 2014.

90. J. A. Shatkin, K. J. Ong, C. Beaudrie, A. J. Clippinger, C. O. Hendren, L. T. Haber, M. Hill, P. Holden, A. J. Kennedy, B. Kim, M. MacDonell, C. M. Powers, M. Sharma, L. Sheremeta, V. Stone, Y. Sultan, A. Turley, and R. H. White, Advancing Risk Analysis for Nanoscale Materials: Report from an International Workshop on the Role of Alternative Testing Strategies for Advancement, *Risk Analysis: An Official Publication of the Society for Risk Analysis*, 36:1520–1537, 2016.

91. T. T. Schug, A. F. Johnson, D. M. Balshaw, S. Garantziotis, N. J. Walker, C. Weis, S. S. Nadadur, and L. S. Birnbaum, ONE Nano: NIEHS's Strategic Initiative on the Health and Safety Effects of Engineered Nanomaterials, *Environmental Health Perspectives*, 121:410–414, 2013.

92. A. G. Oomen, P. M. J. Bos, T. F. Fernandes, K. Hund-Rinke, D. Boraschi, H. J. Byrne, K. Aschberger, S. Gottardo, F. von der Kammer, D. Kühnel, D. Hristozov, A. Marcomini, L. Migliore, J. Scott-Fordsmand, P. Wick, and R. Landsiedel, Concern-driven integrated approaches to nanomaterial testing and Assessment-Report of the NanoSafety Cluster Working Group 10, *Nanotoxicology*, 8:334–348, 2014.

93. A. E. Nel, E. Nasser, H. Godwin, D. Avery, T. Bahadori, L. Bergeson, E. Beryt, J. C. Bonner, D. Boverhof, J. Carter, V. Castranova, J. R. DeShazo, S. M. Hussain, A. B. Kane, F. Klaessig, E. Kuempel, M. Lafranconi, R. Landsiedel, T. Malloy, M. B. Miller, J. Morris, K. Moss, G. Oberdorster, K. Pinkerton, R. C. Pleus, J. A. Shatkin, R. Thomas, T. Tolaymat, A. Wang, and J. Wong, A Multi-Stakeholder Perspective on the Use of Alternative Test Strategies for Nanomaterial Safety Assessment, *ACS nano*, 7:6422–6433, 2013.

94. A. K. Pal, I. Aalaei, S. Gadde, P. Gaines, D. Schmidt, P. Demokritou, and D. Bello, High Resolution Characterization of Engineered Nanomaterial Dispersions in Complex Media Using Tunable Resistive Pulse Sensing Technology, *ACS Nano*, 8:9003–9015, 2014.

95. A. J. Clippinger, A. Ahluwalia, D. Allen, J. C. Bonner, W. Casey, V. Castranova, R. M. David, S. Halappanavar, J. A. Hotchkiss, A. M. Jarabek, M. Maier, W. Polk, B. Rothen-Rutishauser, C. M. Sayes, P. Sayre, M. Sharma, and V. Stone, Expert Consensus on an In Vitro Approach to Assess Pulmonary Fibrogenic Potential of Aerosolized Nanomaterials, *Archives of Toxicology*, 90:1769–1783, 2016.

96. R. L. M. Robinson, I. Lynch, W. Peijnenburg, J. Rumble, F. Klaessig, C. Marquardt, H. Rauscher, T. Puzyn, R. Purian, C. Åberg, S. Karcher, H. Vriens, P. Hoet, M. D. Hoover, C. O. Hendren, and S. L. Harper, How Should the Completeness and Quality of Curated Nanomaterial Data be Evaluated?, 8:9919–9943, 2016.

97. R. Landsiedel, L. Ma-Hock, K. Wiench, W. Wohlleben, and U. G. Sauer, Safety Assessment of Nanomaterials Using an Advanced Decision-Making Framework, the DF4nanoGrouping, *Journal of Nanoparticle Research: An Interdisciplinary Forum for Nanoscale Science and Technology*, 19:171, 2017.

98. L. Kong, S. Tuomela, L. Hahne, H. Ahlfors, O. Yli-Harja, B. Fadeel, R. Lahesmaa, and R. Autio, NanoMiner - Integrative Human Transcriptomics Data Resource for Nanoparticle Research, *PloS One*, 8:68414, 2013.

99. D. A. Winkler, Recent Advances, and Unresolved Issues, in The Application of Computational Modelling to The Prediction of the Biological Effects of Nanomaterials, *Toxicology and Applied Pharmacology*, 299:96–100, 2016.

100. C. C. Zimmer, Y. X. Liu, J. T. Morgan, G. Yang, K.-H. Wang, I. M. Kennedy, A. I. Barakat, and G. Liu, New Approach to Investigate the Cytotoxicity of Nanomaterials Using Single Cell Mechanics, *The Journal of Physical Chemistry. B*, 118:1246–1255, 2014.

101. C. Riebeling, M. Wiemann, J. Schnekenburger, T. A. J. Kuhlbusch, W. Wohlleben, A. Luch, and A. Haase, A Redox Proteomics Approach to Investigate the Mode of Action of Nanomaterials, *Toxicology and Applied Pharmacology*, 299:24–29, 2016.

102. Z. Ke, Z. Yu, and Q. Huang, Assessment of Damage of Glutathione by Glow Discharge Plasma at the Gas–Solution Interface through Raman Spectroscopy, *Plasma Processes and Polymers*, 10:181–188, 2013.

103. J.-A. Sergent, V. Paget, and S. Chevillard, Toxicity and Genotoxicity of Nano-SiO2 on Human Epithelial Intestinal HT-29 Cell Line, *The Annals of Occupational Hygiene*, 56:622–630, 2012.

104. A. R. Collins, B. Annangi, L. Rubio, R. Marcos, M. Dorn, C. Merker, I. Estrela- Lopis, M. R. Cimpan, M. Ibrahim, E. Cimpan, M. Ostermann, A. Sauter, N. E. Yamani, S. Shaposhnikov, S. Chevillard, V. Paget, R. Grall, J. Delic, F. G. de- Cerio, B. Suarez-Merino, V. Fessard, K. N. Hogeveen, L. M. Fjellsbø, E. R. Pran, T. Brzicova, J. Topinka, M. J. Silva, P. E. Leite, A. R. Ribeiro, J. M. Granjeiro, R. Grafström, A. Prina- Mello, and M. Dusinska, High Throughput Toxicity Screening and Intracellular Detection of Nanomaterials, *Wiley Interdisciplinary Reviews. Nanomedicine and Nanobiotechnology*, 9:1413, 2017.

105. H. Schulz, G. Özkan, M. Baranska, H. Krüger, and M. Özcan, Characterisation of Essential Oil Plants from Turkey by IR and Raman Spectroscopy, *Vibrational Spectroscopy*, 39:249–256, 2005.

106. L. Bokobza, Near Infrared Spectroscopy, *Journal of Near Infrared Spectroscopy*, 6:3–17, 1998.

107. C. Pasquini, Near Infrared Spectroscopy: Fundamentals, Practical Aspects and Analytical Applications, *Journal of the Brazilian Chemical Society*, 14:198–219, 2003.

108. R. Chang, *Physical Chemistry for the Biosciences*. University Science Books, 2005.

109. N. Colthup, *Introduction to Infrared and Raman Spectroscopy*. Elsevier, 2012.

110. E. B. Wilson, J. C. Decius, and P. C. Cross, *Molecular Vibrations: The Theory of Infrared and Raman Vibrational Spectra*. Courier Corporation, 2012.

111. D. N. Sathyanarayana, *Vibrational Spectroscopy: Theory and Applications*. New Age International, 2015.

112. J. Coates, Interpretation of Infrared Spectra, a Practical Approach, *Encyclopedia of analytical chemistry*, 2000.

113. E. Smith and G. Dent, *Modern Raman Spectroscopy: A Practical Approach*. John Wiley & Sons, 2013.

114. Z. Li, M. J. Deen, S. Kumar, and P. R. Selvaganapathy, Raman Spectroscopy for In-Line Water Quality Monitoring—Instrumentation and Potential, *Sensors*, 14:17275–17303, 2014.

115. C. Xie, M. A. Dinno, and Y. Li, Near-Infrared Raman spectroscopy of Single Optically Trapped Biological Cells, *Optics Letters*, 27:249–251, 2002.

116. C. Xie, D. Chen, and Y. Li, Raman sorting and identification of Single Living Micro-Organisms with Optical Tweezers, *Optics Letters*, 30:1800–1802, 2005.

117. A. Zumbusch, G. R. Holtom, and X. S. Xie, Three-Dimensional Vibrational Imaging by Coherent Anti-Stokes Raman Scattering, *Physical Review Letters*, 82:4142–4145, 1999.

118. C. W. Freudiger, W. Min, B. G. Saar, S. Lu, G. R. Holtom, C. He, J. C. Tsai, J. X. Kang, and X. S. Xie, Label-Free Biomedical Imaging with High Sensitivity by Stimulated Raman Scattering Microscopy, *Science*, 322:1857–1861, 2008.

119. P. Matousek, I. P. Clark, E. R. C. Draper, M. D. Morris, A. E. Goodship, N. Everall, M. Towrie, W. F. Finney, and A. W. Parker, Subsurface probing in Diffusely Scattering Media Using Spatially Offset Raman Spectroscopy, *Applied Spectroscopy*, 59:393–400, 2005.

120. P. Geladi, D. MacDougall, and H. Martens, Linearization and Scatter-Correction for Near-Infrared Reflectance Spectra of Meat, *Applied Spectroscopy*, 39:491–500, 1985.

121. A. Aina, M. D. Hargreaves, P. Matousek, and J. C. Burley, Transmission Raman Spectroscopy as a Tool for Quantifying Polymorphic Content of Pharmaceutical Formulations, *The Analyst*, 135:2328–2333, 2010.

122. M. Minsky, Microscopy apparatus, 1961.

123. M. Fleischmann, P. J. Hendra, and A. J. McQuillan, Raman Spectra of Pyridine Adsorbed at a Silver Electrode, *Chemical Physics Letters*, 26:163–166, 1974.

124. D. L. Jeanmaire and R. P. Van Duyne, Surface Raman Spectroelectrochemistry, *Journal of Electroanalytical Chemistry and Interfacial Electrochemistry*, 84:1–20, 1977.

125. M. G. Albrecht and J. A. Creighton, Anomalously Intense Raman Spectra of Pyridine at a Silver Electrode, *Journal of the American Chemical Society*, 99:5215–5217, 1977.

126. R. M. Stöckle, Y. D. Suh, V. Deckert, and R. Zenobi, Nanoscale Chemical Analysis by Tip-Enhanced Raman Spectroscopy, *Chemical Physics Letters*, 318:131–136, 2000.

127. A. A. Stacy and R. P. Van Duyne, Surface Enhanced Raman and Resonance Raman Spectroscopy in a Non-Aqueous Electrochemical Environment: Tris(2,2′-bipyridine)ruthenium(II) Adsorbed on Silver From Acetonitrile, *Chemical Physics Letters*, 102:365–370, 1983.

128. C. L. Haynes, C. R. Yonzon, X. Zhang, and R. P. Van Duyne, Surface-Enhanced Raman Sensors: Early History and the Development of Sensors for Quantitative Biowarfare Agent and Glucose Detection, *Journal of Raman Spectroscopy*, 36:471–484, 2005.

129. R. P. V. Duyne, *Applications of Raman Spectroscopy in Electrochemistry*, *Le Journal de Physique Colloques*, 38:239–252, 1977.

130. Zhao, L. Jensen, and G. C. Schatz, Pyridine−Ag20 Cluster: A Model System for Studying Surface-Enhanced Raman Scattering, *Journal of the American Chemical Society*, 128:2911–2919, 2006.

131. P. Kambhampati, C. M. Child, M. C. Foster, and A. Campion, On the Chemical Mechanism of Surface Enhanced Raman Scattering: Experiment and Theory, *The Journal of Chemical Physics*, 108:5013–5026, 1998.

132. J. R. Lombardi and R. L. Birke, A Unified Approach to Surface-Enhanced Raman Spectroscopy, *The Journal of Physical Chemistry C*, 112:5605–5617, 2008.

133. S. M. Morton, E. Ewusi-Annan, and L. Jensen, Controlling the Non-Resonant Chemical Mechanism of SERS Using a Molecular Photoswitch, *Physical chemistry chemical physics: PCCP*, 11:7424–7429, 2009.

134. B. Sharma, R. R. Frontiera, A.-I. Henry, E. Ringe, and R. P. Van Duyne, SERS: Materials, Applications, and the Future, *Materials Today*, 15:16–25, 2012.

135. K. Ock, W. I. Jeon, E. O. Ganbold, M. Kim, J. Park, J. H. Seo, K. Cho, S.-W. Joo, and S. Y. Lee, Real-Time Monitoring of Glutathione-Triggered Thiopurine Anticancer Drug Release in Live Cells Investigated by Surface-Enhanced Raman Scattering, *Analytical Chemistry*, 84:2172–2178, 2012.

136. A. Sujith, T. Itoh, H. Abe, K. Yoshida, M. S. Kiran, V. Biju, and M. Ishikawa, Imaging the Cell Wall of Living Single Yeast Cells Using Surface-Enhanced Raman Spectroscopy, *Analytical and Bioanalytical Chemistry*, 394:1803–1809, 2009.

137. S. Shanmukh, L. Jones, Y.-P. Zhao, J. D. Driskell, R. A. Tripp, and R. A. Dluhy, Identification and Classification of Respiratory Syncytial Virus (RSV) strains by Surface-Enhanced Raman Spectroscopy and Multivariate Statistical Techniques, *Analytical and Bioanalytical Chemistry*, 390:1551–1555, 2008.

138. M. Knauer, N. P. Ivleva, X. Liu, R. Niessner, and C. Haisch, Surface-Enhanced Raman Scattering-Based Label-Free Microarray Readout for the Detection of Microorganisms, *Analytical Chemistry*, 82:2766–2772, 2010.

139. X. Huang, I. H. El-Sayed, W. Qian, and M. A. El-Sayed, Cancer Cells Assemble and Align Gold Nanorods Conjugated to Antibodies to Produce Highly Enhanced, Sharp, and Polarized Surface Raman Spectra: A Potential Cancer Diagnostic Marker, *Nano Letters*, 7:1591–1597, 2007.

140. G. Wang, R. J. Lipert, M. Jain, S. Kaur, S. Chakraboty, M. P. Torres, S. K. Batra, R. E. Brand, and M. D. Porter, Detection of the Potential Pancreatic Cancer Marker MUC4 in Serum Using Surface-Enhanced Raman Scattering, *Analytical Chemistry*, 83:2554–2561, 2011.

141. C. Yuen, W. Zheng, and Z. Huang, Low-Level Detection of Anti-Cancer Drug in Blood Plasma Using Microwave-Treated Gold-Polystyrene Beads as Surface-Enhanced Raman Scattering Substrates, *Biosensors and Bioelectronics*, 26:580–584, 2010.

142. X. Qian, X.-H. Peng, D. O. Ansari, Q. Yin-Goen, G. Z. Chen, D. M. Shin, L. Yang, A. N. Young, M. D. Wang, and S. Nie, In Vivo Tumor Targeting and Spectroscopic Detection with Surface-Enhanced Raman Nanoparticle Tags, *Nature Biotechnology*, 26:83–90, 2008.

143. C. L. Zavaleta, B. R. Smith, I. Walton, W. Doering, G. Davis, B. Shojaei, M. J. Natan, and S. S. Gambhir, Multiplexed Imaging of Surface Enhanced Raman Scattering Nanotags in Living Mice Using Noninvasive Raman Spectroscopy, *Proceedings of the National Academy of Sciences*, 106:13511–13516, 2009.

144. I. Nabiev, H. Morjani, and M. Manfait, Selective Analysis of Antitumor Drug Interaction with Living Cancer Cells as Probed by Surface-Enhanced Raman Spectroscopy, *European biophysics journal*, 19:311–316, 1991.

145. C. E. Talley, L. Jusinski, C. W. Hollars, S. M. Lane, and T. Huser, Intracellular pH Sensors Based on Surface-Enhanced Raman Scattering, *Analytical Chemistry*, 76:7064–7068, 2004.

146. J. Kneipp, H. Kneipp, M. McLaughlin, D. Brown, and K. Kneipp, In Vivo Molecular Probing of Cellular Compartments with Gold Nanoparticles and Nanoaggregates, *Nano Letters*, 6:2225–2231, 2006.

147. L. Xu, H. Kuang, C. Xu, W. Ma, L. Wang, and N. A. Kotov, Regiospecific Plasmonic Assemblies for in Situ Raman Spectroscopy in Live Cells, *Journal of the American Chemical Society*, 134:1699–1709, 2012.

148. X. Wang, X. Qian, J. J. Beitler, Z. G. Chen, F. R. Khuri, M. M. Lewis, H. J. C. Shin, S. Nie, and D. M. Shin, Detection of Circulating Tumor Cells in Human Peripheral Blood Using Surface-Enhanced Raman Scattering Nanoparticles, *Cancer Research*, 71:1526–1532, 2011.

149. B. Kang, L. A. Austin, and M. A. El-Sayed, Real-Time Molecular Imaging throughout the Entire Cell Cycle by Targeted Plasmonic-Enhanced Rayleigh/Raman Spectroscopy, *Nano Letters*, 12:5369–5375, 2012.

150. B. Kang, L. A. Austin, and M. A. El-Sayed, Observing Real-Time Molecular Event Dynamics of Apoptosis in Living Cancer Cells using Nuclear-Targeted Plasmonically Enhanced Raman Nanoprobes, *ACS Nano*, 8:4883–4892, 2014.

151. S. R. Panikkanvalappil, S. M. Hira, and M. A. El-Sayed, Elucidation of Ultraviolet Radiation-Induced Cell Responses and Intracellular Biomolecular Dynamics in Mammalian Cells using Surface-Enhanced Raman Spectroscopy, 7:1133–1141, 2016.

152. Y. Wang, B. Yan, and L. Chen, SERS Tags: Novel Optical Nanoprobes for Bioanalysis, *Chemical Reviews*, 113:1391–1428, 2013.

153. J. Turkevich, P. C. Stevenson, and J. Hillier, A Study of the Nucleation and Growth Processes in the Synthesis of Colloidal Gold, *Discussions of the Faraday Society*, 11:55–75, 1951.

154. G. Frens, Controlled Nucleation for the Regulation of the Particle Size in Monodisperse Gold Suspensions, *Nature*, 241:20–22, 1973.

155. M. M. Mariani, P. Lampen, J. Popp, B. R. Wood, and V. Deckert, Impact of Fixation on In Vitro Cell Culture Lines Monitored with Raman Spectroscopy, *The Analyst*, 134:1154–1161, 2009.

156. W. Haiss, N. T. K. Thanh, J. Aveyard, and D. G. Fernig, Determination of Size and Concentration of Gold Nanoparticles from UV−Vis Spectra, *Analytical Chemistry*, 79:4215–4221, 2007.

157. A. V. Peskin and C. C. Winterbourn, A Microtiter Plate Assay for Superoxide Dismutase Using a Water-Soluble Tetrazolium Salt (WST-1), *Clinica Chimica Acta*, 293:157–166, 2000.

158. M. V. Berridge and A. S. Tan, Trans-Plasma Membrane Electron Transport: A cellular Assay for NADH- and NADPH-Oxidase Based on Extracellular, Superoxide-Mediated Reduction of the Sulfonated Tetrazolium Salt WST-1, *Protoplasma*, 205:74–82, 1998.

159. R. Masoud, T. Bizouarn, S. Trepout, F. Wien, L. Baciou, S. Marco, and C. Houée Levin, Titanium Dioxide Nanoparticles Increase Superoxide Anion Production by Acting on NADPH Oxidase, *PLoS ONE*, 10:0144829, 2015.

160. J. Heim, E. Felder, M. N. Tahir, A. Kaltbeitzel, U. R. Heinrich, C. Brochhausen, V. Mailänder, W. Tremel, and J. Brieger, Genotoxic effects of zinc oxide nanoparticles, *Nanoscale*, 7:8931–8938, 2015.

161. M. Lelimousin and M. S. P. Sansom, Membrane Perturbation by Carbon Nanotube Insertion: Pathways to Internalization, *Small*, 9:3639–3646, 2013.

162. E. Sarukhanyan, A. De Nicola, D. Roccatano, T. Kawakatsu, and G. Milano, Spontaneous Insertion of Carbon Nanotube Bundles Inside Biomembranes: A Hybrid Particle-Field Coarse-Grained Molecular Dynamics Study, *Chemical Physics Letters*, 595:–596:156–166, 2014.

163. B. D. Holt, H. Shams, T. A. Horst, S. Basu, A. D. Rape, Y.-L. Wang, G. K. Rohde, M. R. K. Mofrad, M. F. Islam, and K. N. Dahl, Altered Cell Mechanics from the Inside: Dispersed Single Wall Carbon Nanotubes Integrate with and Restructure Actin, *Journal of Functional Biomaterials*, 3:398–417, 2012.

164. H. Shams, B. D. Holt, S. H. Mahboobi, Z. Jahed, M. F. Islam, K. N. Dahl, and M. R. K. Mofrad, Actin Reorganization through Dynamic Interactions with Single-Wall Carbon Nanotubes, *ACS Nano*, 8:188–197, 2014.

165. B. D. Holt, K. N. Dahl, and M. F. Islam, Differential Sub-Cellular Processing of Single-Wall Carbon Nanotubes via Interfacial Modifications, *Journal of Materials Chemistry B*, 3:6274–6284, 2015.

166. A. Kermanizadeh, I. Gosens, L. MacCalman, H. Johnston, P. H. Danielsen, N. R. Jacobsen, A.-G. Lenz, T. Fernandes, R. P. F. Schins, F. R. Cassee, H. Wallin, W. Kreyling, T. Stoeger, S. Loft, P. Møller, L. Tran, and V. Stone, A Multilaboratory Toxicological Assessment of a Panel of 10 Engineered Nanomaterials to Human Health—ENPRA Project—The Highlights, Limitations, and Current and Future Challenges, *Journal of Toxicology and Environmental Health, Part B*, 19:1–28, 2016.

167. B. B. Manshian, S. Munck, P. Agostinis, U. Himmelreich, and S. J. Soenen, High Content Analysis at Single Cell Level Identifies Different Cellular Responses Dependent on Nanomaterial Concentrations, *Scientific Reports*, 5:13890, 2015.

168. S. R. Panikkanvalappil, M. James, S. M. Hira, J. Mobley, T. Jilling, N. Ambalavanan, and M. A. El-Sayed, Hyperoxia Induces Intracellular Acidification in Neonatal Mouse Lung Fibroblasts: Real-Time Investigation Using Plasmonically Enhanced Raman Spectroscopy, *Journal of the American Chemical Society*, 138:3779–3788, 2016.

169. S. R. Panikkanvalappil, S. M. Hira, M. A. Mahmoud, and M. A. El-Sayed, Unraveling the Biomolecular Snapshots of Mitosis in Healthy and Cancer Cells Using Plasmonically-Enhanced Raman Spectroscopy, *Journal of the American Chemical Society*, 136:15961–15968, 2014.

170. N. Feliu, X. Sun, R. A. Alvarez Puebla, and W. J. Parak, Quantitative Particle–Cell Interaction: Some Basic Physicochemical Pitfalls, *Langmuir*, 27:6639–6646, 2017.

171. J. Rejman, M. Nazarenus, D. Jimenez de Aberasturi, A. H. Said, N. Feliu, and W. J. Parak, Some Thoughts about the Intracellular Location of Nanoparticles and the Resulting Consequences, *Journal of Colloid and Interface Science*, 482:260–266, 2016.

172. R. Tantra, R. J. C. Brown, and M. J. T. Milton, Strategy to Improve the Reproducibility of Colloidal SERS, *Journal of Raman Spectroscopy*, 38:1469–1479, 2007.

173. A. C. S. Talari, Z. Movasaghi, S. Rehman, and I. ur Rehman, Raman Spectroscopy of Biological Tissues, *Applied Spectroscopy Reviews*, 50:46–111, 2015.

174. J. Bella, M. Eaton, B. Brodsky, and H. M. Berman, Crystal and Molecular Structure of a Collagen-Like Peptide at 1.9 A Resolution, *Science (New York, N.Y.)*, 266:75–81, 1994.

175. R. Z. Kramer, J. Bella, P. Mayville, B. Brodsky, and H. M. Berman, Sequence Dependent Conformational Variations of Collagen Triple-Helical Structure, *Nature Structural Biology*, 6:454–457, 1999.

176. T. E. Petersen, H. C. Thøgersen, K. Skorstengaard, K. Vibe-Pedersen, P. Sahl, L. Sottrup-Jensen, and S. Magnusson, Partial Primary Structure of Bovine Plasma Fibronectin: Three Types of Internal Homology, *Proceedings of the National Academy of Sciences*, 80:137–141, 1983.

177. G. Neurauter, K. Schrocksnadel, S. Scholl-Burgi, B. Sperner-Unterweger, C. Schubert, M. Ledochowski, and D. Fuchs, Chronic Immune Stimulation Correlates with Reduced Phenylalanine Turnover, *Current Drug Metabolism*, 9:622–627, 2008.

178. J. Turco and H. H. Winkler, Gamma-Interferon-Induced Inhibition of the Growth of Rickettsia prowazekii in Fibroblasts cannot be Explained by the Degradation of Tryptophan or Other Amino Acids., *Infection and Immunity*, 53:38–46, 1986.

179. M. C. Duran, H.-L. Chan, and J. F. Timms, Identification of Oxidative Stress-Induced Tyrosine Phosphorylated Proteins by Immunoprecipitation and Mass Spectrometry, *Methods in Molecular Biology (Clifton, N.J.)*, 527:33–45, 2009.

180. N. Khatibzadeh, A. A. Spector, W. E. Brownell, and B. Anvari, Effects of Plasma Membrane Cholesterol Level and Cytoskeleton F-Actin on Cell Protrusion Mechanics, *PloS One*, 8:57147, 2013.

181. D. B. Mitchell, K. S. Santone, and D. Acosta, Evaluation of Cytotoxicity in Cultured Cells by Enzyme Leakage, *Journal of tissue culture methods*, 6:113–116, 1980.

182. P. Ghezzi, V. Bonetto, and M. Fratelli, Thiol–Disulfide Balance: From the Concept of Oxidative Stress to that of Redox Regulation, *Antioxidants & Redox Signaling*, 7:964–972, 2005.

183. S. Toyokuni, K. Okamoto, J. Yodoi, and H. Hiai, Persistent Oxidative Stress in Cancer, *FEBS Letters*, 358:1–3, 1995.

184. J. L. Martindale and N. J. Holbrook, Cellular Response to Oxidative Stress: Signaling for Suicide and Survival, *Journal of Cellular Physiology*, 192:1–15, 2002.

185. A. Krammer, D. Craig, W. E. Thomas, K. Schulten, and V. Vogel, A Structural Model for Force Regulated Integrin Binding to Fibronectin's RGD-Synergy Site, *Matrix Biology: Journal of the International Society for Matrix Biology*, 21:139–147, 2002.

186. H. Bachman, J. Nicosia, M. Dysart, and T. H. Barker, Utilizing Fibronectin Integrin-Binding Specificity to Control Cellular Responses, *Advances in Wound Care*, 4:501–511, 2015.

187. D. Cavallo, C. Fanizza, C. L. Ursini, S. Casciardi, E. Paba, A. Ciervo, A. M. Fresegna, R. Maiello, A. M. Marcelloni, G. Buresti, F. Tombolini, S. Bellucci, and S. Iavicoli, Multi-Walled Carbon Nanotubes Induce Cytotoxicity and Genotoxicity in Human Lung Epithelial Cells, *Journal of Applied Toxicology*, 32:454–464, 2012.

188. C. Kirchner, T. Liedl, S. Kudera, T. Pellegrino, A. Muñoz Javier, H. E. Gaub, S. Stölzle, N. Fertig, and W. J. Parak, Cytotoxicity of Colloidal CdSe and CdSe/ZnS Nanoparticles, *Nano Letters*, 5:331–338, 2005.

189. Y. Yamauchi, C. C. Y. Chang, M. Hayashi, S. Abe-Dohmae, P. C. Reid, T.-Y. Chang, and S. Yokoyama, Intracellular Cholesterol Mobilization Involved in the ABCA1/Apolipoprotein-Mediated Assembly of High Density Lipoprotein in Fibroblasts, *Journal of Lipid Research*, 45:1943–1951, 2004.

190. G. Kuku, M. Saricam, F. Akhatova, A. Danilushkina, R. Fakhrullin, and M. Culha, Surface-Enhanced Raman Scattering to Evaluate Nanomaterial Cytotoxicity on Living Cells, *Analytical Chemistry*, 88:9813–9820, 2016.

191. G. Kuku and M. Culha, Investigating the Origins of Toxic Response in TiO2 Nanoparticle-Treated Cells, *Nanomaterials*, 7:83, 2017.

192. M. Altunbek, G. Kuku, and M. Culha, Gold Nanoparticles in Single-Cell Analysis for Surface Enhanced Raman Scattering, *Molecules*, 21:1617, 2016.

193. S. McAughtrie, K. Faulds, and D. Graham, Surface Enhanced Raman Spectroscopy (SERS): Potential Applications for Disease Detection and Treatment, *Journal of Photochemistry and Photobiology C: Photochemistry Reviews*, 21:40–53, 2014.

194. L. Cui, S. Chen, and K. Zhang, Effect of Toxicity of Ag Nanoparticles on SERS Spectral Variance of Bacteria, *Spectrochimica Acta Part A: Molecular and Biomolecular Spectroscopy*, 137:1061–1066, 2015.

195. B. Zhang, L. Cui, and K. Zhang, Dosage- and Time-Dependent Antibacterial Effect of Zinc Oxide Nanoparticles Determined by a Highly Uniform SERS Negating Undesired Spectral Variation, *Analytical and Bioanalytical Chemistry*, 408:3853–3865, 2016.

196. E. Efeoglu, A. Casey, and H. J. Byrne, In Vitro Monitoring of Time and Dose Dependent Cytotoxicity of Aminated Nanoparticles Using Raman Spectroscopy, *The Analyst*, 141:5417–5431, 2016.

197. P. Knief, C. Clarke, E. Herzog, M. Davoren, F. M. Lyng, A. D. Meade, and H. J. Byrne, Raman Spectroscopy-A Potential Platform for the Rapid Measurement of Carbon Nanotube-Induced Cytotoxicity, *The Analyst*, 134:1182–1191, 2009.

198. M. Davoren, E. Herzog, A. Casey, B. Cottineau, G. Chambers, H. J. Byrne, and F. M. Lyng, In Vitro Toxicity Evaluation of Single Walled Carbon Nanotubes on Human A549 Lung Cells, *Toxicology in Vitro*, 21:438–448, 2007.

199. J. H. Nazemi and J. F. Brennan, Lipid Concentrations in Human Coronary Artery Determined with High Wavenumber Raman Shifted Light, *Journal of Biomedical Optics*, 14:034009, 2009.

200. S. Koljenović, T. C. Bakker Schut, R. Wolthuis, B. de Jong, L. Santos, P. J. Caspers, J. M. Kros, and G. J. Puppels, Tissue Characterization Using High Wave Number Raman Spectroscopy, *Journal of Biomedical Optics*, 10:031116, 2005.

201. X. Zhou, J. Dai, Y. Chen, G. Duan, Y. Liu, H. Zhang, H. Wu, and G. Peng, Evaluation of the Diagnostic Potential of Ex Vivo Raman Spectroscopy in Gastric Cancers: Fingerprint versus High Wavenumber, *Journal of Biomedical Optics*, 21:105002–105002, 2016.

202. S. Debaisieux, V. Encheva, P. Chakravarty, A. P. Snijders, and G. Schiavo, Analysis of Signaling Endosome Composition and Dynamics Using SILAC in Embryonic Stem Cell-Derived Neurons, *Molecular & cellular proteomics: MCP*, 15:542–557, 2016.